Faculty of Physics and Astronomy

University of Heidelberg

Diploma thesis

in Physics

submitted by

Börge Hemmerling

born in Saarlouis

2006

Thermally Induced Fluctuations in a Bosonic Josephson Junction

This diploma thesis has been carried out by Börge Hemmerling at the
Kirchhoff Institute of Physics
under the supervision of
Prof. Dr. M. K. Oberthaler

Thermisch induzierte Fluktuationen in einem bosonischen Josephson Kontakt

Ein bosonischer Josephson Kontakt kann mit Hilfe eines Bose-Einstein Kondensates in einem Doppelmuldenpotential erzeugt werden. Dies ermöglicht es, das Kondensat in zwei lokalisierte Wellenfunktionen aufzuspalten. Der endliche Überlapp der Wellenfunktionen im Bereich der Doppelmuldenbarriere führt zu einer Kopplung der beiden Moden durch tunnelnde Atome. Im Rahmen dieser Arbeit werden thermische Effekte in einem solchen Kontakt untersucht, die zu Fluktuationen der relativen Phase zwischen den Moden führen. Diese thermischen Phasenfluktuationen werden als Funktion der Temperatur und der Tunnelkopplung gemessen.

Die Phasenfluktuationen werden zur Bestimmung der Temperatur eines Bose Gases weit unterhalb der kritischen Temperatur herangezogen. In diesem Regime versagen Standardmethoden, da diese von der Meßbarkeit des thermischen Anteils des Bose Gases abhängen. Des weiteren wird das Aufheizen eines Bose Gases in einer dreidimensionalen harmonischen Falle gemessen. Die daraus resultierende Wärmekapazität ist konsistent mit der theoretisch erwarteten eines idealen Bose Gases.

Thermally Induced Fluctuations in a Bosonic Josephson Junction

A Bosonic Josephson Junction is realised by loading a Bose-Einstein condensate into a double-well potential which allows to split the condensate into two localized wave functions. The finite overlap of the wave functions in the region of the double-well barrier leads to a coupling of the two condensates due to tunnelling. In this thesis, we investigate finite temperature effects in such a junction that result in fluctuations of the relative phase between the wells. These thermal phase fluctuations are measured as a function of temperature and tunnelling coupling.

We use these phase fluctuations to determine the temperature of a Bose gas far below the critical temperature. In this regime standard methods are not applicable since they rely on the observation of the thermal component of the Bose gas. We further measure the heating up of the Bose gas in a three-dimensional harmonic trap. The deduced heat capacity is consistent with the prediction for an ideal Bose gas.

Contents

List of Figures

Fundamental Constants

Quantity	Symbol	Value	Unit
Speed of light	c	$2.99792458 \cdot 10^{8}$	m s^{-1}
Boltzmann Constant	k_B	$1.3806503(24) \cdot 10^{-23}$	J K^{-1}
Planck Constant	h	$6.62606876(52) \cdot 10^{-34}$	J s
	$h/2\pi$	$1.054571596(82) \cdot 10^{-34}$	J s
	k_B/h	$20.836644(36)$	Hz nK^{-1}
Bohr Magneton	μ_B	$9.27400899(37) \cdot 10^{-23}$	J T^{-1}
Riemann Zeta Function	$\zeta(3/2)$	$2.61238\ldots$	
	$\zeta(2)$	$\pi^2/6 = 1.64493\ldots$	
	$\zeta(5/2)$	$1.34149\ldots$	
	$\zeta(3)$	$1.20206\ldots$	
	$\zeta(4)$	$\pi^4/90 = 1.08232\ldots$	

Specific Data on Rubidium-87			
Mass	m	$1.4445 \cdot 10^{-25}$	kg
s-Wave Scattering Length	a	5.32	nm
Saturation Intensity	I_{sat}	1.58	mW cm^{-2}
D2-Line Width	Γ	$2\pi \times 6.065$	MHz

Chapter 1

Introduction

The invention of quantum mechanics in the last century revised the understanding of the microscopic world completely. Among the most fascinating - with classical theory not explainable - results are the wave nature of massive particles [1] and the resulting matter wave interference of these particles. The first experiments on interfering electrons have been realised by Davisson and Germer in 1927 [2]. These effects can be explained by describing the quantum particles with a wave function whose absolute square corresponds to the probability density. However, the propablility description implies that it is necessary to do many measurements in order to fully charaterize the wave function of a particle. This situation is different with a Bose-Einstein condensate (BEC). The phenomenon of Bose-Einstein condensation, a result of the theoretical investigations done by Bose in 1924 on photons and Einstein 1925 on massive bosons [3, 4], predicts that a macroscopic number of bosons can occupy the same quantum state. In such a system the wave function can be fully characterized by doing just one measurement. In this sense a BEC, representing a macroscopic matter wave, is an extraordinary probe for doing quantum mechanical investigations.

One way to generate a Bose-Einstein condensate is cooling a dilute bosonic vapor below the critical temperature, where the condensation takes place. Since this critical transition is usually found in the micro-Kelvin regime, the experimental realisation is an enormous technical challenge. It took seventy years after the theoretical prediction to generate the first Bose-Einstein condensate in a dilute vapor. The experiments have been done by Wiemann, Cornell, Hulet and Ketterle in 1995 [5, 6, 7]. Since then, this new type of matter has provided a useful tool for studying matter wave dynamics, as for instance the interference of two Bose-Einstein condensates which has been accomplished for the first time by Ketterle in 1997 [8].

Josephson Junctions

Another fundamental but also in the classical sense contradictory effect is the tunnelling of massive particles through regions that are forbidden from a classical point of view. This effect can also be accessed with a Bose-Einstein condensate by loading the condensate into a double-well potential. This setup is referred to as Bose-Einstein or Bosonic Josephson Junction (BJJ). The condensate in such a junction splits in two modes and populates both wells. These two modes are weakly coupled by particles that tunnel through the barrier of the double-well potential. The reason for calling it Bosonic Josephson Junc-

tion is, that it is very similar to the well-known Josephson junction in solid state and condensed matter physics. There, people did extensive studies about weak links between two modes of superfluid helium (see [9] for a review article on that) and weak links of two superconductors. For the latter the barrier consists of a thin insulator. However, the similarity arises from the fact that all three systems are describable within a similar model. The modes are associated with two macroscopic wave functions with an overall phase for each. These wave functions are assumed to overlap in the region of the barrier what results in a weak coupling. The coupling itself is then physically given by particles that tunnel through the barrier.

The origin of these junctions relies on a theoretical prediction of Brian D. Josephson in the year 1962 [10] who claimed one should observe a current across the insulating barrier in the case of the superconductors. This current depends on the relative phase of the two macroscopic wave functions that describe the Cooper pairs in each superconductor. The origin of this current - as mentioned above - was supposed to be Cooper pairs that tunnel through the barrier. This tunnelling effect has been proven one year later in 1963 [11]. Nowadays, the superconducting Josephson junction has many useful applications, such as SQUIDS (superconducting quantum interference devices) [12], consisting of two Josephson junctions, with which it is possible to measure magnetic field variations to a very high accuracy. Furthermore, the Josephson junction have lead to high accuracy measurements on the ratio of the electron charge to the Planck constant and it has provided the basis of the nowadays used voltage standard.

However, the implementation of a Bose-Einstein Josephson Junction has recently been accomplished for the first time in our group by loading a condensate into an optical double-well potential. The tunnelling dynamics - given by the temporal evolution of the relative phase and the population imbalance between the two modes - has been subject to experiments in our group [13]. A profound theoretical description of such a BJJ can be found for instance in [14, 15, 16].

Finite Temperature Effects in a Bosonic Josephson Junction

A Josephson Junction with a Bose-Einstein condensate can be utilized to investigate finite temperature effects resulting from the thermal component of the condensate. The interaction of the thermal particles with the particles in the condensate fraction leads to a scrambling of the relative phase of the two macroscopic wave functions, whereas the coherent coupling of the wave functions by particles tunnelling through the barrier stabilizes it. This results in shot-to-shot[1] fluctuations of the relative phase. The process is investigated by studying interference measurements with the two modes in the BJJ. The resulting interference pattern, that corresponds to the momentum distribution of the condensate, can be used to directly deduce the relative phase of the two modes. In the scope of this thesis these phase fluctuations are quantitativley studied by measuring the coherence factor, which represents the visibility of the average of many single interference patterns, as a function of tunnelling coupling and the temperature.

Since the coherence factor depends on the temperature it can be used for doing thermometry. What makes it so interesting is the fact that this method is applicable in a

[1]Shot-to-shot means that one measurement can be done with one condensate since the condensate is destroyed during the measurement. After that a new condensate needs to be created under the same experimental conditions.

regime where standard methods fail. The commonly used methods rely on measuring the expansion of the thermal cloud, since it is directly connected to the temperature. However, this is only suitable where the thermal cloud is observable and can be distinguished from the background noise. Since for temperatures far below the critical temperature only a few atoms occupy higher states, this method is not applicable anymore. But, in this regime the thermal phase fluctuations are still present and thus can be utilized to deduce the temperature.

In the scope of this thesis this new thermometer is demonstrated by measuring the heating up of a Bose gas in a three dimensional harmonic trap. In order to validate the new method, the result is cross-checked with a standard method in a regime where both are applicable. Furthermore, for higher temperatures a change in the heating up is supposed to be seen as soon as the critical temperature is crossed. This different behaviour results from a discontinuity in the heat capacity of the Bose gas due to a phase transition at the critical temperature.

Contents of this Thesis

The following thesis is divided into four chapters: In chapter two and chapter three, the theoretical description of the considered phenomena and the system is given. First, the basic theoretical description of the appearance of Bose-Einstein condensation of a dilute Bose gas in a harmonic trap and the heat capacity of this configuration is discussed. After introducing the non-linear Schrödinger equation, i.e. the so-called Gross-Pitaevskii equation that predicts the condensate dynamics, in chapter three a two-mode approximation of a Bose-Einstein condensate in a double-well potential (BJJ) is described. The main part of chapter three focusses on quantum mechanical and thermal fluctuations concerning two dynamical variables - the relative phase and the population imbalance - that are defined within the scope of the two-mode model. Furthermore, the momentum distribution of the condensate in the Bosonic Josephson Junction is discussed with respect to thermal fluctuations of the relative phase.

Chapter four gives an overview of the experimental setup used to realize the BJJ. Here, the main steps of cooling a dilute Rubidium-87 vapor down to quantum degeneracy and preparing the resulting condensate in an optical double-well potential is explained. The last part of this chapter deals with the calibration of the relevant and accessable experimental parameters.

In chapter five the experimental results on the thermal fluctuations of the relative phase between the two-modes of the condensate are presented. Furthermore, a technique is discussed how to apply these results as a new tool for thermometry. This point is studied in the context of heating up a Bose gas in a harmonic trap.

After summarizing the results and giving an outlook for future prospects, the last part of this thesis contains appendices considering mathematical and numerical calculations for the two-mode model and the used non-linear Schrödinger equation. Furthermore, a numerical comparison of the used classical Hamiltonian for the two-mode model and the exact Hamiltonian in second quantization is given.

Chapter 2

Theory of Bose-Einstein Condensation

The fact that identical particles are indistinguishable in quantum mechanics leads to new phenomena. For instance the statistical behaviour of a many particle system is different than predicted by classical theory. It depends on the quantum nature of particles as there are fermions and bosons. Considering bosons one prominent phenonemon is the Bose-Einstein condensation where a macroscopic number of particles occupies a single quantum mechanical state. This is not possible with fermions since they have to obey the Pauli principle. The Bose-Einstein condensation has been predicted by Bose [3] in 1924 for photons and by Einstein [4] in 1925 for massive bosons. In the following chapter we theoretically discuss the occurance of condensation for dilute Bose gases at very low temperatures. Since this effect comes along with a quantum phase transition we also study the heat capacity of a bose gas in this regime.

Furthermore, in order to consider dynamics of a Bose-Einstein condensate the Gross-Pitaevskii equation, a non-linear Schrödinger equation, is discussed. It describes the temporal evolution of the wave function with which a Bose-Einstein condensate is associated.

2.1 Bose-Einstein Condensation in a Harmonic Trap

We consider a non-interacting Bose gas within the grand canonical ensemble. The atoms shall be in a trapping potential with discrete single particle states. The mean number of atoms $\langle n_i \rangle$ found in the ith state with energy ε_i is given by the Bose-Einstein distribution

$$\langle n_i \rangle = \frac{1}{e^{(\varepsilon_i - \mu)/k_B T} - 1} \tag{2.1}$$

where μ is the chemical potential and T the temperature of the gas (see standard textbooks [17]). The chemical potential, being the energy needed to transfer a particle from infinity to the system, is always smaller than the lowest eigenenergy ε_0. Otherwise, the number of atoms in a particular state is less than zero which is not physical.

We assume the average number of atoms N in the gas to be constant[1]

$$N = \sum_i \langle n_i \rangle \tag{2.2}$$

[1]The sum is to be taken over all possible single particle states.

This constraint defines the chemical potential μ implicitly. For evaluating this sum we replace it by an integral. This is valid if the spacing between the energy levels is small compared to the temperature. By introducing the density of states $g(\varepsilon)$ at a given energy we replace the sum by

$$\sum \rightarrow \int d\varepsilon g(\varepsilon) \tag{2.3}$$

While doing this we have to consider the following problem: If the density of states is zero at the lowest state, this state is not taken into account. This problem arises for instance when we consider a harmonic trapping potential. In order to correct this error we separate the first term of the sum before integrating. We write Eq. (2.2) as

$$N = N_0 + \underbrace{\int\limits_{\varepsilon>\varepsilon_0} d\varepsilon g(\varepsilon) \frac{1}{e^{(\varepsilon-\mu)/k_B T} - 1}}_{N_{\text{ex}}} \tag{2.4}$$

where N_0 is the number of particles in the ground state and N_{ex} the number of particles in the excited states.

As the density of states depends on the external potential, we consider a gas of bosons with mass m in a three dimensional harmonic oscillator potential

$$V(\mathbf{r}) = \frac{1}{2} m(\omega_x^2 x^2 + \omega_y^2 y^2 + \omega_z^2 z^2) \tag{2.5}$$

This is a good approximation to real trapping potentials since nearly all experiments use potentials of parabolic shape or ones that can be approximated by a parabola to some extend. The density of states[2] is then given by [18]

$$g(\varepsilon) = \frac{1}{2} \left(\frac{1}{\hbar \bar{\omega}} \right)^3 \varepsilon^2 \qquad \text{with } \bar{\omega} = \sqrt[3]{\omega_x \omega_y \omega_z} \tag{2.6}$$

If we insert this expression into Eq. (2.4) we find that the integral on the right hand side is finite for all temperatures, corresponding to the fact that the number of particles in the excited states is finite at any given temperature. If we decrease the temperature (while keeping the number of atoms constant, accompanied by an increase of the chemical potential until $\mu \approx \varepsilon_0$) we will reach a temperature where the number of particles which are allowed to occupy the excited states is less than the total atom number. Decreasing the temperature further will leave only one possibility to the atoms, namely occupying the ground state. This results in a macroscopic occupation of the ground state and is called *Bose-Einstein condensation*. The point where this transition takes place is characterised by the *critical temperature* T_c. Another possibility to reach condensation is to increase the total number of particles to more than the critical value in the excited states at a given temperature.

We calculate the transition point in the thermodynamical limit[3] where we set $\mu = \varepsilon_0 = 0$

$$N = N_{\text{ex}}\,(T = T_c, \mu = 0) \quad \Longrightarrow \quad k_B T_c = \hbar \bar{\omega} \left(\frac{N}{\zeta(3)} \right)^{1/3} \tag{2.7}$$

[2]The number of states $G(\varepsilon)$ can be calculated by summing over all possible quantum numbers in order to get all possible states at a given energy. The density is then defined as $g(\varepsilon) := \partial_\varepsilon G(\varepsilon)$.

[3]This means $N \rightarrow \infty, \hbar\omega \rightarrow 0$ with $N \cdot \hbar\omega = \text{const.}$. Taking a finite number of particles and finite size effects into account leads to a non-discrete transition temperature.

With this result we can find a power law for the number of atoms which occupy the ground state. If we solve Eq. (2.4) and insert the critical temperature we find

$$\frac{N_0}{N} = 1 - \left(\frac{T}{T_c}\right)^3 \tag{2.8}$$

For a real system with interacting particles these calculations are a good approximation as long as $na^3 \ll 1$, where n is the atom number density and a is the s-wave scattering length.

2.2 Heat Capacity of a Bose-Einstein Condensate

The heat capacity of a gas of classical particles is expected to be constant and non-zero for all temperatures. This is in contradiction to the third law of thermodynamics which states that the heat capacity should vanish while the temperature is approaching absolute zero. Thus, the inclusion of quantum nature of particles is necessary for a correct description of the heat capacity. Especially, below the critical temperature, quantum effects become significant and we expect a behaviour different to that predicted by classical description. In the following, we discuss the heat capacity of a Bose gas both for temperatures above and below the transition temperature (see also [18, 19]).

The heat capacity per particle is defined as the amount of energy gained or lost while changing the temperature

$$c := \frac{1}{N}\left(\frac{dE}{dT}\right) \tag{2.9}$$

We calculate the energy E of a bosonic atomic ensemble. This is done by taking the sum over all energy levels weighted with their occupation number

$$E = \sum_i \varepsilon_i \langle n_i \rangle \approx \varepsilon_0 N_0 + \int\limits_{\varepsilon > \varepsilon_0} d\varepsilon \frac{\varepsilon g(\varepsilon)}{e^{(\varepsilon-\mu)/k_B T} - 1} \tag{2.10}$$

We again consider the case of atoms confined in a harmonic potential. If we evaluate the integral above in the thermodynamic limit ($\epsilon_0 = 0$) we find

$$E = \left(\frac{g_4(z)}{\zeta(3)}\right) 3k_B N T \left(\frac{T}{T_c}\right)^3 \tag{2.11}$$

where we have introduced the fugacity $z = \exp(\mu/k_B T)$ and the generalized Riemann Zeta function

$$g_\nu(z) = \sum_{l=1}^{\infty} \frac{z^l}{l^\nu} \tag{2.12}$$

For temperatures lower than the critical temperature we can set the fugacity $z = 1$ and the specific heat can be directly calculated. For temperatures higher than T_c we have to determine $z(T)$ and thus $\mu(T)$[4]. The heat capacity for the whole temperature range

[4] In order to do this we insert the density of states (Eq. (2.6)) into the Eq. (2.4) and set $N_0 = 0$. This integral is then to be solved numerically since $\mu(T)$ is only given implicitly.

then reads

$$c(T) = \begin{cases} \left(4\dfrac{\zeta(4)}{\zeta(3)}\right) 3k_B \left(\dfrac{T}{T_c}\right)^3 & (T < T_c) \\ \\ \left(4\dfrac{g_4(z)}{g_3(z)} - 3\dfrac{g_3(z)}{g_2(z)}\right) 3k_B & (T \geq T_c) \end{cases} \tag{2.13}$$

We consider the results in the limit of very high temperatures. In this case $z(T) \ll 1$ and can be expanded to second order. The heat capacity then reads

$$c(T \gg T_c) = \left(1 + \frac{\zeta(3)}{2^3}\left(\frac{T_c}{T}\right)^3\right) 3k_B \quad \longrightarrow \quad 3k_B \quad (T \to \infty) \tag{2.14}$$

The fact that the heat capacity goes asymptotically to $3k_B$ is consistent with the value expected from classical theory.

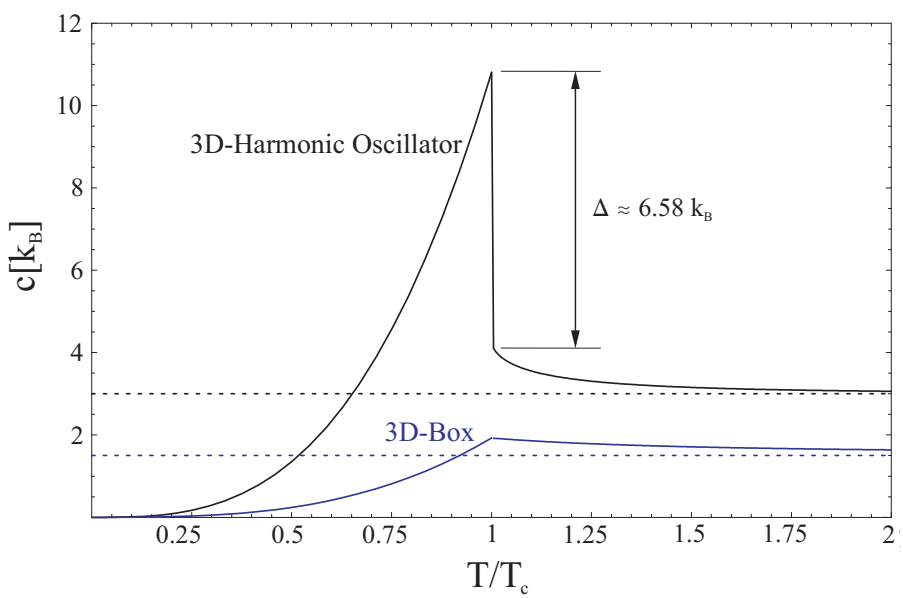

Figure 2.1: The heat capacity per particle of a Bose gas in units of the Boltzman constant vs temperature is shown. The black curve corresponds to the heat capacity of a Bose gas in a 3D harmonic oscillator. The blue curve shows the same for a Bose gas confined in a 3D box. In both cases we see a deviation from the values predicted by classical theory which are indicated by the dashed horizontal lines.

The results from above are summarized in Fig. 2.1. If we cool down a Bose gas starting from a high temperature, the gas undergoes a second-order phase transition since the heat capacity is discontinuous at the critical temperature. The jump at the discontinuity is $\Delta \approx 6.58k_B$. Cooling further yields that $c \propto T^3$. Thus, $c \to 0$ as predicted by the third law of thermodynamics. Also depicted is the behaviour of the heat capacity for a bosonic vapor in a three dimensional box. It can be calculated in the same way by using the corresponding density of states $g(\varepsilon) \propto \sqrt{\varepsilon}$. In this case we have a first-order phase transition at the critical temperature. The slope below the critical temperature is proportional to $T^{3/2}$.

2.3 Temporal Evolution of a BEC within a Mean-Field Approach

To accurately describe the dynamics of a realistic system composed of many bosons, one has to take atom-atom interaction into account. To overcome the problem of exactly solving the resulting many body Schrödinger equation we work with a *mean-field* description at zero temperature. This means that for one particle the interaction with the other particles is described by an average potential. It reduces the many body problem to a one-body problem. The condensate is then described by a one-body wave function[5] $\Psi(\mathbf{r}, t)$ where the absolute square of the wave function is equal to the atomic density

$$n(\mathbf{r}, t) = |\Psi(\mathbf{r}, t)|^2 \tag{2.15}$$

The resulting equation that describes the temporal evolution of the condensate wave function is called the *Gross-Pitaevskii equation* (GPE). It was first developed by Gross [20, 21] and Pitaevskii [22]. For most experimental realizations the GPE is a very good approximation and is suitable to describe the dynamics of most nowadays experiments.

2.3.1 The Gross-Pitaevskii Equation

One way to derive the Gross-Pitaevskii equation, is using the quantum least action principle with the corresponding action functional[6] (see [18, 23] for more details). The GPE is then the Euler-Lagrange equation of the action functional. It reads

$$\imath\hbar\frac{\partial}{\partial t}\Psi(\mathbf{r}, t) = \left[-\frac{\hbar^2}{2m}\Delta + V_{\text{ext}}(\mathbf{r}, t) + g\,|\Psi(\mathbf{r}, t)|^2\right]\Psi(\mathbf{r}, t) \tag{2.16}$$

The wave function $\Psi(\mathbf{r}, t)$ is normalized to the number of atoms

$$\int d\mathbf{r}|\Psi(\mathbf{r}, t)|^2 = N \tag{2.17}$$

The GPE is similar to the Schrödinger equation with an additional non-linear term $g\,|\Psi(\mathbf{r}, t)|^2$ which accounts for the atom-atom interaction. The constant g is only depending on the mass m and the s-wave scattering length a since for dilute gases at low temperatures elastic s-wave scattering between the atoms is dominant. The interaction constant is given by $g = \frac{4\pi\hbar^2 a}{m}$.

If we want to consider the stationary case we factorize time and space in the wave function as $\Psi(\mathbf{r}, t) = \Psi(\mathbf{r})\exp(-\imath\mu t/\hbar)$. Putting this into Eq. (2.16) yields the stationary GPE

$$\mu\Psi(\mathbf{r}) = \left[-\frac{\hbar^2}{2m}\Delta + V_{\text{ext}}(\mathbf{r}) + g\,|\Psi(\mathbf{r})|^2\right]\Psi(\mathbf{r}) \tag{2.18}$$

In general one cannot solve the GPE analytically. There are two limits to the GPE where this is possible in some cases as for the harmonic oscillator. In the first regime

[5] In the mean-field approach this one-body wave function $\Psi(\mathbf{r}, t)$ equals the expectation value of the bosonic field operator $\Psi(\mathbf{r}, t) = \langle\hat{\Psi}(\mathbf{r}, t)\rangle$.

[6] The action functional here reads $S = \int dt d\mathbf{r}\Psi^*(\mathbf{r}, t)\left[\imath\hbar\partial_t + \hbar^2/2m\nabla^2 - V_{\text{ext}}(\mathbf{r}) - gN/2|\Psi(\mathbf{r}, t)|^2\right]\Psi(\mathbf{r}, t)$.

we neglect the interaction between the atoms and the GPE simplifies to the well-known linear Schrödinger equation. In the opposite case we are in the Thomas-Fermi limit, i.e. the kinetic energy term is neglected. Here we directly write down a solution as[7]

$$|\Psi(\mathbf{r})|^2 = \frac{1}{g}(\mu - V_{\text{ext}}(\mathbf{r}))\Theta(\mu - V_{\text{ext}}(\mathbf{r})) \tag{2.19}$$

If we are in the intermediate regime it is necessary to take the kinetic and interaction energy into account. As mentioned above it is difficult to find solutions of the GPE even for simple potentials due to its non-linearity. Thus, it is necessary to do a numerical approach to the GPE. Since for some experimental situations it is suitable to consider a quasi one-dimensional gas we discuss this approach with a dimensional reduced GPE.

2.3.2 Gross-Pitaevskii Equation in one dimension

We assume the condensate to be in an external potential which is harmonic in the transverse direction and of arbitrary shape in x direction

$$V_{\text{ext}}(\mathbf{r}, t) = V_{\text{ext}}(x, t) + \frac{1}{2}m\omega_\perp^2(y^2 + z^2) \tag{2.20}$$

We make an ansatz for the wave function with a gaussian shape in the transverse direction which reads

$$\Psi(\mathbf{r}, t) = \frac{1}{\sqrt{\pi\sigma_\perp^2}}\Psi(x, t)\exp\left(-\frac{y^2 + z^2}{2\sigma_\perp^2}\right) \tag{2.21}$$

The width of the transverse gaussian $\sigma_\perp$ is either assumed to be constant or it can vary in time and x-direction. The first case applies to a quasi-one dimensional situation where the transverse dynamics can be neglected. The second case takes transverse dynamics to some extend into account. We discuss the results of both cases in the following.

One-dimensional Gross-Pitaevskii Equation

We insert the ansatz Eq. (2.21) into the 3D-GPE and integrate over the y and z-direction. Here, the transverse width $\sigma_\perp$ is set to be constant and equal to the ground state width of a harmonic oscillator

$$\sigma_\perp = \sqrt{\frac{\hbar}{m\omega_\perp}} \tag{2.22}$$

The result is a one-dimensional Gross-Pitaevskii equation which reads

$$\imath\hbar\frac{\partial}{\partial t}\Psi(x, t) = \left(-\frac{\hbar^2}{2m}\frac{\partial^2}{\partial x^2} + V_{\text{ext}} + g_{1d}|\Psi(x, t)|^2\right)\Psi(x, t) \tag{2.23}$$

with an effective one-dimensional interaction constant $g_{1d} = 2a\hbar\omega_\perp$.

Since the interaction couples the dynamics in all three spatial dimensions the one-dimensional GPE is only valid if the interaction energy is small compared to the energy of the transverse ground state, i.e. $g_{1d}|\Psi(x, t)|^2 \ll \hbar\omega_\perp/2$. This can be re-written in terms of the s-wave scattering length as $a|\Psi(x, t)|^2 \ll 1$.

[7] $\Theta(x) = 1$ for $x > 0$ and $\Theta(x) = 0$ for $x < 0$

Non-Polynomial Schrödinger Equation

In many situations a more accurate approach to tackle quasi one-dimensional problems is to include a variable transverse width. Using the ansatz Eq. (2.21) for the quantum least action principle one finds (see [24])

$$\imath\hbar\frac{\partial}{\partial t}\Psi(x,t) = \left[-\frac{\hbar^2}{2m}\frac{\partial^2}{\partial x^2} + V_{\text{ext}}(x) + g_{1d}\frac{|\Psi(x,t)|^2}{\sqrt{1+2a|\Psi(x,t)|^2}} + \frac{\hbar\omega_\perp}{2}\left(\frac{1}{\sqrt{1+2a|\Psi(x,t)|^2}} + \sqrt{1+2a|\Psi(x,t)|^2}\right)\right]\Psi(x,t) \tag{2.24}$$

$$\text{with } \sigma_\perp(x,t)^2 = \left(\frac{\hbar}{m\omega_\perp}\right)\sqrt{1+2a|\Psi(x,t)|^2} \tag{2.25}$$

This equation is called a *Non-Polynomial Schrödinger equation* (NPSE). It turns out that it is in good agreement with the exact solution of the 3D-GPE (see [24] for a numerical comparison).

The NPSE can be handled numerically more easily than the GPE since only a one-dimensional equation is to be solved. A numerical solution of the NPSE with a Fourier split-step algorithm is discussed in Appendix C.

Chapter 3

Theory of a Bosonic Josephson Junction

Quantum mechanics predicts that massive particles tunnel through energetically forbidden regions. In solid state physics many investigations of the tunneling phenomena have been done with Superconducting Josephson Junctions (SJJ). A SJJ consists of two superconductors serparated by a thin insulating barrier. In such a junction the electron cooper pairs in the superconductors can tunnel through the barrier. This results in a supercurrent accross the barrier which has been predicted by Josephson in 1962 [10]. We study a similar situation but instead of cooper pairs in superconductors, we consider bose condensed Rubidium-87 atoms confined in a double-well potential. As described in the following sections the Bose-Einstein condensate splits up in two modes, that are localized in each well, which are coupled by tunnelling through the barrier in between. This is called a Bosonic Josephson Junction (BJJ). It is in close analogy to a BJJ of superfluid ^{3}He-A [9].

The condensate modes are described by two macroscopic wave functions that are overlapping in the region of the barrier. A similar description is valid for the cooper pairs in a SJJ. Thus, we expect both situations to be described by a similar model which results in similar dynamics.

In this chapter a theoretical description of the dynamics occuring in such a Bosonic Josephson Junction is given. The used model results in two relevant dynamical variables, the relative atom number and the relative phase between the two modes of the condensate. Since these are conjugate variables we furthermore discuss the quantum mechanical uncertainty of their corresponding operators. In the last part of this chapter finite temperature effects in a Bosonic Josephson Junction that manifest themselves by fluctuations in the dynamical variables are considered.

3.1 The Two-Mode Model

We discuss the dynamics of a Bose-Einstein condensate with N atoms in a double-well potential. This can be realized by the superposition of a three dimensional harmonic potential and a one-dimensional periodic potential. Thus, we assume the external potential

to be of the form

$$V_{\text{ext}}(x) = \frac{1}{2}m(w_x^2x^2 + w_y^2y^2 + w_z^2z^2) + \frac{V_0}{2}\left(\cos\left(\frac{2\pi}{q_0}x\right) + 1\right) \tag{3.1}$$

First, we study some properties of this potential. It is depicted for the x-direction in Fig. 3.1(a) for a harmonic confinement of $w_x = 2\pi \times 90\text{Hz}$, a spacing of $q_0 = 4.78\mu\text{m}$. The solid black line shows the pure harmonic trap ($V_0 = 0$) whereas the green solid line shows a double-well potential ($V_0 > 0$). We define the effective barrier of the double-well as the difference between the local maximum in the center and the minimum of the potential. The effective barrier is useful when comparing the barrier with energy scales that are in respect to the minimum of the trap. The difference between the effective barrier and the barrier height[1] V_0 is depicted in Fig. 3.1(b) as a function of V_0. For larger values of V_0 the difference is approximately given by an offset.

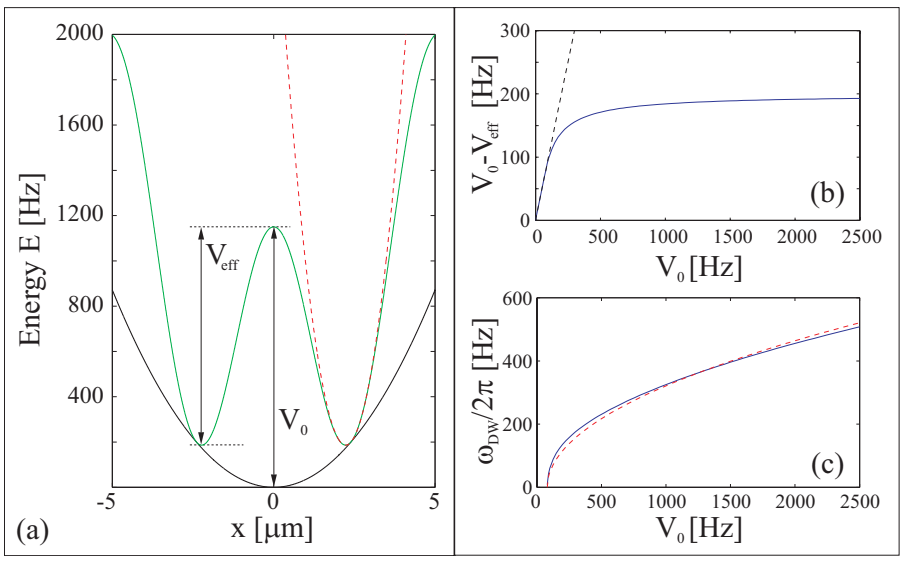

Figure 3.1: An example of the potential Eq. (3.1) is shown for a harmonic confinement of $w_x = 2\pi \times 90\text{Hz}$ and a spacing of $q_0 = 4.78\mu\text{m}$. (a) shows the potential in x-direction. The solid black line depicts the case of a pure harmonic potential, i.e. $V_0 = 0$. The solid green line depicts the case of $V_0 > 0$ leading to a double-well potential. Also seen in the picture is the definition of the effective barrier as the difference between the local maximum in the center and the minimum of the potential. The red dashed line shows a harmonic approximation of the potential in one of the wells. (b) The difference between the effective barrier and the barrier height is shown. The dashed line depicts the bisecting line. For larger values of V_0 the deviation to the effective barrier height increases and levels to an offset. (c) shows the frequencies resulting from the harmonic approximation in one of the wells. The behaviour can in very good agreement be fitted with a square root function (Eq. (3.2)).

In order to estimate a timescale inside one of the wells we approximate the potential harmonically and compare the result with a harmonic oscillator with the frequency ω_{DW}. This is depicted in Fig. 3.1(a) by the red dashed line. In Fig. 3.1(c) the frequencies for the well are plotted as a function of the barrier height. It can be approximated by a square root function. The corresponding fit (dashed red line in the figure) yields as a thumb rule for the harmonic frequency of the well

$$\omega_{\text{DW}} = 2\pi \times 10.58\text{Hz} \cdot \sqrt{V_0[\text{Hz}] - 80} \tag{3.2}$$

[1]This has to be calculated numerically since the zero points of the first derivative of the double-well potential are only implicitly given.

The function is shifted since for barrier heights smaller than $V_0 = 80\text{Hz}$ the potential is not consisting of two clearly distinguishable wells. For these values the harmonic potential is only flattened around the minimum. It should be noted that these numbers are only valid for the considered example of $\omega_x = 2\pi \times 90\text{Hz}$ and $q_0 = 4.78\mu\text{m}$. For other parameters the values of the double-well frequency and the effective barrier height is different. We will refer to these parameters later again.

After this preliminary thoughts we study the eigenenergie spectrum of the double-well potential. In Fig. 3.2 a comparison between the harmonic potential and the double-well potential is shown. Increasing the barrier in the middle decreases the energy gap between the first excited and the ground state. The other states are less shifted.

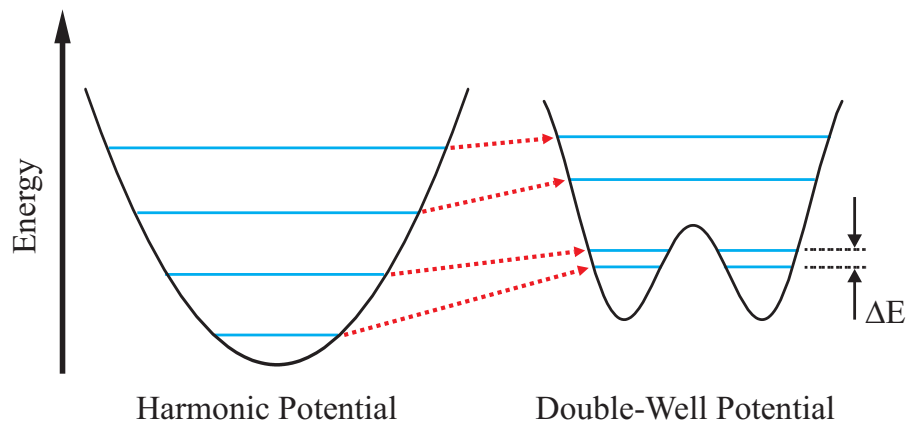

Figure 3.2: Schematic comparison between the eigenenergie spectrum (blue lines) of a harmonic potential and a double-well potential. The harmonic potential has equidistant levels. Introducing a barrier by adding a cosine potential leads to a smaller splitting of the ground and the first excited state. The higher energy states are less influenced. See Appendix C for a numerical comparison.

Since this energy gap is small compared to the distance to the higher states we only consider the first two states being populated[2] wherease higher states are neglected. For the following discussion we denote the groundstate eigenfunction as φ_+ and the eigenfunction of the first excited state as φ_-. They satisfy the stationary GPE

$$\beta_\pm \varphi_\pm(\mathbf{r}) = \left(-\frac{\hbar^2}{2m}\Delta + V_{\text{ext}}(\mathbf{r}) + g\left|\varphi_\pm(\mathbf{r})\right|^2 \right) \varphi_\pm(\mathbf{r}) \tag{3.3}$$

where $\beta_\pm$ is the corresponding chemical potential. The two eigenfunctions are orthornomal $\langle \varphi_i | \varphi_j \rangle = \delta_{ij}$ with $i, j \in \{+, -\}$ and due to the symmetry of the potential we have $\varphi_\pm(x) = \pm\varphi_\pm(-x)$.

As shown in Fig. 3.3 we combine these eigenfunctions to construct two modes φ_1 and φ_2 which account for the left and right well separately

$$\varphi_{1,2}(\mathbf{r}) = \frac{1}{\sqrt{2}}(\varphi_+(\mathbf{r}) \pm \varphi_-(\mathbf{r})) \tag{3.4}$$

With the considerations above we assume the wave function describing the condensate to be a superposition of the wave functions φ_1 and φ_2 with the complex amplitudes ψ_1 and ψ_2

$$\Psi(\mathbf{r}, t) \quad = \quad \psi_1(t)\varphi_1(\mathbf{r}) + \psi_2(t)\varphi_2(\mathbf{r}) \tag{3.5}$$

[2]For real experimental parameters it turns out that the first two states are nearly degenerated (see Appendix C).

This ansatz is commonly referred to as the *Two-Mode Approximation*. $\psi_{1,2}(t)$ are the time-dependent amplitudes of the corresponding mode $\varphi_{1,2}(x)$ with

$$\psi_{1,2}(t) = \sqrt{N_{1,2}(t)}e^{\imath\theta_{1,2}(t)} \tag{3.6}$$

where $N_{1,2}(t)$ is the number of atoms in the left and right well, repectively. The functions $\theta_{1,2}(t)$ correspond to the phase of each mode of the condensate. It should be emphasized that in this model the phase is assumed to be constant over the well but it can vary in time. This description is suitable as long as the coupling of the two modes, which is resulting from the overlap of both, is small (see [25] for a detailed investigation on this).

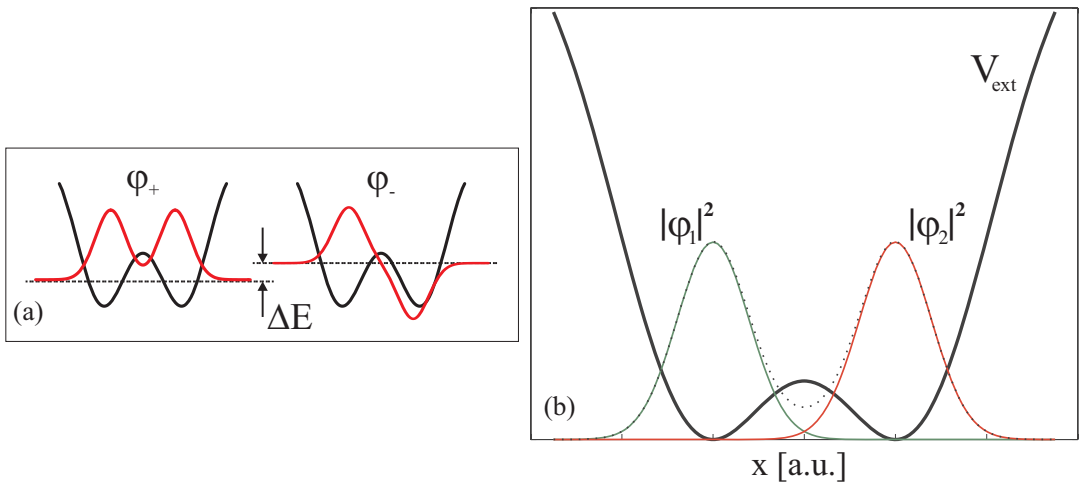

Figure 3.3: Two-Mode Approximation of the wave function in a double-well potential. (a) The black curve corresponds to the external double-well potential. The symmetric ground state φ_+ and the antisymmetric first excited state φ_- is plotted (red curve) with the energy gap ΔE. (b) The two superpositions $|\varphi_{1,2}|^2$ of the ground and the first excited state are plotted with $\varphi_{1,2} = (\varphi_+ \pm \varphi_-)/\sqrt{2}$. The dotted curve shows the resulting superposition $|\varphi_1 + \varphi_2|^2$.

In order to consider the relative dynamics between the two wells it is convenient to define new dynamical variables

$$\begin{aligned} n(t) &= \frac{1}{2}(N_1(t) - N_2(t)) \\ \phi(t) &= \theta_2(t) - \theta_1(t) \end{aligned} \tag{3.7}$$

The new quantity $n(t)$ is the number of atoms which are transferred from one mode to the other starting with the symmetric case. $\phi(t)$ corresponds to the relative phase between the two modes.

In order to obtain the temporal evolution of the dynamical variables we first derive the describing equations for $\psi_{1,2}(t)$. We put the two-mode ansatz Eq. (3.5) into the time-dependent Gross-Pitaevskii equation, multiply by $\varphi_{1,2}(x)$ respectively and integrate over space. We end up with two coupled differential equations for $\psi_{1,2}(t)$ describing their temporal evolution. The coupling of the equations will be given in terms of a tunneling parameter. In the following we discuss two approaches to these equation. The first

approach (we will refer to this as the *Standard Two-Mode Model* [16]) neglects all mixed terms that are of higher order than two in $\varphi_{1,2}$. In contrast to this the second approach takes all terms into account (*Improved Two-Mode Model* [25, 26]). We study these two models in the following sections.

3.1.1 The Standard Two-Mode Model

With the ansatz (Eq. (3.5)) as described above we find two coupled differential equations for $\psi_{1,2}$ (see Appendix A for the main steps of the derivation)

$$\begin{aligned} \imath\hbar\frac{\partial\psi_1}{\partial t} &= (E_1 + U_1 N_1)\psi_1 - K\psi_2 \\ \imath\hbar\frac{\partial\psi_2}{\partial t} &= (E_2 + U_2 N_2)\psi_2 - K\psi_1 \end{aligned} \tag{3.8}$$

with the following definitions

$$\begin{aligned} E_{1,2} &= \int d\mathbf{r}\left(\tfrac{1}{2}\left|\nabla\varphi_{1,2}\right|^2 + |\varphi_{1,2}|^2 V_{\text{ext}}\right) \\ U_{1,2} &= g\int d\mathbf{r}|\varphi_{1,2}|^4 \\ K &= -\int d\mathbf{r}\left(\tfrac{\hbar}{2m}\left(\nabla\varphi_1\nabla\varphi_2\right) + \varphi_1 V_{\text{ext}}\varphi_2\right) \end{aligned} \tag{3.9}$$

Here, $E_{1,2}$ is the energy of each mode and $U_{1,2}$ is the on-site interaction energy. The coupling term K accounts for the amplitude of tunnelling between the two wells since it contains the overlap of the two modes $\varphi_{1,2}$. In this model K is assumed to be constant and does not depend on the interaction.

With the use of the relative quantities (Eq. (3.7)) we rewrite Eq. (3.8) and find for the time evolution of the phase difference and the population imbalance

$$\begin{aligned} \frac{d\phi}{dt} &= 2U\cdot n - \left(\frac{4K}{N}\right)\cdot\frac{n}{\sqrt{1-4n^2/N^2}}\cos\phi \\ \frac{dn}{dt} &= -KN\sqrt{1-4n^2/N^2}\sin\phi \end{aligned} \tag{3.10}$$

These are the coupled dynamical equations for n and ϕ. They describe the temporal evolution of the population imbalance and the relative phase between the two modes of the BEC in the double-well potential.

We can write the dynamical Eq. (3.10) in canonical form like in Hamiltonian classical mechanics (see standard textbooks [27])

$$\frac{d\phi}{dt} = \frac{\partial H}{\partial n} \quad ; \quad \frac{dn}{dt} = -\frac{\partial H}{\partial\phi} \tag{3.11}$$

The Hamiltonian then reads

$$H(n,\phi) = U\cdot n^2 - NK\cdot\sqrt{1-\frac{4n^2}{N^2}}\cos\phi \tag{3.12}$$

This Hamiltonian can be seen in a mechanical analogy. It corresponds to a non-rigid pendulum with deviation angle ϕ and angular momentum n. The length of the pendulum l is given by $l = \sqrt{1-4n^2/N^2}$ (see also [16]).

3.1.2 The Improved Two-Mode Model

In the scope of the Improved Two-Mode Model the terms of higher order in $\varphi_{1,2}$ are not neglected. Again, the main steps of the derivation are given in the Appendix A (for a detailed derivation see [25]). The equations describing the temporal evolution of $\psi_{1,2}$ are of the same form as in the Standard Two-Mode Model (Eq. (3.8))

$$\begin{aligned} \imath\frac{\partial\psi_1}{\partial t} &= M_1\psi_1 - K_1\psi_2 \\ \imath\frac{\partial\psi_2}{\partial t} &= M_2\psi_2 - K_2\psi_1 \end{aligned} \tag{3.13}$$

For clarity the quantities $M_{1,2}$ and $K_{1,2}$ are defined in the Appendix A. Here, the dynamical equations for n and ϕ read

$$\begin{aligned} \frac{d\phi}{dt} &= \left(\frac{2A}{N}\right)\cdot n + \left(\frac{2B}{N}\right)\cdot\frac{n}{\sqrt{1-4n^2/N^2}}\cos\phi - \left(\frac{2C}{N}\right)\cdot n\cos(2\phi) \\ \frac{dn}{dt} &= -\left(\frac{NB}{2}\right)\sqrt{1-\frac{4n^2}{N^2}}\sin\phi + \left(\frac{NC}{2}\right)\cdot\left(1-\frac{4n^2}{N^2}\right)\sin(2\phi) \end{aligned} \tag{3.14}$$

Again, for the definition of the quantities A, B and C see Appendix A. In this case the Hamiltonian

$$H = \left(\frac{2A}{N}\right)\cdot\frac{n^2}{2} - \left(\frac{NB}{2}\right)\cdot\sqrt{1-\frac{4n^2}{N^2}}\cos\phi + \frac{1}{2}\left(\frac{NC}{2}\right)\cdot\left(1-\frac{4n^2}{N^2}\right)\cos(2\phi) \tag{3.15}$$

leads to the canonical form for n and ϕ.

We discuss this Hamiltonian in more detail. In order to understand the new quantities A, B and C we compare these to the ones defined in the Standard Two-Mode model. With the mathematical relation which can be found in Appendix A we see that B is comparable with the tunnelling parameter K whereas A and C account for the atomic interaction. The quantity C can be expressed in terms of $\varphi_{1,2}$ as

$$C = g\int d\mathbf{r}\varphi_1^2\varphi_2^2 \tag{3.16}$$

We see that the overlap of the two wave functions $\Psi_{1,2}$ is crucial for the value of C since it contains $\varphi_{1,2}$ *both* in second order. For our experimental parameters it turns out that C is always small compared to B (the quantities A, B and C are plotted in the Appendix A). Thus, we neglect this term in the following considerations.

We define the *charging energy* $E_c := 2A/N$ and the *Josephson tunnelling energy* $E_J := NB/2$. With these new quantities and the considerations above the Hamiltonian reads

$$\boxed{H(n,\phi) = \frac{1}{2}E_c n^2 - E_J\sqrt{1-\frac{4n^2}{N^2}}\cos\phi} \tag{3.17}$$

In Appendix B this Hamtilonian is plotted as a function of ϕ and n.

For investigating the dynamical regimes of this Hamiltonian we first consider the limit of small n and ϕ. As mentioned above we can write the dynamical equations (Eq. (3.14)) in canonical form with the two conjugate variables n and ϕ. For this reason it is appropriate to search for analogies with other Hamiltonian systems. We expand the Hamiltonian to second order in both variables

$$H(n,\phi) = \frac{1}{2}\left(E_c + \frac{4E_J}{N^2}\right)n^2 + \frac{1}{2}E_J\phi^2 - E_J + O(\phi^3) + O(n^3) + O(n^2\phi^2) \quad (3.18)$$

Associating the variables ϕ and n with a spatial variable x and the corresponding momentum p Eq. (3.18) is similar to the Hamiltonian of a particle moving in a harmonic potential potential ($H = p^2/2m + m\omega^2x^2/2$). Thus, we expect sinusoidal oscillations for small n and ϕ. Comparing the two cases yields

$$\omega_p = \frac{1}{\hbar}\sqrt{E_J\left(E_c + \frac{4E_J}{N^2}\right)} = \frac{1}{\hbar}\sqrt{E_cE_J} \qquad (E_c \gg E_J/N^2) \quad (3.19)$$

for the oscillation frequency. In the limit of $E_c \gg E_J/N^2$ it is referred to as the *plasma frequency* ω_p.

In the case of large n or ϕ there are different dynamical regimes of the Josephson Hamiltonian (Eq. (3.17)). They have been subject to detailed theoretical and experimental studies. In the next section a brief overview of the results is given.

3.1.3 Dynamics of a Bosonic Josephson Junction

We give a brief overview of the expected dynamical behaviour of a Bosonic Josephson Junction in the following. For a detailed theoretical and experimental description I refer to the publications [16, 25] and the theses of Albiez and Fölling [28, 29, 13].

We distinguish two regimes which result from the equation of motion Eq. (3.14)[3]: the *Josephson Oscillation* regime and the *Macroscopic Quantum Self-Trapping* regime. They can be accessed by adjusting the initial conditions, i.e. the initial population imbalance $n_0 = n(t=0)$ and the initial relative phase $\phi_0 = \phi(t=0)$.

Josephson Oscillations

In Fig. 3.4 the phase plane portrait of the equation of motion for the mentioned regimes is shown. In the plot the population imbalance is given in terms of $z = 2/N \cdot n$. Choosing small relative phases and small population imbalances we end up in the Josephson oscillation regime (closed trajectories in the phase plane portrait). The points correspond to measurements (see [28, 29]). The atoms oscillate between the wells coming along with a phase oscillation. The advantage of a bosonic Josephson junction is that one can directly observe at the relative phase in contrast to the superconducting junction (see section 3.3 on the deduction of the relative phase between the modes).

[3]The experimental results turned out to be better explained within the scope of the Improved Two-Mode Model than the Standard Two-Mode Model. Especially the tunneling times for the Josephson junction had been in better agreement with the experiment (see [28, 29]).

Macroscopic Quantum Self-Trapping

The second regime as can be seen from Fig. 3.4 is accessed by increasing n_0 above a critical value. This regime is charaterized by a nearly stationary behaviour of n accompanied by an unbound phase ϕ. Thus, the population imbalance is just doing small oscillations around a non-zero value and the atoms are 'trapped' in one well. For this reason this regime is called *self-trapping*.

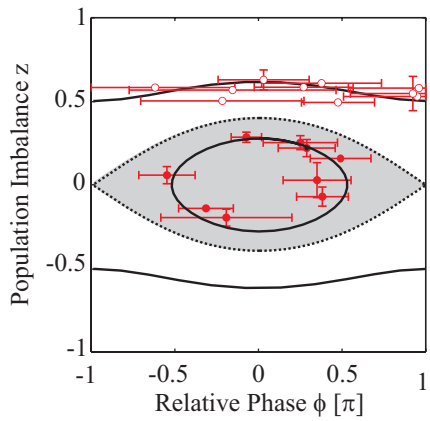

Figure 3.4: Phase Plane Portrait of the Bosonic Josephson Junction. The solid black lines correspond to the theoretical prediction of the Improved Two-Mode Model and are calculated without a free parameter. The closed black line shows the expected sinusoidal oscillations of the relative phase ϕ and the population imbalance $z = 2/N \cdot n$ around zero (Josephson Oscillation regime). The other curve corresponds to a nearly stationary state of the population imbalance coming along with an unbound evolution and monotonically increase of the relative phase. (Macroscopic Self-Trapping regime). The transition between the two regimes is exhibited by the separatrix (dashed line). The points correspond to measurements which have been recently done in our group (see [28, 29]).

3.2 Fluctuations within the Two-Mode Model

So far, we have discussed the Bosonic Josephson Junction within the two-mode model. In this context the dynamical variables n and ϕ do not include any kind of fluctuations. We distinguish between two kinds: *quantum fluctuations* and *thermally induced fluctuations*. For investigating quantum fluctuations [30] we replace the dynamical variables by the corresponding quantum mechanical operators. Quantum fluctuations then correspond to the Heisenberg uncertainty that comes along with the operators. In contrast to that thermal fluctuations arise from the finite temperature that is given by the inevitable thermal fraction of the atom cloud. It turns out that by choosing the right charging energy E_c and tunneling energy E_J we can isolate the thermal fluctuations from the quantum ones.

In the following section these two kind of fluctuations are discussed with respect to our dynamical variables n and ϕ.

3.2.1 Quantum Fluctuations

We quantize the Hamiltonian

$$H(n,\phi) = \frac{1}{2}E_c n^2 - E_J\sqrt{1-4\frac{n^2}{N^2}}\cos\phi \tag{3.20}$$

by introducing the non-commutating operators[4] $\hat{n}$ and $\hat{\phi}$ with

$$[\hat{\phi}, \hat{n}] = i \tag{3.21}$$

The origin of this can be demonstrated with a simple analogy. Let us assume we have two sources of N atoms each. We do interference measurements with these two sources by coupling out atoms, letting them interfere and detect them on a screen. In the beginning the system is in the state with N atoms in each source. We call this state $|N, N\rangle$. Let us further assume that we can imprint a quantum mechanical phase on one of the sources. Depending on this phase we will gain different interference pattern. However, if we look at a short time scale we will see single atoms hitting the screen separately. We can't tell from which source the single atom originates without loosing the interference pattern (in analogy to the double-slit experiment). So, keeping the interference and having started in a state $|N, N\rangle$ we end up in a superposition $|N, N-1\rangle + |N-1, N\rangle$ as the state for the source. But having detected one atom tells us nothing about the relative phase of the two sources. We need to do many measurements in order to achieve the interference pattern from which we can deduce the phase. But then considering the two sources we can't tell anything about the distribution of the atoms anymore.

Associating the variable ϕ with this relative phase and n with the population difference in the reservoirs we can see that the more we know about the phase the less we know about the atom numbers. In that sense the two variables do not commute.

Having quantized the Hamiltonian we estimate the quantum fluctuations by considering the case of small oscillations and refer to the harmonic approximation of the Hamiltonian (Eq. (3.18)). We take the ground state for the resulting harmonic oscillator

$$\psi_0 \propto \exp\left(-\frac{m\omega\phi^2}{2\hbar}\right) \quad \text{with } \omega = \frac{1}{\hbar}\sqrt{E_J\left(E_c + \frac{4E_J}{N^2}\right)} \tag{3.22}$$

and calculate the fluctuations for the ground state for both operators as

$$(\Delta\phi)^2 = \langle\phi^2\rangle - \langle\phi\rangle^2 = \langle\psi_0|\phi^2|\psi_0\rangle - \langle\psi_0|\phi|\psi_0\rangle^2 \tag{3.23}$$

We find that the quantum fluctuations of the number and phase operator are given by

$$(\Delta\phi)^2 = \frac{1}{2}\cdot\sqrt{\frac{E_c + \frac{4E_J}{N^2}}{E_J}} \tag{3.24}$$

$$(\Delta n)^2 = \frac{1}{2}\cdot\sqrt{\frac{E_J}{E_c + \frac{4E_J}{N^2}}} \tag{3.25}$$

Thus, these fluctuations follow the uncertainty relation $\Delta\phi \cdot \Delta n = 1/2$.

We distinguish between three regimes as there is the *Fock*, the *Josephson* and the *Rabi* regime. The Rabi regime is found in the limit of $E_c \ll E_J/N^2$. Here, the phase is well defined and the atom number fluctuations are equal to the number of atoms $\Delta n = \sqrt{N}$. The Fock regime is characterized by $E_c \gg E_J$. The atom number is well

[4] Of course, this is a quite ad hoc quantization but it is also possible to get these operators by defining the Hamiltonian in the context of creation and annihilation operators. One finds that the operator $\hat{n}$ is then given by ∂_ϕ in the phase representation (see [30] and references therein).

defined whereas the phase is completely undefined. The Josephson regime yields a well-defined phase and atom number. It is characterized by $E_J/N^2 \ll Ec \ll E_J$. The corresponding fluctuations then read

$$(\Delta\phi)^2 = \frac{1}{2} \cdot \sqrt{\frac{E_c}{E_J}} \ll 1 \quad ; \quad \frac{(\Delta n)^2}{N} = \frac{1}{2} \cdot \sqrt{\frac{E_J/N^2}{E_c}} \ll 1 \tag{3.26}$$

Thus, we can neglect quantum fluctuations for the relative phase and the relative population number in the Josephson regime.

3.2.2 Thermal Fluctuations

In order to investigate thermal effects we assume the system to be in the Josephson regime, so that quantum fluctuations are negligible. We also consider our system to be in the classical limit where the plasma frequency (Eq. (3.19)) is small compared to the mean energy $\hbar\omega_p \ll k_B T$. In this case we can regard the states as continuously distributed.

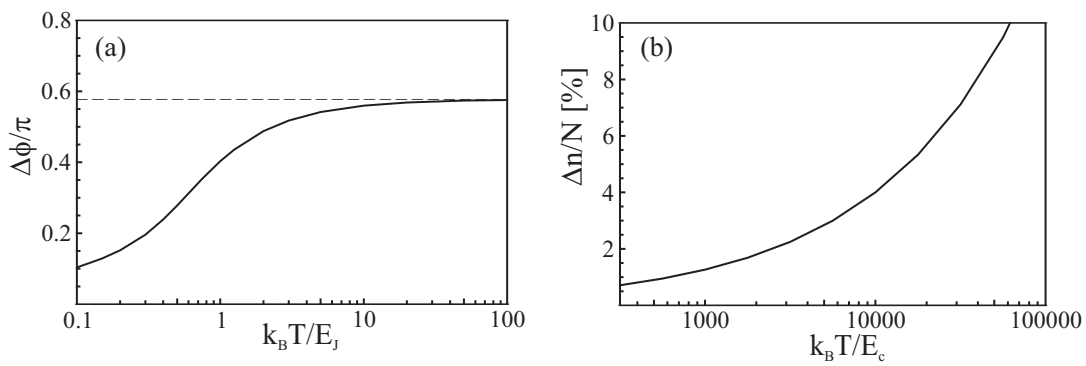

Figure 3.5: Thermal Fluctuations in a Bosonic Josephson Junction with 2500 atoms. (a) shows the thermal average of ϕ^2 in units of π depending on $k_B T/E_J$. The dashed lines shows the limit for high temperatures which reads $\pi/\sqrt{3}$. The curve was calculated for $E_c/k_B = 20$pK. Varying E_c shows that the phase fluctuations do not significantly depend on that. (b) depicts the thermal average of n^2 relative to the total number of atoms. The curve was plotted for $E_J/k_B = 100$nK. Varying E_J, only small changes for the relative number fluctuations are seen.

The states are assumed to be weighted according to the Boltzmann factor $\exp(-E/k_B T)$ where E is the energy of each state and T the temperature [31]. To gain information about the variables ϕ and n we consider their thermal averages[5] [31]

$$(\Delta\phi)^2 = \langle\phi^2\rangle_{\text{th}} - \underbrace{\langle\phi\rangle_{\text{th}}^2}_{=0} = \frac{1}{\gamma}\int_{-\pi}^{\pi} d\phi \int_{-N/2}^{N/2} dn \cdot \phi^2 \cdot \exp(-E/k_B T) \tag{3.27}$$

$$(\Delta n)^2 = \langle n^2\rangle_{\text{th}} - \underbrace{\langle n\rangle_{\text{th}}^2}_{=0} = \frac{1}{\gamma}\int_{-\pi}^{\pi} d\phi \int_{-N/2}^{N/2} dn \cdot n^2 \cdot \exp(-E/k_B T) \tag{3.28}$$

with the normalization $\gamma = \int_{-N/2}^{N/2} dn \int_{-\pi}^{\pi} d\phi \exp(-E/k_B T)$ and the energy $E = H(n, \phi)$. In Fig. 3.5(a,b) the behaviour of the thermal fluctuations depending on the ratio of

[5]Sums over states are to be replaced by integrals since we assume the states to be continously distributed.

k_BT/E_J and k_BT/E_c is depicted. The fluctuations of the relative phase increase with increasing temperature and approach asymptotically the value $\pi/\sqrt{3}$. This corresponds to a completely random phase. As shown in the figure we expect the phase fluctuations to get important as soon as the temperature is on the order of the tunnelling energy. The number fluctuations are for the same parameters ($E_J/k_B = 100$nK, $T = 50$nK) on the order of one percent. Since this is not measurable with our current experimental setup we focus on the phase fluctuations only. Their investigation is discussed in the next section.

3.3 Interference Pattern of the Two Condensate Modes in the Scope of Thermal Phase Fluctuations

The relative phase between the two modes of a Bose-Einstein in a double-well potential governs its momentum distribution. The fluctuations of the relative phase manifests themselves in different momentum distributions for each time the distribution is measured. This effect is discussed in the following. Furthermore, we consider how the relative phase is distributed as a function of the temperature and the tunnelling energy E_J.

3.3.1 Momentum Distribution in a Bosonic Josephson Junction

Let the two modes of the Bose-Einstein condensate have a relative phase ϕ. The condensates are separated in the double-well by a distance d along the x-direction. The shape of the wave function of each mode is called $\eta(x)$. If we switch off the confinement the two modes are allowed to expand freely and thus will interfere. The density distribution after a long expansion time corresponds to the momentum distribution. Interaction effects are neglected in this consideration since the density is very low after the expansion when the two condensates crucially overlap (see [32, 33] for a detailed consideration of interaction effects in interference experiments). Since the momentum distribution is depending on the relative phase between the condensates we can deduce this phase by investigating the interference patterns.

We assume the wave function to be in a superposition

$$\Psi(x) = a \cdot \eta\left(x - \frac{d}{2}\right) + b \cdot \eta\left(-\left(x + \frac{d}{2}\right)\right) \cdot e^{\iota\phi} \tag{3.29}$$

In order to find the momentum distribution we calculate the Fourier transformation of the wave function. The absolute squared value of the momentum distribution reads

$$I(p, \phi) = |F(\Psi(x))|^2 = |F(\eta(x))|^2 \cdot \left[a^2 + b^2 + 2ab \cdot \cos\left(\phi - d \cdot \frac{p}{\hbar}\right)\right] \tag{3.30}$$

In Fig. 3.6 the expected interference pattern are plotted for different values of the relative phase. The initial density distribution η of each mode is assumed to be of gaussian shape for these patterns. We see that different relative phases result in a shift of the pattern with respect to the gaussian envelope. The visibility (or contrast) of such a pattern is defined as

$$V_{\text{single}} := V(I) = \frac{I_{\max} - I_{\min}}{I_{\max} + I_{\min}} = \frac{2ab}{a^2 + b^2} \tag{3.31}$$

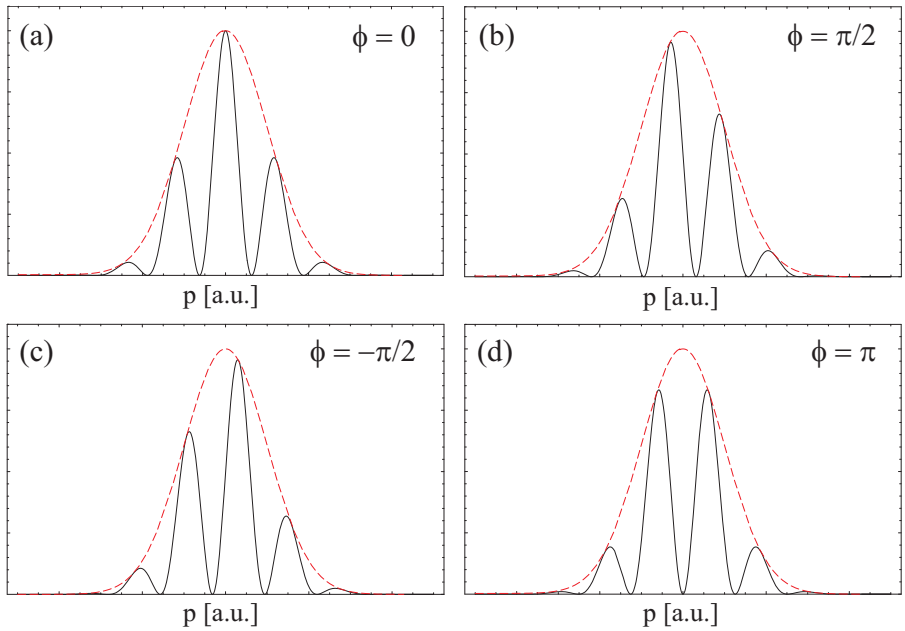

Figure 3.6: The plots (a)-(d) depict the interference pattern of the two modes of a BEC in a double-well potential for different relative phases ϕ. The density distribution of each mode has been assumed to be of gaussian shape. The red dashed curve depicts the gaussian envelope of the momentum distribution. Different relative phases lead to a shift of the momentum distribution with respect to the envelope.

For the symmetric case, i.e. a=b, the visibility equals one. Doing single interference measurements we always get the same maximal visibility independent of the relative phase. However, if we assume that the relative phase fluctuates from shot-to-shot and we average over every interference measurement, the visibility of this averaged pattern will depend on the amount of fluctuations of the relative phase. This is discussed in the next section.

3.3.2 Averaged Interference Pattern and the Coherence Factor

We assume the relative phase to be fluctuating between the values $-\phi_0$ and ϕ_0 with $\phi_0 \in [0, \pi]$. In order to characterize these shot-to-shot fluctuations we discuss averaged interference pattern. The averaged momentum distribution reads

$$\langle I(p) \rangle = \frac{1}{2\phi_0} \int_{-\phi_0}^{\phi_0} d\phi I(p, \phi) = |F(\eta(x))|^2 \cdot \left[a^2 + b^2 + 2ab \cdot \alpha \cdot \cos\left(d \cdot \frac{p}{\hbar} \right) \right] \tag{3.32}$$

with the *coherence factor*

$$\alpha = \langle \cos\phi \rangle = \frac{1}{2\phi_0} \int_{-\phi_0}^{\phi_0} d\phi \cos\phi = \frac{\sin\phi_0}{\phi_0} \tag{3.33}$$

The visibility of the averaged pattern reads

$$V(\langle I \rangle) = \left(\frac{2ab}{a^2 + b^2} \right) \cdot \alpha = V_{\text{single}} \cdot \alpha \tag{3.34}$$

Thus, the coherence factor is a direct measure of the visibility of the averaged interference pattern.

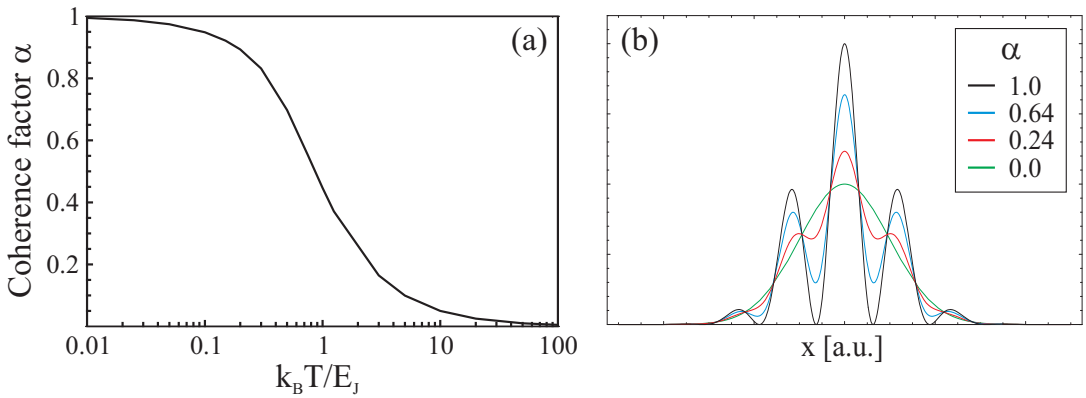

Figure 3.7: (a) The coherence factor is plotted as a function of k_BT/E_J for 20pK. (b) The averaged interference pattern is plotted for different values of the coherence factor. With full coherence $\alpha = 1$ the interference pattern is sutained since the relative phase is not fluctuating. Decreasing alpha, coming along with increasing phase fluctuations, leads to a decrease of the visiblity of the averaged pattern.

If the coherence factor $\alpha \to 0$, the averaged interference pattern is smeared out since its visibility vanishes. On the other hand, if $\alpha \to 1$, corresponding to small fluctuations of the relative phase, the averaged interference pattern is sustained and similar to the single shot pattern for a relative phase that equals the mean value of the phase distribution. Since we assume the phase to be fluctuating with zero mean value, this pattern equals the one for $\phi = 0$. This behaviour is depicted in Fig. 3.7(b). Theoretically we expect α to depend on k_BT/E_J like

$$\alpha = \langle \cos\phi \rangle_{\text{th}} = \frac{1}{\gamma} \int_{-\pi}^{\pi} d\phi \int_{-N/2}^{N/2} dn \cdot \cos\phi \cdot \exp(-E/k_BT) \tag{3.35}$$

where $E = H(n, \phi)$ and γ the normalization constant (see above). In Fig. 3.7(a) the coherence factor is plotted for $E_c = 20$pK.

For $n \ll N$ we neglect the square root in the Hamiltonian. We find an analytical result for the coherence factor

$$\alpha = \langle \cos\phi \rangle_{\text{th}} = \frac{\int_{-\pi}^{\pi} d\phi \cos\phi \exp(E_J \cos\phi / k_BT)}{\int_{-\pi}^{\pi} d\phi \exp(E_J \cos\phi / k_BT)} = \frac{I_1(E_J/k_BT)}{I_0(E_J/k_BT)} \tag{3.36}$$

where $I_{0,1}$ are the modified Bessel function. See Appendix B for the definition and a series expansion of this result.

3.3.3 Distribution of the Relative Phase

Since the relative phase fluctuates we study its distribution in the case of negligible relative atom number. For $n \approx 0$ we neglect all terms depending on n and the Hamiltonian reads

$$H(n, \phi) = \frac{1}{2} E_c n^2 - E_J \sqrt{1 - \frac{4n^2}{N^2}} \cos\phi \approx -E_J \cos\phi \tag{3.37}$$

The normalized distribution of the phase depending on the parameter $k_B T/E_J$ is then given by

$$\nu(\phi) = \gamma \exp\left((E_J/k_B T) \cdot \cos\phi\right) \tag{3.38}$$

The normalization constant γ is such that $\int d\phi \nu(\phi) = 1$. In Fig. 3.8 the expected relative phase distribution is shown for different $E_J/k_B T$. For $T \gg E_J$ the phase is uniformly distributed. For very low temperatures the phase distribution results in a sharp peak around zero. We see that a high tunneling rate stabilizes the phase whereas the lack of coupling destroys the relative phase.

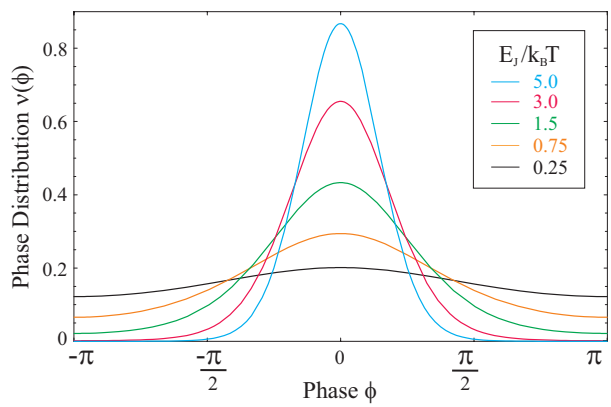

Figure 3.8: The different curves depict the distribution of the relative phase depending on the ratio $E_J/k_B T$. Keeping the tunneling coupling E_J constant and changing the temperature yields a uniform distribution for very high temperatures and a sharp peak for $T \to 0$.

Chapter 4

Experimental Setup and Calibration of the Parameters

In this chapter we discuss the experimental realization of the Bose-Einstein condensate in a double-well confinement. First of all, the necessary steps to cool a Rubidium vapor below the critical temperature are explained. Since the apparatus has been explained in detail in many other theses [28, 29, 34, 35, 36, 37] only a brief overview of the separate steps is given. The second part of this chapter discusses the experimental calibration of the relevant parameters of the experiment such as the magnification of the imaging setup and the trapping frequencies of the corresponding potentials.

4.1 Experimental Procedure to Reach Bose-Einstein Condensation

4.1.1 Gathering Atoms in a Magneto-Optical Trap

In order to reach Bose-Einstein condensation for a dilute atomic cloud we need to cool bosons down to a temperature in the nano-Kelvin range. The atoms have to be isolated from the environment, and thus all experiments are done in an ultra-high vacuum (UHV) chamber[1] with a pressure below 10^{-11}mbar. The whole apparatus is shown in Fig. 4.1. The actual experiments are done inside a glass cell (right part of the apparatus) to be able to access the atoms from outside with laser beams.

The atoms are provided by dispensers containing Rubidium−87. They are heated by an eletrical current of ca. 8A. Since the released Rubidium creates an additional vapor pressure in the chamber we need to separate the dispenser from the region where the experiments take place. This is done by dividing the chamber into two parts and connecting them via a differential pumping stage. The pressure in the first chamber is then 10^{-9}mbar.

The atoms which are released from the dispensers are precooled by a two-dimensional magneto-optical trap (funnel) [38] which results in a directed atom beam. This beam is guided through the differential pumping stage into a three-dimensional magneto-optical trap (MOT) [39] where the atoms are captured. The laser beam arrangement used for

[1] In order to sustain the vacuum the chamber is continously evacuated by two VARIAN ion-getter pumps. One for each part of the chamber (see text).

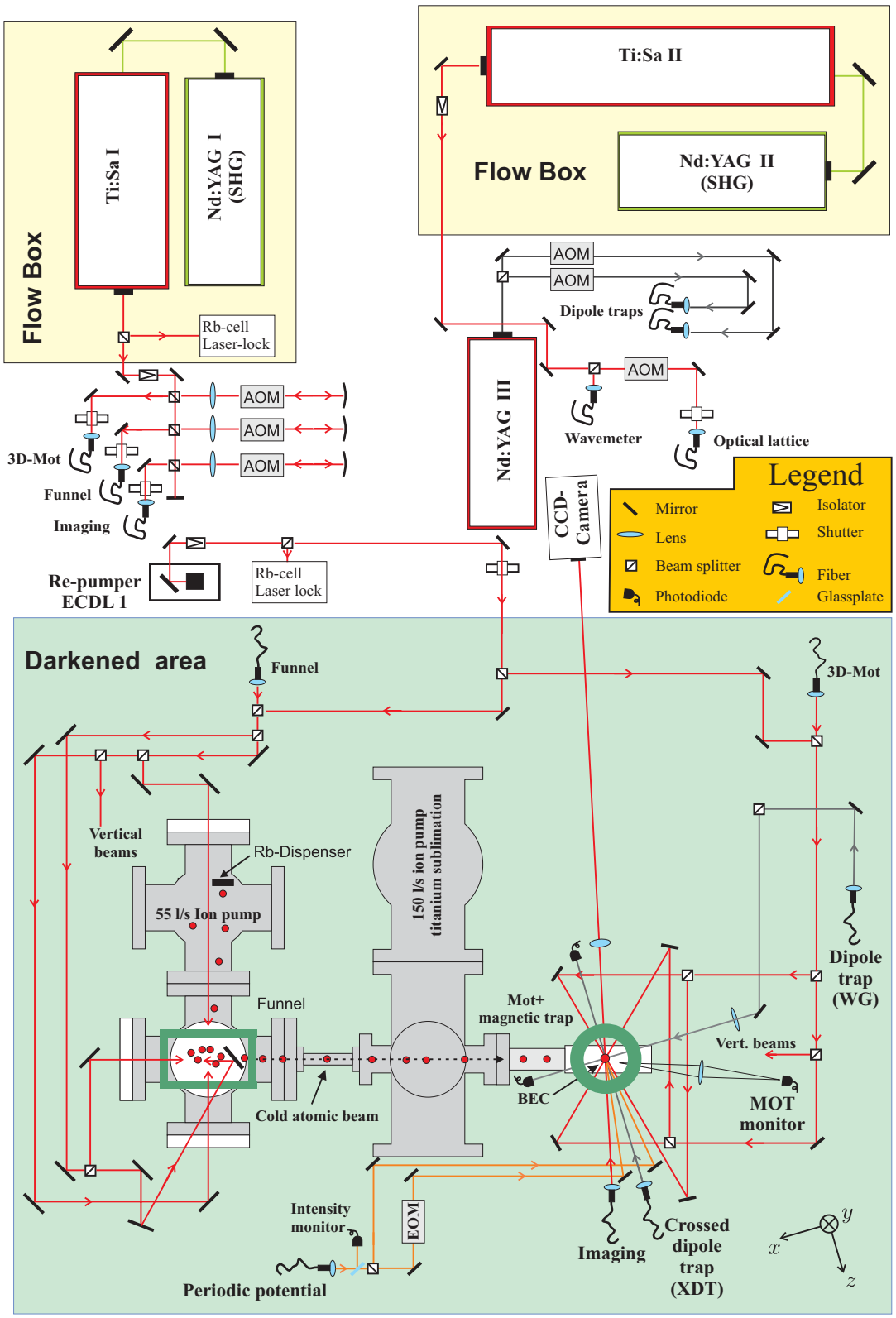

Figure 4.1: Overview of the experimental setup. The whole setup is situated on an optical table. The laser light needed for the experiment is adjusted in the frequency and intensity before it is guided by optical fibers to the vacuum chamber where the Bose-Einstein condensates are prepared (darkened area).

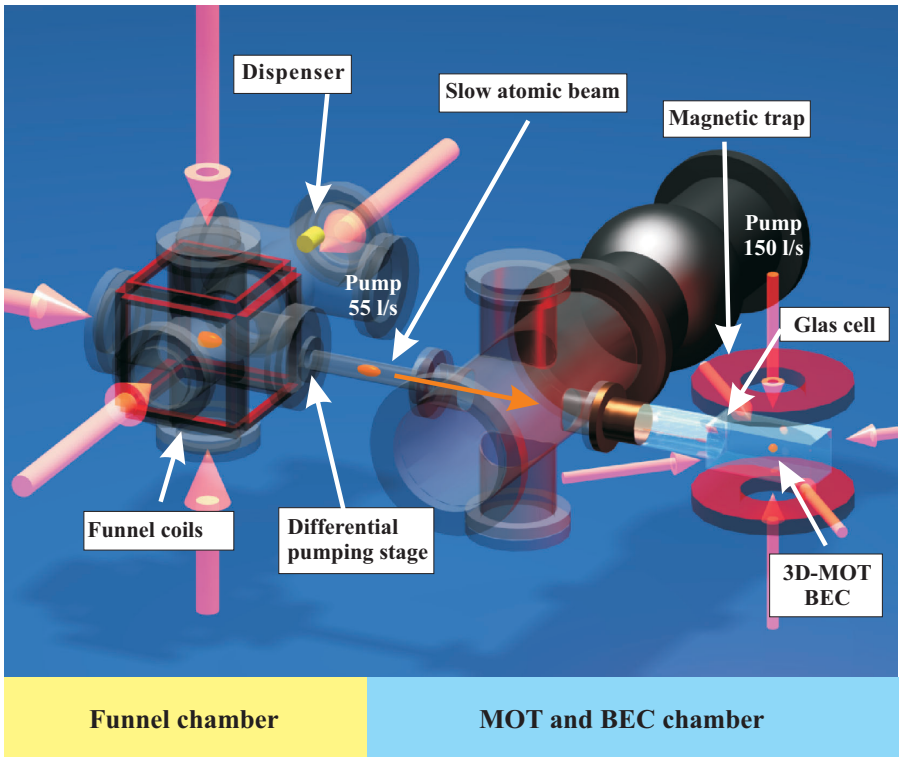

Figure 4.2: Schematic picture of the vaccum setup. In the left chamber the pressure is $\approx 10^{-9}$mbar. A cold atom beam is created in there by means of a funnel [38]. It is directed through a differential pumping stage to the second chamber which has a pressure of below 10^{-11}mbar. The atoms are there collected in a three-dimensional MOT [39] for further cooling (see text).

the setup is schematically depicted in Fig. 4.1 and Fig. 4.2. The light for the funnel and the MOT is provided by a titanium sapphire (Ti:Sa I) laser (*Coherent Monolitic-Block-Resonator 110*) which is pumped by a frequency-doubled diode Nd:YAG laser (*Coherent Verdi V10*). The laser frequency is locked to the ($F = 2 \rightarrow F' = 3$) crossover transition of the D2-line of ^{87}Rb (see Fig. 4.3) by using doppler-free saturation spetroscopy. The beam is then divided into three parts. One for the funnel, one for the MOT laser beams and one for imaging (we will refer to the imaging beam later again). Since we need slightly different wave lengths for each of the beams they are guided through separate acousto-optical modulators (AOM) [40] which are used in double-pass configuration. After that, all laser beams are guided by optical fibres to the experiment.

The MOT beams pump the atoms from the $5S_{1/2}(F = 2)$ state to the $5P_{3/2}(F' = 3)$ state. Due to the small splitting of the $F' = 3$ and $F' = 2$ state, some of the atoms are also pumped to the $F' = 2$ state. Since this part can also decay into the $5S_{1/2}(F = 1)$ state we need to re-pump them back into the cooling cycle again. This is done by an external cavity diode laser (ECDL 1). It is locked to the ($F = 1 \rightarrow F' = 2$) transition (see Fig. 4.3).

The number of trapped atoms is detected by measuring the amount of fluorescing light coming from the atom cloud. By means of optical molasses [41] the cloud is cooled further.

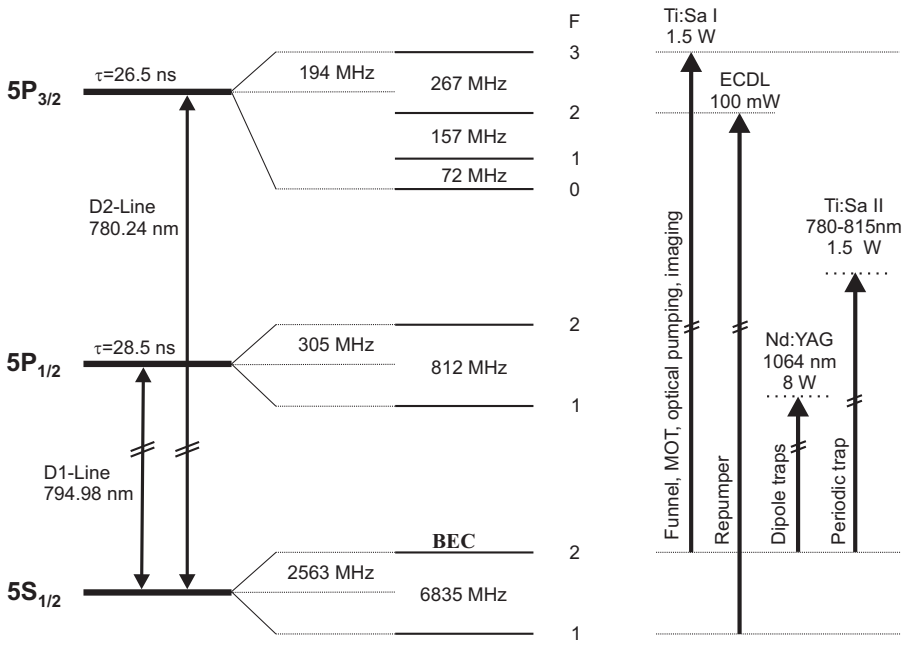

Figure 4.3: Hyperfine structure of Rubidium-87. The right part shows the wavelengths of all lasers that are used in the experiment.

4.1.2 Evaporative Cooling in a Magnetic Trap

By switching off the MOT beams, pumping the atoms to the $|F = 2, m_F = 2\rangle$ state and ramping up the magnetic field the atoms are loaded into a magnetic TOP trap.

The magnetic field is a three-dimensional quadrupole field and is created by two coils in anti-Helmholtz configuration. Since this field has a field strength of zero in the center of the coils the direction of the atomic spin is no longer defined and the atoms can undergo Majorana spin flips [42] to sub-levels which are not trapped anymore. In order to avoid this a *time-orbiting potential* (TOP) [43], i.e. a bias field which circulates with a frequency of 9.8KHz[2], is superimposed to the magnetic trap. The result is a time-averaged harmonic potential which has a non-zero minimum in the center (see [34]). The zero point, which is shifted due to the TOP trap, is moving on a circle around this minimum.

In a magnetic trap the atoms experience a force due to their magnetic dipole moment which interacts with the external magnetic field $\mathbf{B}(\mathbf{r})$. The potential energy of an atom with dipole moment μ reads

$$V(\mathbf{r}) = -\mu \cdot \mathbf{B}(\mathbf{r}) = m_F g_F \mu_B |\mathbf{B}(\mathbf{r})| \tag{4.1}$$

where m_F is the magnetic quantum number, g_F is the gyromagnetic factor of the hyperfine state and μ_B the Bohr magneton. Since the force acting on the atoms is given by $\mathbf{F}(\mathbf{r}) = -\nabla V(\mathbf{r})$ we can trap atoms with $m_F g_F > 0$ in a minimum of the external magnetic field. These are called *low-field seekers*. Trapping *high-field seekers* ($m_F g_F < 0$) in the vacuum is not possible since the Maxwell equations do not allow a local maximum in an area without currents [44]. We trap the atoms in the $|F = 2, m_F = 2\rangle$ because

[2]The frequency has to be chosen satisfying two criteria: At first, it is faster than the center of mass motion of the atoms, so that the atoms cannot follow. Secondly, it is slower than the Larmor frequency, so that the magnetic moment can follow the changing magnetic field.

it has the highest magnetic moment compared to the other sub-levels. The trapping frequency[3] for our magnetic trap is on the order of 100Hz [34].

Since the atoms with high energy are statistically found to be more often in the outer regions of the trap we can get rid of *hot* atoms by applying the rotating bias field since the atoms at the zero point of the field, which is rotating around the center of the trap, can undergo spin flips and fall out of the trap. The slope on which the zero point is rotating is therefore often referred to as *circle of death*. We continously change the radius of the rotation circle starting with a diameter of 1.6mm down to 75μm. Doing this slowly enough (this procedure takes about $\sim$ 30s) the atom cloud is always in thermal equilibrium. Since the hot atoms take out energy of the cloud the temperature is decreased. The cooling of the gas comes along with the loss of atoms. This procedure is commonly referred to as *evaporative cooling* of the gas.

After this cooling stage the atoms are loaded into an optical dipole trap for further cooling.

4.1.3 Evaporative Cooling in an Optical Dipole Trap

Atoms can be trapped by a laser beam since the induced atomic dipolar moment interacts with the external electric field of the beam (*ac Stark shift*). For calculating the resulting potential we assume the atom to be a two level system consisting of a ground and an excited state. The laser frequency ω_L is detuned with respect to the transition frequency ω_0. We define the detuning as $\Delta = \omega_L - \omega_0$.

The potential that a two-level atom experiences in the external field of the laser beam is [45, 46]

$$V(\mathbf{r}) = \left(\frac{\hbar\Gamma^2}{8I_{\text{sat}}}\right) \cdot \frac{I(\mathbf{r})}{\Delta} \tag{4.2}$$

where $I_{\text{sat}} = \pi hc\Gamma/(3\lambda^3)$ is the saturation intensity, λ the laser wavelength and Γ the natural line-width of the transition to the excited state. In the case of ^{87}Rb we need to include the D1 and the D2-transition in our considerations since the atom has more than two levels (see Fig. 4.3). If the laser has a detuning of $\Delta_{1,2}$ for the corresponding transition the potential approximately reads

$$V(\mathbf{r}) = \left(\frac{\hbar\Gamma^2}{8I_{\text{sat}}}\right) \frac{2}{3} \left(\frac{1}{2\Delta_1} + \frac{1}{\Delta_2}\right) \cdot I(\mathbf{r}) \tag{4.3}$$

Here, the Clebsch-Gordon coefficient and the different strength of the transitions are included [45].

The intensity of a focused laser beam of wavelength λ propagating in x-direction with maximal power P is given by

$$I(\mathbf{r}) = \left(\frac{2P}{\pi s_y s_z}\right) \cdot \left(\frac{1}{1 + x^2/R_y R_z}\right) \cdot \exp\left(-2\left(\frac{y^2}{\sigma_y^2(x)} + \frac{z^2}{\sigma_z^2(x)}\right)\right) \tag{4.4}$$

where $s_{y,z}$ is the $1/e^2$-waist, $\sigma_{y,z} = s_{y,z}\sqrt{(1 + (x/R_{y,z})^2)}$ the width and $R_{y,z} = \pi w_{y,z}^2/\lambda$ the Rayleigh length[4] of the beam in y, z-direction. Inserting this result into Eq. (4.3)

[3]Trapping frequency is always meant in comparison with a particle of mass m in a harmonic oscillator with frequency ω.

[4]The Rayleigh length is defined as the distance from the beam waist to the point where the width of the beam broadens by a factor of $\sqrt{2}$.

leads to the corresponding potential. We expand the resulting potential to second order and find for the trapping frequencies

$$\omega_{y,z} = \sqrt{\frac{4|V_{\max}|}{m s_{y,z}^2}} \quad ; \quad \omega_x = \sqrt{\frac{2|V_{\max}|}{m R_y R_z}} \tag{4.5}$$

$$\text{with } V_{\max} = \left(\frac{\hbar \Gamma^2 P}{6 I_{\text{sat}} \pi s_y s_z}\right) \cdot \left(\frac{1}{2\Delta_1} + \frac{1}{\Delta_2}\right) \tag{4.6}$$

Thus, if the Rayleigh length is large enough the confinement in the direction of the beam propagation is negligible.

However, our three dimensional dipole trap in which the atoms are loaded after the magnetic trap is given by two focused laser beams (*Spectra Physics (T 40-X30-106QW, Nd:YAG III)*, Output power 3W) which cross under an angle of 90° as depicted in Fig. 4.4. Since it has a wavelength of 1064nm (corresponding to a positive detuning) the resulting potential is attractive for ^{87}Rb.

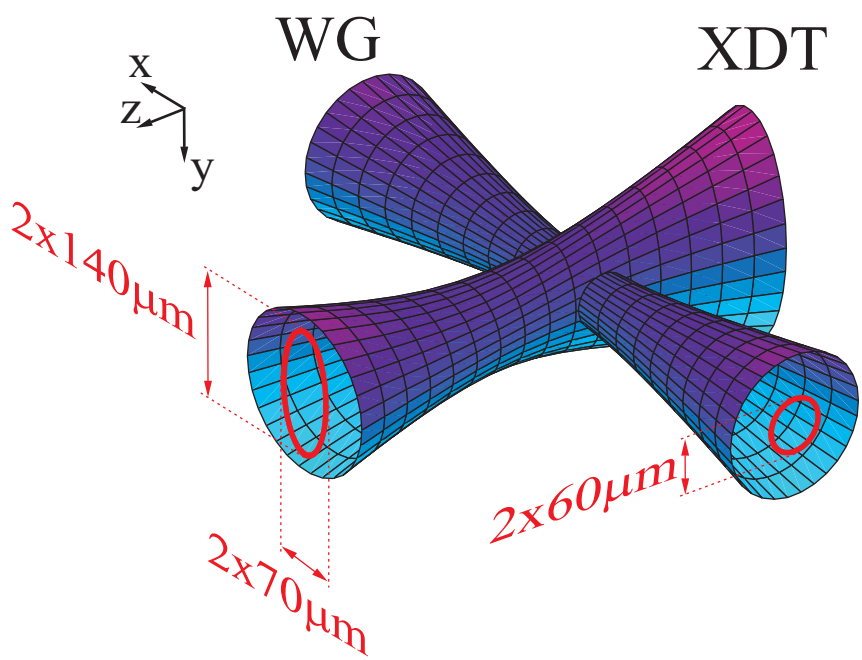

Figure 4.4: The three-dimensional dipole trap for the Bose-Einstein condensate is shown schematically. The surfaces correspond to the $1/e^2$-intensity width of the separate laser beams. The red curves depict the diameter of the beams at the center of the crossing (they have been moved from the center for clarity). The waveguide (WG) which provides the confinement in y and z-direction is of spherical shape. The crossed dipole trap (XDT) provides the confinement in x-direction. It is made asymmetric with a cylindrical lens to minimize its influence in y-direction. The condensate is trapped at the crossing of the two beams.

The Rayleigh length of the beams is on the order of 1cm and thus only a confinement perpendicular to the propagation direction is provided by each beam. The first beam (*waveguide* (WG)) is responsible for the confinement in y and z-direction. It is transversally of spherical shape and has a power of 500mW at maximum. The second beam (*crossed dipole trap* (XDT)) povides the confinement in x-direction. With the use of a cylindrical lense it is made asymmetric in order to guarantee that changing the

confinement in x-direction does not influence the confinement in y-direction too much[5]. In Fig. 4.4 the resulting shape of the beam is shown. The power of the XDT beam is $\sim$ 800mW.

Since each dipole trap beam passes an acousto-optical modulator we can adjust the intensity and thus the trapping frequency of each beam to our needs. In order to stabilize a specified intensity we collect light which is backscattered from the glass cell by a photodiode. The photodiode voltage is compared to the desired value and by means of a proportional-integrator loop [47] the AOM is adjusted such that the set voltage and the desired voltage equal. As well as the MOT beams the XDT and the WG beam are guided by optical fibres to the glass cell.

In the experiment gravity which is pointing in y-direction has to be taken into account. It shifts the minimum of the potential by $\Delta y \approx g/\omega_y^2$ and effectivley reduces the trapping frequencies. We reach the maximal trapping frequencies of $\omega_x = 2\pi \times 120$ Hz, $\omega_y = 2\pi \times 170$ Hz and $\omega_z = 2\pi \times 180$ Hz.

In order to reduce vibrational fluctuations of the dipole traps the XDT fibre has been mounted on an additional table as well as the WG has been mounted on a separate block of aluminium (see Fig. 4.5(a)). The position of the harmonic confinement is then fluctuating due to remaining mechanical instabilities with a standard deviation of 80nm from shot-to-shot (see [28, 29] for measurements on this). In order to adjust long time drift deviations the fibre collimator can be moved with the help of piezo elements.

Having the atoms in the dipole trap we evaporatively cool them further by lowering the laser intensity, thus making the trap shallower, and letting the 'hottest' atoms escape. This is done on a timescale of several seconds. When we pass the critical temperature during this cooling procedure the condensation starts to take place. We cool further down until we reach a temperature of $\sim$ 20nK. The number of atoms in the BEC can be adjusted by changing how far we lower the laser intensity. With our setup it is possible to condense between 1000 and 150.000 atoms in total.

4.1.4 Preparing a BEC in a Double-Well Potential

In order to generate a double-well potential we superimpose a one-dimensional periodic potential with the harmonic trap. The standing light wave creating the periodic potential is realized by two laser beams which intersect at an angle of $\gamma \approx 10°$ (see Fig. 4.5(a,b) for a schematic plot). The two beams are provided by a titanium sapphire laser (Ti:Sa II) (*Coherent, 899*) at a wavelength of $\lambda_{\mathrm{SW}} = 830$nm. The corresponding double-well potential in x-direction then reads

$$V_{\mathrm{ext}}(x) = \frac{1}{2} m\omega_x^2 x^2 + \frac{V_0}{2}\left(1 + \cos\left(\frac{2\pi}{q_L}x\right)\right) \quad \text{with } q_L = \frac{\lambda_{\mathrm{SW}}}{2\sin(\gamma/2)} \tag{4.7}$$

The constant offset of $V_0/2$ can be neglected since it is not effecting any dynamics. The lattice spacing q_L is about 4.78μm in our case.

We have to ensure that the periodic potential and the harmonic confinement are not moving relatively to each other. Therefore, the position of the periodic potential is actively stabilized. This is depicted in Fig. 4.5(b). The light coming out of the fibre is

[5]For the full frequency one has to quadratically add the frequencies resulting from the WG and the XDT.

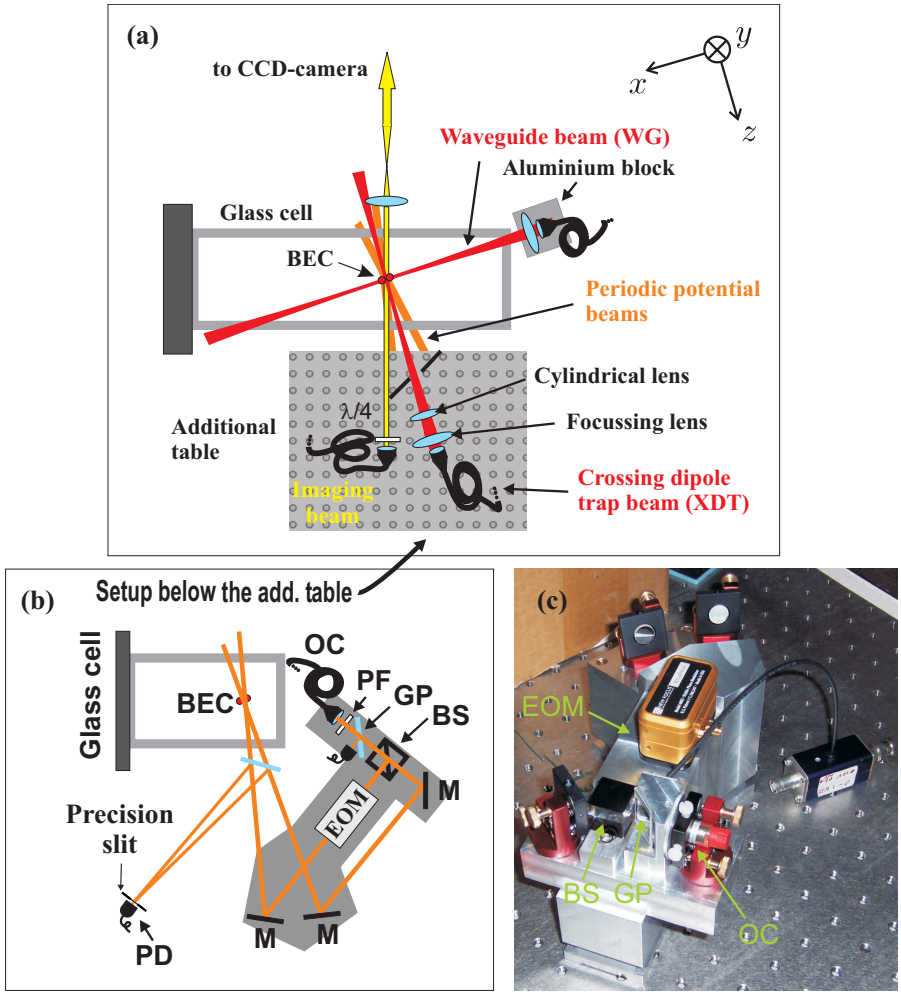

Figure 4.5: (a) The setup close to the glass cell with all optical dipole traps is shown. WG and XDT have been mounted at a separate table and block for better stability. The setup for the periodic potential is situated below the table. It is depicted in Figure (b). A photo of it can be seen in (c).

split up into two beams. One of them is passing an electro optical modulator (EOM) with which we can shift the phase of the beam. The two beams are then overlapped in the region of the BEC in the vacuum for creating the periodic potential. For the stabilization a small fraction of the beams is reflected by a glass plate before reaching the glass cell. The reflected beams intersect and are pictured on a precision slit (*Melles Griot*) of 2μm width. After the slit a photodiode is monitoring the transmitted intensity which depends on the relative phase of the two beams. The resulting photodiode voltage is differentiated by a lock-in amplifier. This control signal is compared to a reference voltage with a proportional integrator loop. The PI loop then adjusts the EOM until the control signal is equal to the reference.

Since we are looking at the derivative of the signal it is not intensity dependent, and thus we can change the intensity without loosing the phase stabilization. With the current electronics it is possible to lock intensity changes on a time scale of milliseconds. Furthermore, the whole setup for the phase stabilization has been built on a separate massive block in order to reduce vibrations (see Fig. 4.5(b,c)). With this method we can stabilize the relative position to 100nm which corresponds to a phase of the periodic potential of $\sim \pi/50$.

4.1.5 Imaging the BEC

In order to get information about the trapped atoms we image them with resonant light and measure the transmitted intensity with a CCD camera. Doing this we destroy the Bose-Einstein condensate since it is heated up (for non-destructive methods see [41]). Since the imaging system has been explained in detail in other theses, see e.g. [29], we give a brief overview.

In our setup the imaging light is a σ_+ polarized gaussian beam (with a waist of 1.9mm) which is resonant to the ($F = 2 \rightarrow F' = 3$) D2-transition of ^{87}Rb. This light is absorbed by the atoms[6] and a shadow image of the cloud is pictured onto the CCD camera. The image itself is magnified before by an aspheric lens system (*Zeiss Plan-Apochromat S, focal length* $f = 10cm$) and projected onto a CCD camera (*Theta System SiS s285M*). Since the absorption of light depends on the scattering cross section and the density of the atomic cloud we can extract the atomic density distribution from the measured intensity distribution on the camera.

For the complete imaging procedure three pictures are used to deduce the information. The first picture images the atom cloud (main picture). We denote its intensity distribution $I(x, y)$. The second picture (reference picture) is taken with the same light intensity but without atoms in order to get the intensity distribution of the imaging beam which we call $I_{\text{Ref}}(x, y)$. The last picture is a background picture without any imaging light which accounts for the background noise. After subtracting the background picture, the main picture and the reference picture are divided in order to get rid of structures resulting from light diffraction. The relative intensity distribution reads

$$T(x, y) = \frac{I(x, y) - I_{\text{Back}}(x, y)}{I_{\text{Ref}}(x, y) - I_{\text{Back}}(x, y)} \tag{4.8}$$

$$\tag{4.9}$$

This quantity is correlated to the atom columm density distribution as

$$n(x, y) = \frac{1}{\sigma} \cdot (-\log T(x, y)) \tag{4.10}$$

where $\sigma = \frac{\Gamma h\nu}{2I_{\text{sat}}(1+I/I_{\text{sat}})}$ is the scattering cross section and ν the frequency of the imaging beam [34]. The number of atoms which is found for one pixel on the camera is then given by $N(x, y) = (A/M^2)n(x, y)$ where $A = 6.45 \times 6.45\mu m^2$ is the pixelsize of the CCD camera and M is the magnification of the lens system which is ~ 10.

Since illuminating a cold gas with resonant light heats it up and results in broadening the cloud we apply very short pulses of $4\mu s$. It leads to a broadening of below 1μm. This is below the optical resolution of $2.7(2)\mu m$. We refer to the thesis of Fölling [29] for a detailed investigation on the optical resolution and diffraction effects coming from our optical setup. We further note that the imaging plane is tilted at an angle of 12.3° with respect to the periodic trap direction. This has to be taken into account when analysing the pictures.

[6]For getting best absorption efficiency a magnetic field is applied in direction of the imaging beam propagation to keep the atoms spin-polarized.

4.2 Calibration of the Parameters

In the following sections a detailed analysis of the calibration of the relevant experimental parameters is discussed. First of all, we determine the magnification of our imaging setup by measuring the free fall of condensates for different times in the gravitational field. The next step is to determine the trapping frequency of the harmonic trap. This is done by measuring dipolar oscillations of condensates in the trap. Furthermore, the atom number determination as described in section 4.1.5 will be cross-checked by considering a different method. The periodic dipole trap is characterized by determining the lattice spacing and investigating induced dipolar oscillations in the wells. For calibrating the lattice spacing we load a large condensate in a trap with a shallow harmonic trap in x-direction and a high periodic potential. The condensate then is populating several wells which directly yields the lattice spacing.

In principle one could determine the trapping potentials for instance by measuring the power and the waist of the beams. We refer to indirect measurements as mentioned above since this method leads to a better accuracy.

4.2.1 Magnification

In order to determine the magnification of the imaging system we use the fact resulting fom classical theory that every mass falls equally in the gravitational field[7]. Thus, we let the condensate fall for different times Δt and measure the falling distance Δd with the help of the images. Since we know the size of one pixel of the CCD chip ($s_{\text{pixel}} = 6.45\mu\text{m}$) we can determine the magnification M by the law of falling bodies as

$$\frac{s_{\text{pixel}}}{M}(\Delta d - d_0) = \frac{1}{2}g(\Delta t - t_0)^2 \tag{4.11}$$

where g is the gravitational acceleration and d_0 and t_0 are constant shifts.

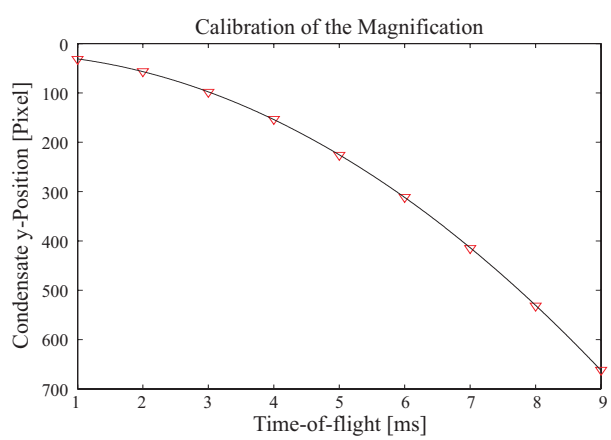

Figure 4.6: Calibration measurement of the magnification of the imaging system. The red triangles correspond to the vertical position of the condensate after switching off the trap and letting the condensate fall for different time-of-flight. Each point represents the average of at least 20 measurements. The error bars are not shown since they are on the order of a few pixel. The black curve corresponds to a least-square fit for Eq. (4.11). The resulting magnification for this measurement is 9.97 ± 0.12.

[7]Since in our experiment we are talking about a quantum mechanical object this is not clear from the beginning.

In Fig. 4.6 a typical calibration measurement of the magnification is shown. The measured falling distances of the condensate are plotted against the time-of-flight. The least-square fit with Eq. (4.11) gives a magnification of 9.97 ± 0.12 for this measurement.

4.2.2 Harmonic Trap

For calibrating the trapping frequencies of the harmonic trap we consider collective dipolar excitations of the condensate [23] initiated by a displacement of the trap center. The principle of the measurement relies on measuring the position of the center of mass of the condensate for different times.

For the excitation in x-direction the XDT beam is shifted by using the piezo-actuated fibre outcoupler. This leads to a shifted harmonic confinement with respect to the condensate. The condensate then starts oscillating in x-direction. The excitation in the y-direction (direction of gravity) is initiated by opening the WG trap for a few milliseconds - corresponding to a shift of the trap minimum - and closing it again. The condensate experiences a reset force and starts to oscillate.

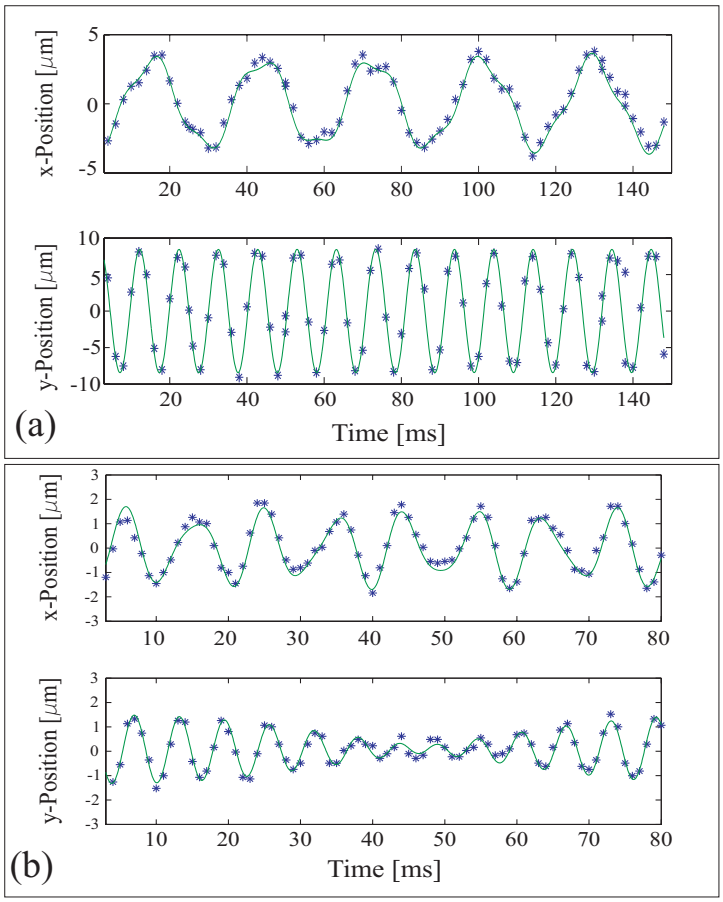

Figure 4.7: The calibration of the harmonic trap for different trap frequencies is shown. The blue points correspond to the measured center of mass position of the condensate after different times in the trap. The green curves show a least-square fit of a sinusoidal oscillation including a possible beating. The upper part of the two figures (a,b) shows the excitation in x-direction whereas the lower the one in y-direction. The resulting frequencies are: (a) $\omega_x = 2\pi \times 35.0 \pm 0.5$Hz, $\omega_{x,\mathrm{beat}} = 2\pi \times 98.7 \pm 0.8$Hz ; $\omega_y = 2\pi \times 98.1 \pm 0.5$Hz (b) $\omega_x = 2\pi \times 103.1 \pm 0.5$Hz, $\omega_{x,\mathrm{beat}} = 2\pi \times 160.6 \pm 1.5$Hz ; $\omega_y = 2\pi \times 153.2 \pm 1.2$Hz, $\omega_{x,\mathrm{beat}} = 2\pi \times 165.0 \pm 0.9$Hz.

Doing these two excitations separately we see sinusoidal oscillations of the center of mass in x and y-direction. Since we cannot observe dynamics in z-direction (direction of imaging beam) we have to rely on an indirect method to determine this oscillation frequency.

If we excite the condensate in both directions x and y at the same time we observe a beating in the frequency. The beating corresponds to a simultaneous excitation in z-direction. Thus, measuring the beating yields all needed frequencies. Fig. 4.7(a,b) depicts a typical measurement of such kind. The center of mass position of the condensate is plotted against the time. Also shown is the least-square fit of a sinusoidal oscillation where a possible beating is included.

4.2.3 Atom Numbers

As mentioned in section 4.1.5 we determine the number of atoms by using the absorption imaging method and comparing the light intensities on the main and the reference picture. We cross-check this method by an independent measurement. The shape of the atomic cloud is strongly dependent on the number of atoms. More atoms result in a broader cloud due to the repulsive atomic interaction. Thus, we measure the width of the atomic density distribution in the harmonic trap for different atom numbers. The atom numbers N_{abs} are determined by the absorption imaging method. We compare the result to a numerical calculation using the non-polynomial Schrödinger equation for different atom numbers N_{NPSE} (see section 2.3.2). The resulting widths of the cloud have been convolved with a gaussian with 2.7μm $1/e^2$-width to account for the finite resolution.

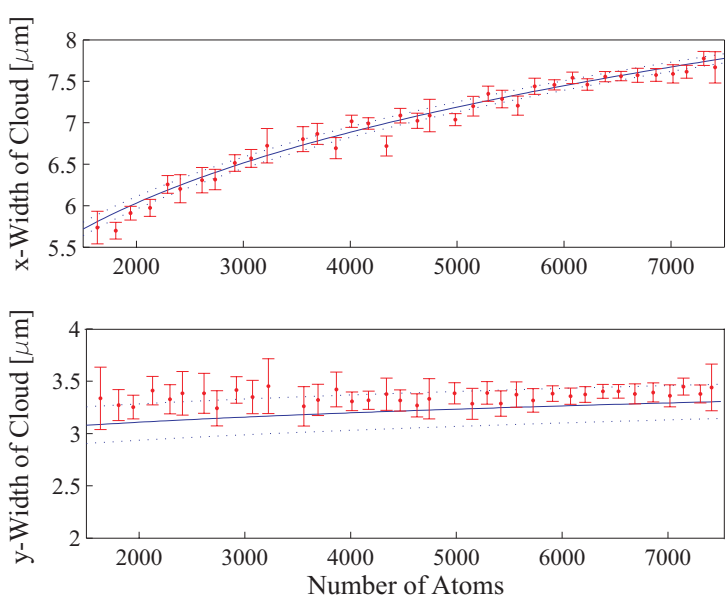

Figure 4.8: The solid line corresponds to a numerical simulation of the widths of the condensate in a harmonic trap ($(\omega_x|\omega_y|\omega_z) = 2\pi \times (35(2)|98(2)|99(2))$Hz) as a function of the atom number N_{NPSE} using the NPSE (see section 2.3.2). The resulting widths have been convolved with a gaussian of 2.7(2)μm $1/e^2$-width to account for the finite resolution. The points correspond to the measured widths where the corresponding atom numbers N_{abs} have been determined with the absorption method and corrected by a factor of 5% (see text). The factor has been deduced by minimizing the standard deviation to the numerical curve. The dotted lines depict the convolved widths of the maximum and minimum resolution due to the error of 0.2μm. We note that the transverse widths are near the limit of our optical resolution, and thus the errors are larger than for the x-widths.

We find a correction factor for the determined atom numbers of $N_{\text{abs}} = 0.95 \cdot N_{\text{NPSE}}$. The measurements with the corrected atom numbers is compared to the numerical calculation in Fig. 4.8. In our experiments the atom number is on the order of 2500, thus the correction is 125 atoms.

4.2.4 Periodic Trap Spacing

For determining the distance between two wells in the periodic trap the confinement in x-direction is decreased while the confinement of the periodic trap is increased to a very high value. By loading a large condensate into this trap we populate many wells as depicted in Fig. 4.9. This picture has been taken with a harmonic confinement of $(\omega_x|\omega_y|\omega_z) = 2\pi \times (10(2)|160(2)|165(2))$Hz. Since the confinement in x-direction is very small we can neglect its influence on the scale of the populated wells. The trap spacing is then determined by fitting a sine modulated gaussian of width σ to the integrated atomic density

$$n_{\text{fit}}(x) \propto \left(1 + \sin\left(\frac{2\pi}{q_L}x + \phi_0\right)\right) \exp(-2x^2/\sigma^2) \tag{4.12}$$

where q_L is the lattice spacing and ϕ_0 a phase shift.

Repeating this measurement 20 times and averaging over the determined lattice spacing we find $q_L = 4.78 \pm 0.02\mu$m in our case.

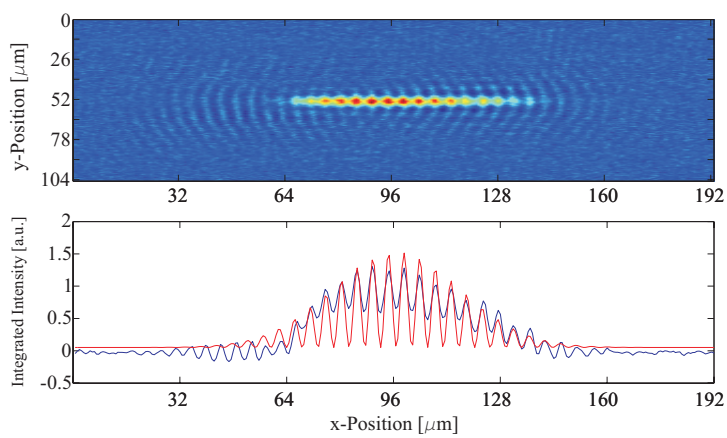

Figure 4.9: The calibration of the periodic trap spacing is shown. Red corresponds to a high atomic density whereas blue corresponds to a low density. For this calibration a large atomic cloud is loaded into a elongated harmonic trap with $(\omega_x|\omega_y|\omega_z) = 2\pi \times (10(2)|160(2)|165(2))$Hz superimposed with a high periodic confinement such that the harmonic confinement in x-direction can be neglected. (a) shows the atomic cloud which is populating many wells of the periodic trap. (b) shows the integrated atomic density which we fit a sine modulated gaussian to in order to determine the lattice spacing.

4.2.5 Periodic Trap Depth

In order to determine the depth of the periodic potential we load a Bose-Einstein condensate into a double-well potential with the unknown barrier height V_0. Increasing the periodic potential non-adiabatically in 2ms to V_F and simultaneously switching off the harmonic confinement in x-direction (which is provided by the XDT) leads to dipolar oscillations of the two separated condensates. However, the oscillations are non-harmonic

since the chemical potential is too high to approximate the potential with a parabola. Thus, it is not enough to measure the frequency of the oscillation in order to determine the trap frequency. Instead, we simulate the described procedure with the NPSE (see section 2.3.2).

For the calibration we measure the relative distance between the two condensates as a function of time. Since we only know the ratio V_0/V_F but not the absolute values[8] of V_0 and V_F, we compare the experimental results to the numerical simulation with the free parameter V_0. This is done by minimizing the least square deviation of the numerical result d_{num} to the measured data d_{meas}

$$\sigma^2 = \frac{1}{k-1}\sum_{j=1}^{k}(d_{\text{num}} - d_{\text{meas}})^2 \tag{4.13}$$

where k is the number of measurements.

A typical measurement of this kind is shown in Fig. 4.10. Here we find for the initial periodic trap depth $V_0 = 159 \pm 15$Hz and $V_F = 1370 \pm 15$Hz.

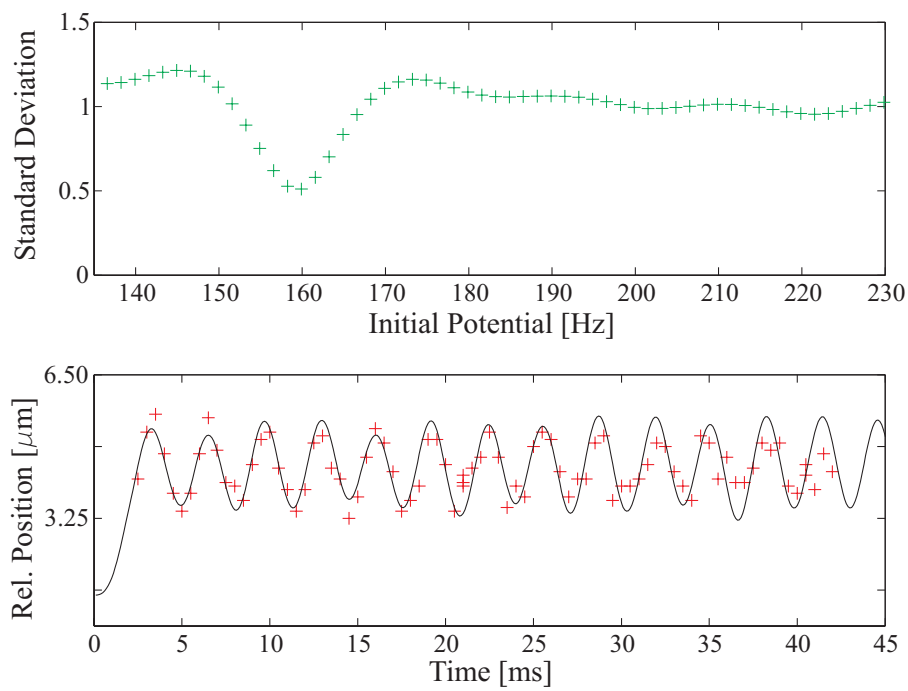

Figure 4.10: The calibration of the periodic potential is shown. The Bose-Einstein condensate is first generated in the double-well. Then, the harmonic confinement in x-direction is switched off, while the periodic confinement is ramped up in 2ms. This excites dipolar oscillations of two separated condensates (one in each well). The points in the lower graph show their measured relative distances. The theoretical curve is calculated by using the NPSE (see section 2.3.2). The simulation has only one free parameter, namely the periodic potential depth at the beginning. We vary this parameter and compare the measured data to the numerical results by minimizing their least square deviation (see Eq. (4.13)). This is shown in the upper graph. The minimum yields the desired value for the initial periodic potential. In this case we find $V_0 = 159 \pm 15$Hz.

[8]The potentials $V_{0,F}$ are assumed to be proportional to the voltage $U_{0,F}$ which is applied to the AOMs used for changing the light intensity. Thus, the ratio of the initial and the final barrier height is given by $V_0/V_F = U_0/U_F$.

Chapter 5

Experimental Results on the Phase Fluctuations in a BJJ

In this chapter we discuss the results on the thermally induced phase fluctuations measurement of a Bose-Einstein condensate in a double-well potential. In the first part the used experimental techniques, such as the deduction of the relative phase, are explained. Since the relevant measurement parameters are the tunnelling coupling between the two modes of the condensate and the temperature, the experimental access to these parameters is discussed in more detail.

In the second part the experimental results on the coherence factor are presented. Since the coherence factor depends on the absolute temperature we study a new method for using it for thermometry. Commonly the temperature of a degenerate Bose gas is determined by observing the expansion characteristics of the thermal cloud. This is only feasible in a regime where the thermal cloud is clearly visible, meaning the signal-to-noise ratio is good enough for distinguishing the thermal cloud from the background noise. For temperatures far below the critical temperature this is not the case anymore, since the number of thermal atoms for instance in a three dimensional harmonic trap scales with $(T/T_c)^3$. In this regime we are able to apply the new thermometer, i.e. the temperature is deduced from the phase fluctuations. This is discussed in the last part of this chapter.

All experiments considered in the following have been done with a harmonic confinement of $(\omega_x|\omega_y|\omega_z) = 2\pi \times (90(2)|100(2)|100(2))$Hz.

5.1 Considerations on the Experimental Method

5.1.1 Phase Measurement

The relative phase between the two modes of the Bose-Einstein condensate in the double-well is deduced by observing the momentum distribution of the condensate. In order to do this we instantly[1] switch off all traps - the harmonic and the periodic trap. The two condensate modes expand freely and interfere. Since the density decreases very rapidly we neglect effects of interaction for the analysis of the interference experiments.

[1]Instantly, here, means as fast as possible with the given electronics, i.e. on the order of microseonds with our setup. This is done in order to project the condensate into free space without influencing the density distribution.

Due to gravity the atoms fall down in the meantime. After a certain time-of-flight we take an absorption image. This time-of-flight has to be chosen such that the measurement is done in the far field. The imaged interference pattern then depicts the momentum distribution. On the other hand the signal-to-noise ratio - which decreases with longer a time-of-flight - needs to be such that the interference pattern is still observable. Some example phase measurements are shown in Fig. 5.1(a). These pictures have been taken for a time-of-flight of 6ms with 3000 atoms in the condensate. It should be noted that this whole procedure is similar to an interference measurement with a double-slit setup for light.

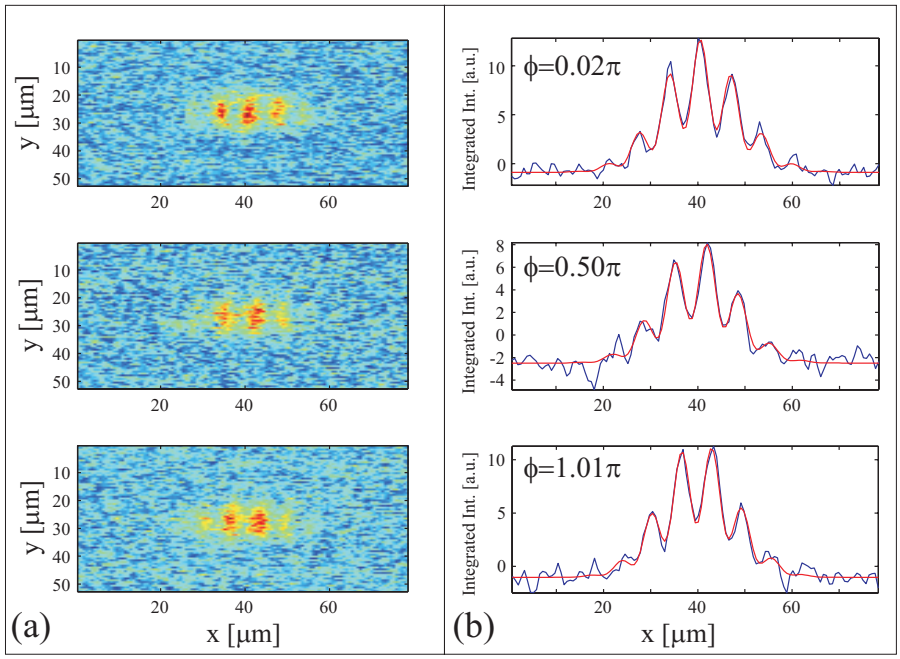

Figure 5.1: (a) Single absorption pictures of the atoms are shown for different values of the relative phase after 6ms time-of-flight. Red corresponds to a high atomic density whereas blue corresponds to a low density. (b) The blue line shows the measured density distribution integrated along the y-direction. The red line corresponds to a cosine modulated gaussian fit from which the phase is deduced.

Phase Deduction with a Negligible Thermal Cloud

In order to deduce the phase from the pictures we integrate the atomic density in the single pictures along the y-direction, i.e. transversally to the double-well. If there is no observable thermal fraction[2] we fit a cosine modulated gaussian with a variable visibility to the integrated density[3](see section 3.3 and Eq. (3.30)). This procedure is shown in Fig. 5.1(b). The blue line depicts the measured data integrated along the y-direction of the corresponding absorption picture on the left. The red line is the cosine modulated gaussian fit for deducing the relative phase of the two modes. The fitting error for the

[2]The distinction between the thermal and the condensate fraction manifests itself in a bimodal distribution of the atom density.

[3]The fitting procedure used is a least square algorithm of MATLAB. Since there are too many degrees of freedom for the phase fit, resulting in a high dimensional parameter space, it is necessary to get the best initial conditions. This is done by fitting a distribution with full visibility first and using the result as initial condition for the fit with a variable visibility.

phase deduction has been estimated by averaging the error resulting from the least-square fit for all measurements and is about 0.13π.

Phase Deduction with an Observable Thermal Cloud

This procedure is extended if there is an observable thermal cloud in the interference picture. We assume that the thermal cloud does not contribute to the interference and we subtract it from the whole distribution. To deduce the thermal fraction we integrate the picture in x-direction, i.e. along the double-well, and fit a bimodal gaussian to the resulting distribution. Having the thermal distribution we go on with the procedure explained above, but subtract the thermal fraction from the integrated interference pattern first.

Deducing the Coherence Factor

Doing many phase measurements we see that the relative phase is fluctuating from shot-to-shot. With respect to the theoretical prediction (see section 3.3.2 and 3.2.2) we calculate the coherence factor α and the standard deviation $\Delta\phi$ for k measurements

$$\begin{aligned} \alpha &= \frac{1}{k}\sum_{i=1}^{k}\cos\phi_i \\ (\Delta\phi)^2 &= \frac{1}{k-1}\sum_{i=1}^{k}(\phi_i - \langle\phi\rangle)^2 \quad ; \quad \langle\phi\rangle = \frac{1}{k}\sum_{i=1}^{k}\phi_i \end{aligned} \tag{5.1}$$

where ϕ_i is the phase of the ith measurement.

5.1.2 Temperature Deduction of the Atomic Cloud

In order to change the temperature of the atomic cloud we hold the atoms for a certain time in the dipole trap. Due to mechanical and electronical noise the intensity of the beams, and thus the trapping frequency, fluctuates and the temperature increases. It turned out that holding the atoms for certain times in the trap is a very reproducible method for adjusting the temperature.

To determine the temperature we fit a bimodal gaussian to the atom cloud after time-of-flight. In order get to better accuracy we average over many pictures for reducing the background noise. Some example pictures for different holding times are shown in Fig. 5.2(a-c). The right part of each picture shows the integrated density distribution and the corresponding bimodal gaussian fits of the absorption images on the left. We see that the width of the thermal cloud is increasing when we hold the atoms longer in the trap. However, the temperature deduction relies on the ratio of thermal atoms N_{th} to condensate atoms N_0 which is given by the bimodal gaussian fit. According to Eq. (2.8) the temperature follows directly from this ratio as

$$T = T_c \cdot \left(1 - \frac{N_0}{N_0 + N_{\text{th}}}\right)^{1/3} \tag{5.2}$$

The critical temperature T_c is deduced from the trap parameters and the total number of atoms (see Eq. (2.7)).

In Fig. 5.2(d) the resulting temperature for different holding times is shown. For this measurement the condensate fraction is kept constant, i.e. 2500 condensate atoms, so that we can compare the interference measurements for different temperatures.

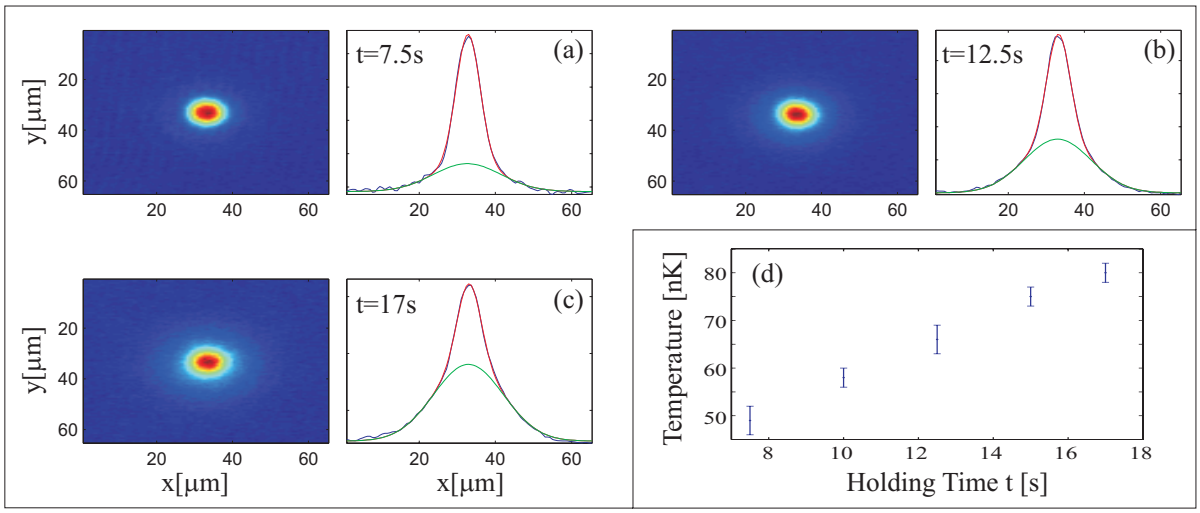

Figure 5.2: (a-c) Shown are averaged absorption pictures (3ms time-of-flight) of the Bose-Einstein condensate after holding the atoms for different times in the harmonic trap. The right part of each picture shows the density distribution integrated along the y-direction (blue line). One can clearly see the expected bimodal gaussian distribution. The fit corresponds to a single gaussian accounting for the thermal fraction (green line) and a gaussian for the condensate fraction (red line). Plot (d) shows the resulting dependency of the cloud temperature on the time for which we hold the atoms in the trap.

5.1.3 Adjusting the Tunnelling Coupling

The second relevant parameter for the experiments is the tunnelling coupling E_J. It is changed by varying the barrier height V_0 of the double-well potential. In order to avoid excitations due to the ramping of the barrier height, the ramp has to be adiabatic with respect to the trapping frequency in the wells which is on the order of 300Hz for the used barrier heights. This gives a lower bound for the ramping timescale.

The tunnelling coupling E_J is calculated within the scope of the two-mode model (see section 3.1 and Appendix A) as a function of the barrier height. These calculations have been done by T. Bergeman [25]. The numerical results are depicted in Fig. 5.3(a) for different number of atoms for a harmonic confinement of $(\omega_x|\omega_y|\omega_z) = 2\pi \times (87|98|98)$Hz. The slope is in very good approximation of exponential shape. For 2500 atoms a fit yields

$$E_J(V_0, N = 2500) \approx 2500 \cdot 4.97\text{Hz} \cdot \exp(-(V_0[Hz] - 500)/158.3) \tag{5.3}$$

Also depicted in the figure is the charging energy E_c as a function of the barrier height. It is nearly independent of V_0 and for our parameters we have approximately $Ec \approx 0.42$Hz or 20pK, respectively.

In Fig. 5.3(b) the corresponding plasma frequency $\hbar\omega_p = \sqrt{E_J E_c}$ is given. Since its inverse is the timescale of the dynamics of the relative phase, it yields the time after which the system is in equilibrium. This is considered in the next paragraph in more detail.

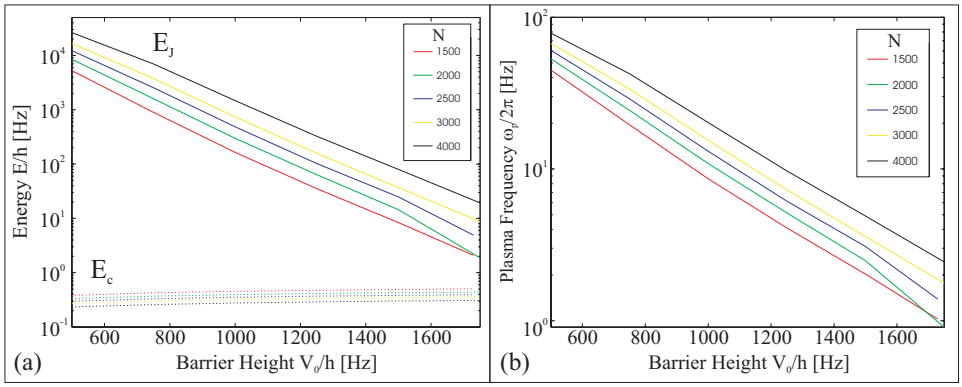

Figure 5.3: (a) The tunnelling energy and the charging energy in the double-well Eq. (3.1) is plotted as a function of the barrier height V_0 for different number of atoms. The harmonic confinement for this calculation has been $(\omega_x|\omega_y|\omega_z) = 2\pi \times (87|98|98)$Hz. This curve is the result of numerical calculations made by T. Bergeman [25] (b) The corresponding plasma frequency is plotted as a function of the barrier height V_0. It is considered for guaranteeing that the system is in thermal equilibrium (see next section).

5.1.4 Thermal Equilibrium

In this section we discuss preliminary experiments on thermalization.

Besides of avoiding excitations while ramping up the barrier for loading the BEC in the double-well potential (see last section) we need to guarantee that the system is in thermal equilibrium all the time. In order to check this we consider different ramping schemes and measure the resulting phase fluctuations. The results on that are depicted in Fig. 5.4(a) for two different ramps. The first was ramping up in 1300ms and measuring the phase fluctuations for different final barrier heights. For the second measurement we ramp up in 300ms after holding the BEC in the harmonic trap for one second and measure the phase fluctuations. The atoms are kept for both schemes for the same time in the trap, so that both measurements correspond to the same temperature.

In order to get an estimation on the response time of the system we consider the plasma frequency since it is the timescale on which the tunnelling process of the atoms take place. For the actual experiments the barrier heights have been varied from $\sim$ 500Hz to 2500Hz. We assume a ramping of 1300ms to be adiabatic with respect to the plasma frequency which is on the order of $1Hz$ for the highest barriers. Since both ramping schemes lead to the same phase fluctuations we deduce the ramp of 300ms to be adiabatic as well.

Another preliminary check has been performed on the increase of the phase fluctuations. Fig. 5.4(b) shows the measured phase fluctuations depending on the holding time in the double-well for two different final barrier heights. The errors result from the fitting error and statistical errors. Since the condensates are less coupled for a higher barrier, the fluctuations are bigger than for the ones with a lower barrier. The increase of the fluctuations corresponds to a heating rate of the system. The dashed line shows the theoretical prediction with a heating rate of 2.3nK/s which has been deduced from measurements in the pure harmonic trap (see section 5.3). The deviation to the data for longer holding times may come from the fact that this heating rate is different for the double-well potential due to the intensity and phase jittering of the additional periodic potential. After these first studies the full measurements on the phase fluctuations are discussed in the next section.

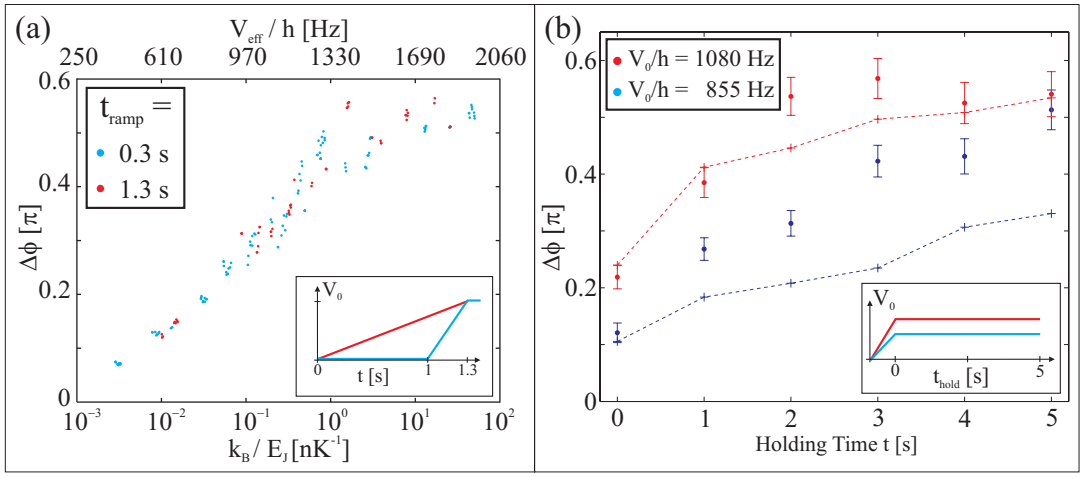

Figure 5.4: (a) The phase fluctuations $\Delta\phi$ are shown as a function of the tunnelling energy and respectively the effective barrier height for different ramping schemes (the second axis depicts the corresponding inverse tunnelling energy $1/E_J$). The red points correspond to a ramping of the periodic potential of 1.3s, whereas for the blue points the condensate has been hold in the trap for 1s and then the periodic confinement has been ramped up in 300ms to the desired value (see also inset). We note that there is no significant difference in the phase fluctuations for both ramps. Since we expect the slow ramp to be adiabatic we also expect the 300ms ramp to be adiabatic as well. (b) The increase of the phase fluctuations within the first 5s of holding the atoms in the double-well potential is plotted for different final barrier heights. As expected for the higher barrier the fluctuations are larger since the condensate modes are more separated, i.e. less coupled. The dashed line shows the theoretical expectation for a heating rate which is valid for the Bose gas in the pure harmonic trap. The deviation may result from a different heating rate due to the additional periodic potential.

5.2 Results on the Thermal Phase Fluctuations

With the previous considerations we summarize the procedure for the measurement on the thermal phase fluctuations. After the condensate is prepared in the harmonic trap the atoms are hold for a certain time in the trap to adjust the temperature T. After the holding time the periodic confinement is ramped up within 300ms to the desired value. We assume that the adiabatic ramping does not change the temperature which has been deduced by independent measurements in the harmonic trap (see section 5.1.2). In order to guarantee that we start with a symmetric distribution in the double-well, the atom distribution in the double-well is checked every $10-15$ shots and, if necessary, adjusted by moving the harmonic potential with the piezo-actuated fibre outcoupler of the XDT. An asymmetric initial position would lead to a change of the tunnelling coupling and the ground state. However, having the Bose-Einstein condensate in the double-well, the traps are switched off suddenly and after a certain time-of-flight an absorption image is taken. For each realisation the relative phase of the two modes is then deduced as described in section 5.1.1.

For all measurements we have chosen a harmonic confinement of $(\omega_x|\omega_y|\omega_z) = 2\pi \times (90(2)|100(2)|100(2))$Hz. With our setup we could vary the barrier height between 500 and 2500Hz. This corresponds to a tunnelling coupling between 30pK ($\sim$ 625mHz) and 400nK ($\sim$ 8300Hz). The charging energy has been 20pK ($\sim$ 420mHz). The temperature has been changed between 50nK and 80nK by holding the atoms between 7.5s and 17s in the trap. Furthermore, a measurement run for not holding the atoms for some extra time in the trap has been done. Since we do not observe a thermal cloud for this case, the

temperature can only be extrapolated from the data of the other measurements, leading to a temperature on the order of 20nK. The atom numbers for the measurements have been varied between 1500 and 3500. Since the tunnelling coupling depends on the atom

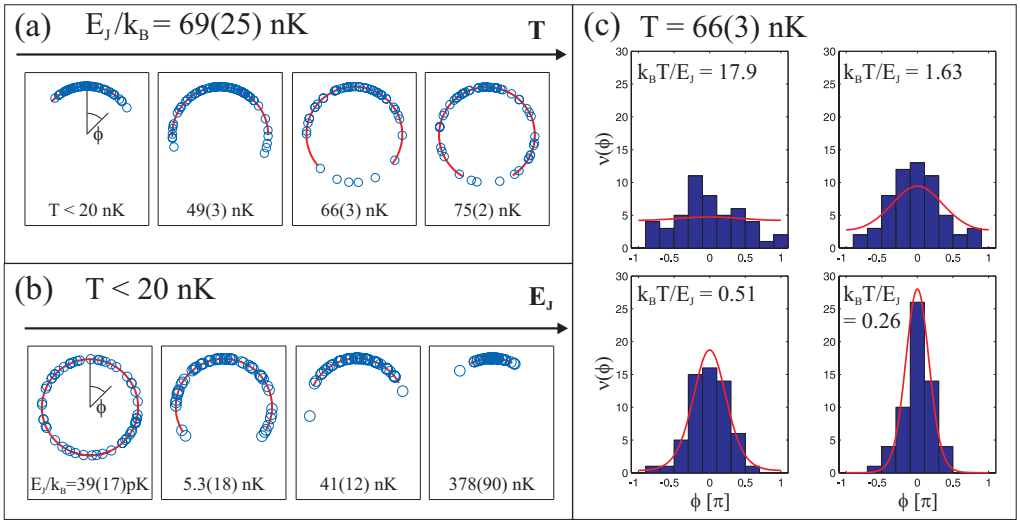

Figure 5.5: (a) shows the measured phase distributions for a constant tunnelling coupling of $E_J/k_B = 69(25)$nK but different temperatures, whereas in (b) the phase distributions for different tunnelling couplings and constant temperature is shown. The open red circle show twice the variance of the phase distribution $2\Delta\phi$. $T < 20$nK corresponds to a measurement without holding the atoms in the trap for some extra time. Since we don't observe a thermal cloud there we need to extrapolate the heating rate (Fig. 5.2(d)), which leads to a temperature below 20nK. This temperature will be discussed later in more detail. (c) shows the phase histogramms for different values of k_BT/E_J. The red line corresponds to a fit according to Eq. (3.38).

number, this has to be taken into account in the analysis of the data.

Repeating the phase measurements we get a distribution of the relative phase which depends on the mentioned parameters. This is depicted in Fig. 5.5. Here, two aspects of the same process are shown in part (a) and (b). For the measurements in graph (a) we keep the tunnelling coupling constant and vary the temperature. We see that the phase fluctuations, which are characterized by the widths of the distributions, increase with increasing temperature. Thus, the relative phase of the two condensate modes is scrambled by the interaction with the thermal fraction of the atom cloud. In part (b) we see the opposite effect. Here, we vary the tunnelling coupling and keep the temperature constant. Increasing the tunnelling coupling, i.e. decreasing the barrier, the phase is stabilized and the fluctuations decrease. Fig. 5.5(c) shows the corresponding histogramms for a temperature of 66(3)nK with the theoretical predicted fit (see 3.3.3). Fig. 5.6 depicts all measurements on the thermal phase fluctuations. In graph (a) we see the phase fluctuations for all different temperatures which we considered. They are plotted as a function of the effective barrier height. In Fig. 5.6(b) the dependence on the temperature and the tunnelling coupling is shown by plotting the coherence factor against the ratio of the two parameters. Every point represents the average of 40 phase measurements. The errors correspond to the statistical error and the error in the experimental parameters, such as the trapping frequencies. Since we do not know the lowest temperature very accurately we do not consider the corresponding points in the plot. The theoretically expected behaviour is given by the dashed black line in the figure (see Eq. (3.35)). However, the finite fitting error of $\phi_0 = 0.13\pi$ will broaden the

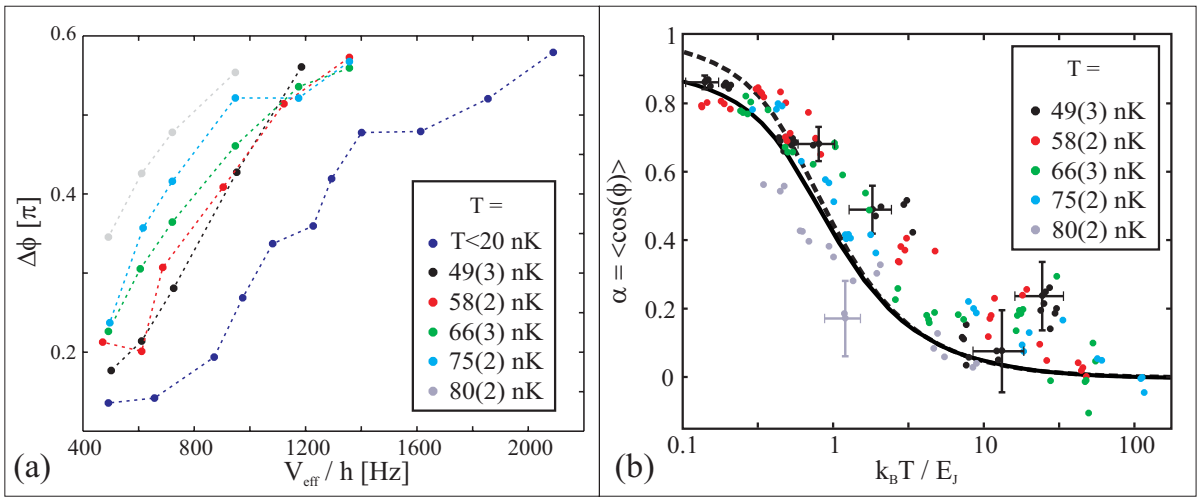

Figure 5.6: (a) All phase fluctuations measurements are shown as a function of the effective barrier height for different temperatures. The lowest temperature corresponds to not holding the atoms for some extra time in the trap (see Fig. 5.5). We see that the fluctuations increase with increasing temperature. (b) The measured coherence factor of all measurements is plotted as a function of the ratio k_BT/E_J. The error bars represent statistical errors and errors in the knowledge of the experimental parameters. For clarity only a few representative bars are plotted. The dashed line corresponds to the theoretical prediction of Eq. (3.35), whereas the solid line takes a systematic error that results from the fitting error into account (see text).

measured phase distribution and thus decrease the coherence factor. This is taken into account by convolving the coherence factor with a phase distribution that corresponds to the fitting error

$$\tilde{\alpha} = \frac{1}{2\phi_0}\int_{-\phi_0}^{\phi_0} d\phi_0 \langle\cos(\phi-\phi_0)\rangle = \frac{\sin(\phi_0)}{\phi_0}\alpha \tag{5.4}$$

The corrected coherence factor is plotted as a solid line in the figure.

The measured points agree very well with the theoretical prediction within the experimental errors for small values of k_BT/E_J, while going to higher values the deviation gets bigger. We note that we measure a visbility α higher than expected for most of the points. This fact is not completely understood yet. One reason might be that the used two-mode model approach is a too simple approximation for considering the whole dynamics but taking the whole excitation spectrum for the thermal cloud into account is theoretically hard to tackle. Even though, the main behaviour is described well within the scope of the two-mode model.

In section 3.3.2 we showed that the coherence factor is proportional to the visibility of the averaged interference pattern. This process is depicted in Fig. 5.7. Part (a) shows the averaged measured interference pattern for decreasing (from left to right) tunnelling couplings for a temperature of 58(2)nK. As expected while increasing the barrier, i.e. decreasing the tunnelling coupling, the bigger fluctuations lead to an averaged interference pattern that gets more and more gaussian like. This is corresponding to a decreasing coherence factor, i.e. the visibility is vanishing. Fig. 5.7(b) shows the fitted visibility α_{fit} of the averaged interference pattern as a function of the coherence factor resulting from the average over the cosine of the measured phases. Effects like the finite resolution and the tilted imaging plane reduce the fitted visibility. In order to take these

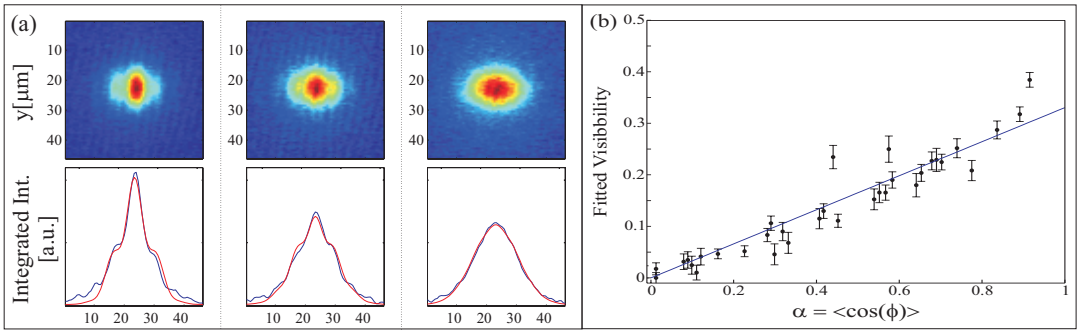

Figure 5.7: In figure (a) the average of 60 phase measurements at a temperature of 58(2)nK, i.e. 10s holding time, is shown. Going from left to right we see the result for different tunnelling couplings, namely $E_J/k_B \sim 243$nK; 15nK; 0.8nK. For lower tunnelling couplings a clear decrease of the visibility is seen. This results from the different amount of fluctuations of the relative phase that depend on the tunnelling coupling. The lower part shows the integrated atom density (blue line). The red line corresponds to a cosine modulated gaussian fit that takes a variable visibility into account. Figure (b) shows the fitted visibility of the averaged interference pattern as a function of the coherence factor. The fit (solid line) yields a reduced resolution of 3.45μm (see text).

effects into account we convolve the averaged interference pattern (see Eq. (3.32)) with a gaussian with a reduced resolution. The corresponding α_{fit} then reads

$$\alpha_{\text{fit}} = \exp\left(-d^2(2\pi)^2 r^2/8k^2(d^2+r^2)\right)\alpha \tag{5.5}$$

where d is the size of the cloud in each well, k is the lattice spacing and r is the reduced resolution. The fit to the data (solid line in the picture) yields a reduced resolution of 3.45μm (see [29] for a detailed analysis on effects reducing the imaging resolution).

5.3 Thermometry with Thermal Phase Fluctuations

Since the thermal phase fluctuations depend on temperature we can, as long as we know the tunnelling coupling, use them for doing thermometry. This is done by measuring the barrier height and determining the tunnelling coupling E_J numerically. By measuring the phase fluctuations we can deduce the temperature by comparing the resulting coherence factor with its theoretical prediction. This new thermometer is demonstrated by measuring the heating up of the Bose gas in the harmonic trap. The difference to the measured heating of the cloud in the previous sections is, that we need to keep the total number of atoms constant. We compare the resulting temperatures with the theoretical prediction that is deduced from the heat capacity of a Bose gas in a harmonic trap. Thus, these measurements are an indirect confirmation of the heat capacity.

5.3.1 Optimal Point and Calibration of the Thermometer

For using the coherence factor for thermometry one should choose the barrier height such that the temperature is strongly depending on it. This is depicted in Fig. 5.8(a). The inset shows the coherence factor as a function of the barrier height for different temperatures. The point of interest is the barrier height where the coherence factor equals 0.5 since we find the biggest gradient there. This can be numerically calculated. The result, i.e. the optimal barrier height V_0 as a function of temperature, is shown in the

plot. Thus, one needs to estimate the regime where the temperature is to be measured and take the corresponding optimal barrier height. In our case a rough estimation of the temperature is $T \approx 20$nK, so that we would choose a barrier height of ~ 1000Hz, corresponding to a tunnelling coupling of ~ 50nK.

We need to calibrate this tool for thermometry, in order to compensate the deviation from the theoretical prediction (see section 5.2). This is done by comparing the temperature we deduce from the coherence factor with the one from the standard method (section 5.1.2) - which we believe to give an accurate temperature - in a regime where both methods are possible. The result is a correction factor for the temperature determined with our new thermometer. This has been done for the phase fluctuations measurements - which we have discussed in section 5.2 - for the data set where we also deduced the temperature. The analysis of that is shown in Fig. 5.8(b).

The different tunnelling couplings have been grouped in three ranges for clarity. From this plot we can read needed the correction factor. In our case this means that the temperature $T_{\Delta\phi}$ deduced from the coherence factor needs to be corrected like

$$T_{\text{real}} = \frac{1}{0.73} \cdot T_{\Delta\phi} \tag{5.6}$$

where T_{real} is the accurate temperature.

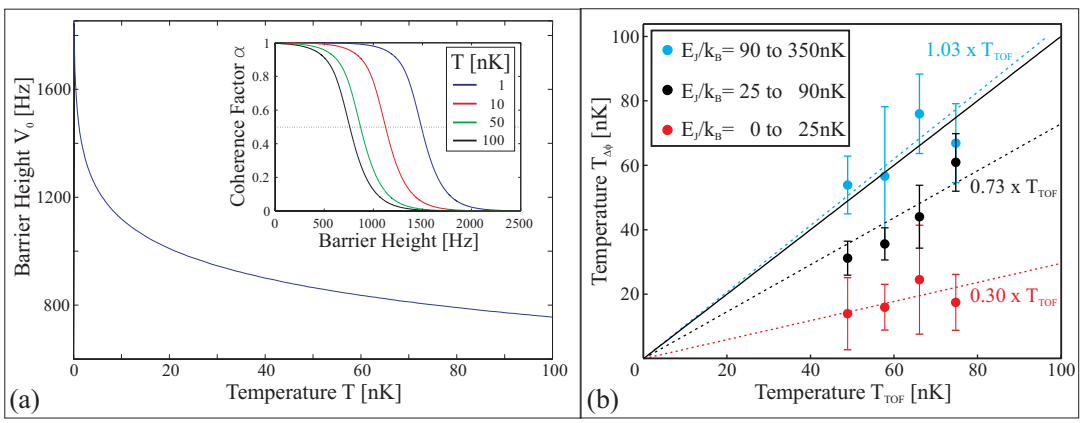

Figure 5.8: (a) The optimal barrier height for the use of the phase fluctuations for thermometry is plotted as a function of the temperature. The optimum is given at the point where the coherence factor equals 0.5, i.e. where the biggest gradient is given (see also inset, where the coherence factor is plotted as a function of the barrier height). (b) The calibration of the phase fluctuations thermometer is shown. In order to compensate the deviation of the experimental data to the theoretical predicition for the phase fluctuation measurements, we need to correct the temperature that is deduced from the measured coherence factor. The correction factor is determined by comparing the temperatures resulting from the well-known standard method (see 5.1.2) with the new phase fluctuations measurement. Since it depends on the tunnelling coupling the factor has been grouped for three regions of E_J.

5.3.2 Results on the Heat Capacity of a Bose-Einstein Condensate

The heat capacity of the degenerate Bose gas in the pure harmonic trap is accessed indirectly by measuring the temperature of the atom cloud as a function of the holding time. In order to be able to compare the results for different temperatures we keep the

total number of atoms constant for all temperatures. For this measurement the total number of atoms has been 2500(500).

The temperature in the pictures can not be deduced from the thermal cloud for holding shorter than 2s, since in this regime the thermal fraction is too small to be observed. But, we can apply the phase fluctuations to determine the temperature. With the new calibrated thermometer we deduce a temperature of 15(4)nK on average for not holding the atoms for some extra time in the trap. The results on the temperature

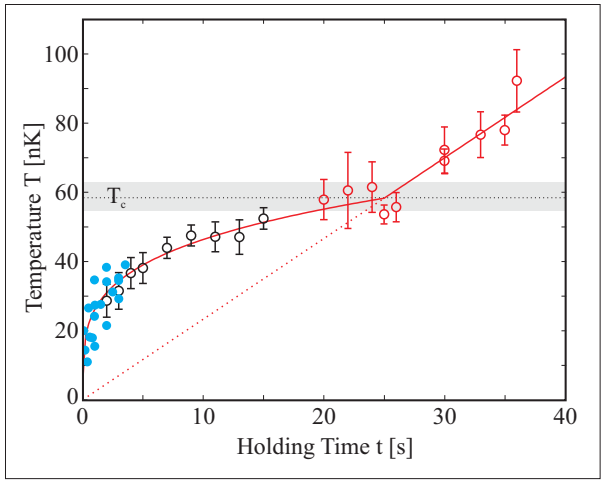

Figure 5.9: The temperature of a Bose-Gas in the three dimensional harmonic trap as a function of the holding time is plotted. The open points depict the measurements done with the standard method (see 5.1.2). Clearly visible is a change in the slope of the temperature dependence after 25s. This corresponds to the expected phase transition which occurs when passing the critical temperature. This is also shown by the different colors for the open circle data points. The red ones correspond to a pure thermal cloud, whereas the black ones, occuring below the critical temperature, represent pictures where a clear condensate fraction and a thermal could be seen. The critical temperature has been determined with the trapping frequencies and the number of atoms (see Eq. (2.7)) and equals 59(4)nK. The filled points correspond to measurements done with the calibrated phase fluctuations thermometer. This measurement revealed that the lowest achievable temperature with our setup is 15(4)nK. The closed line is the theoretically expected behaviour (see Eq. (5.7)).

measurement are summarized in Fig. 5.9. The open circles correspond to the standard method (see 5.1.2), whereas the closed points to deducing the temperature with the coherence factor. In order to compare the results to the theoretical prediction we assume a constant transfer rate of energy κ. The expected heat capacity (see section 2.2) then yields for the temperature depending on the holding time t

$$c = \frac{dE}{dt} \cdot \frac{dt}{dT} = \kappa \cdot \frac{dt}{dT} \quad \Rightarrow \quad T(t) = \begin{cases} \sqrt[d+1]{\frac{\zeta(3)}{\zeta(4)} \cdot \frac{\kappa}{3k_B} \cdot T_c^d \cdot t} & (T < T_c) \\ \frac{\kappa}{3k_B} \cdot t & (T > T_c) \end{cases} \tag{5.7}$$

where d and κ are taken as parameters that are determined by fitting the measurements[4]. The critical temperature for this measurement has been $T_c = 59(4)$nK. It has been deduced with the measured trapping frequencies and the number of atoms (see Eq. (2.7)).

[4]The exact numerical dependency for temperatures right above the critical temperature has been approximated linearly here, since we could not resolve this effect within this measurement.

Fitting the data yields a heating rate of $\kappa/3k_B = 2.3(2)$nK/s and $d = 2.7(6)$. This is consistent with the expected value of $d = 3$ (see section 2.2). It should be noted that the behaviour of the heating up is clearly changing, when the temperature is becoming larger than the critical temperature. This is corresponding to the expected phase transition which occurs in our case after ~ 25s holding time. For longer times we do not have any condensate fraction anymore and we are considering a thermal Bose gas. We note that with our assumption of a constant heating rate the data is in excellent agreement with the theoretical prediction.

Chapter 6

Conclusion and Outlook

In the scope of this diploma thesis the influence of thermal effects on a Bose-Einstein condensate in a symmetric double-well potential is studied. The condensate is described within a two-mode approximation. The two modes correspond to superpositions of the ground state and the first excited state wave function that result in a mode for the left and the right well, respectively. Even though the corresponding Schrödinger equation (Gross-Pitaesvkii equation) for this system is non-linear this approximation is reasonable since these two energy states are nearly degenerate and the gap to higher energies is much larger. The dynamics of the condensate in this approximation is then described by the temporal evolution of two variables, namely the relative phase and the population imbalance between the two modes. The different regimes depending on the initial conditions have been subject to experimental studies [13, 28, 29]. The relative phase is experimentally deduced by doing interference measurements with the two modes, whereas the population imbalance can be directly accessed with the help of the absorption images of the atomic density distribution.

However, in this work fluctuations of these variables are studied. They are expected to arise from two aspects, namely the quantum mechanical uncertainty and the influence of the thermal cloud that always accompanies the condensate. In the experiment the accessible parameters, i.e. the tunnelling energy E_J which is corresponding to the coupling strength of the two modes and the charging energy E_c which is representing the on-site interaction energy, have been chosen such that the quantum fluctuations are negligible. This is the so-called Josephson regime where these parameters fulfil the constraint $E_J/N^2 \ll E_c \ll E_J$. Furthermore, the thermal fluctuations in the atom numbers are negligible since they are below one percent for the considered temperatures and parameters, so that the focus of the experiment is on the thermally induced phase fluctuations. The measurements are analysed by considering the coherence factor, which is representing the visibility of the averaged interference pattern, as a function of the ratio of the temperature and the tunnelling energy. The experimental results are then compared to the theoretical prediction resulting from the two-mode model.

Since the phase fluctuations depend on the temperature it is possible to use these measurements for determining the temperature of the degenerate Bose gas. What makes it so interesting is the fact that the used standard methods for deducing temperatures rely on observing the thermal fraction of the atomic density distribution. This is not possible as soon as the temperature is far below the critical temperature since the thermal fraction scales for instance with $(T/T_c)^3$ in the harmonic trap. In this regime measuring

the thermal phase fluctuations is a good tool for deducing the temperature since only the condensate distribution is relevant for the interference experiments. However, even though the tool is depending on the absolute temperature, it is necessary to calibrate this new thermometer due to a - so far not theoretically understood - deviation of the measured data to the applied theory. This is done by comparing the deduced temperatures with standard methods for temperature deduction in a regime where both are applicable.

Using this tool the temperature of a degenerate Bose gas in a harmonic trap has been measured far below the critical temperature. This measurement yields a temperature of $T = 15(4)\text{nK} \approx T_c/4$ which corresponds to ~ 40 atoms in the thermal fraction of an atom cloud with totally 2500 atoms. Furthermore, an indirect confirmation of the theoretical expected heat capacity of the Bose gas in the harmonic trap is given by measuring the temperature as a function of the holding time in the trap. Assuming a constant heating rate the data is in very good agreement with the theoretical expectation. This measurement confirms that the heat capacity vanishes while approaching the absolute zero as expected from the third law of thermodynamics.

The results on the thermal phase fluctuations and the new thermometer have been summarized and are accepted for publication in Physical Review Letters [48]. Furthermore, a summary on the used experimental techniques and the calibration of the parameters has been published in Applied Physics B [49].

Outlook

The investigation of finite temperature effects with a Bose-Einstein condensate is one necessary step to study the interaction between the thermal cloud and the condensate. Theoretically this issue is hard to tackle due to the many degrees of freedom that are needed for describing the excitation spectrum. One of the next investigative steps on this topic will be experiments on the damping of the observed Josephson oscillations and the decay of the self-trapped state [28] (see also [50, 51] for an investigation of damping within the two-mode model). The time scales on which the energy dissipation takes place are not clear so far, so that the experimental results will give input to theoretical approaches.

One issue that will be tackled in the near future is the investigation of the phase diffusion process [52, 53, 54]. This process manifests itself in collapses and revivals of the relative phase. It has already been subject to investigations by Bloch [55] in an optical lattice potential with two to three atoms per site. In order to do this with our double-well a non-adiabatic ramping scheme for preparing the condensate in the double-well potential should be applied.

Furthermore, the - not so far observed and outstanding - thermal fluctuations of the population imbalance will be studied. In the described measurements they could be neglected. For better accessibility also the atom number detection will be increased in accuracy.

One of the next experimental and technical steps will be installing a new lens system [29] allowing for a better imaging resolution and generating arbitrary potentials that are superimposed to the current potential. This setup can be used to address each well separately via a laser beam. This will make it possible to imprint arbitrary phases on one mode of the condensate, leading to many interesting phenomena. Among them, the

π-oscillations [16], i.e. oscillations of the relative phase around its mean value of π, shall be mentioned since they have not been observed so far.

Another interesting and important application of the Bose-Einstein condensate in the double-well is the creation of dark solitons fans [56, 57, 58]. Dark solitons are expected to be created when doing non-linear interference experiments with the two condensate modes in the double-well. This is done by switching off the barrier of the double-well after a condensate is prepared in it and letting the two modes evolve in the remaining harmonic trap. Preliminary experiments considering the oscillation of the dark solitons in the harmonic trap have already been performed in our group and first results look very promising.

Bose-Einstein condensates have turned out be a probe for many fundamental aspects of quantum mechanics and have given a profound insight into the microscopical world one hardly ever thought is possible. The recent results have made many new predicted effects accessible with current experimental setups, so that this field of ongoing research will be revealing many interesting aspects of physics in the future.

Appendix

Appendix A

The main derivative steps for the dynamical equations of the Standard and the Improved Two-Mode Model are discussed. Furthermore, the numerical results on the parameters of the Two-Mode Model are given as a function of the barrier height in the double-well.

Appendix B

The functional behaviour of the Josephson Hamiltonian and its approximation for $n \ll N$ is studied. Furthermore, an analytical expression for the coherence factor is given in terms of the modified Bessel functions.

Appendix C

The numerical split-step fourier method is presented for solving the non-linear Schrödinger equation and the calculation of the excited states in the double-well is discussed.

Appendix D

A comparison between the exact Hamiltonian - written in terms of creation and annihilation operators - and the classical approximation is discussed in the scope of the coherence factor.

Appendix A

Two-Mode Model Calculations

We discuss the main steps of the derivation of the dynamical equations for both, the Standard and the Improved Two-Mode Model.

Standard Two-Mode Model

We insert the ansatz

$$\Psi(\mathbf{r},t) = \psi_1(t)\varphi_1(\mathbf{r}) + \psi_2(t)\varphi_2(\mathbf{r}) \tag{A.1}$$

into the time-dependent GPE and find the following equation for $\psi_1(t)$ by multiplying with $\phi_1^*(\mathbf{r})$ and integrating over the spatial dimensions

$$\begin{aligned}
\imath\hbar\frac{\partial}{\partial t}\psi_1 \quad = \quad & \underbrace{\int d\mathbf{r}\left(-\frac{\hbar^2}{2m}\varphi_1\nabla^2\varphi_1 + \varphi_1^2 V_{\text{ext}} + gN_1\varphi_1^4\right)}_{=E_1+U_1N_1}\psi_1 \\
& + \underbrace{\int d\mathbf{r}\left(-\frac{\hbar^2}{2m}\varphi_1\nabla^2\varphi_2 + \varphi_1 V_{\text{ext}}\varphi_2\right)}_{=K}\psi_2 \\
& + \int d\mathbf{r}\left(gN_2\varphi_1\varphi_2^3 + g\varphi_1^2\varphi_2^2\psi_1^*\psi_2 + 2gN_1|\varphi_1|^3\varphi_2\right)\psi_2 \\
& + \int d\mathbf{r}\left(g\varphi_1^3\varphi_2\psi_2^*\psi_1 + 2gN_2\varphi_1^2\varphi_2^2\right)\psi_1
\end{aligned} \tag{A.2}$$

With the same method we derive the corresponding equation for $\psi_2(t)$. All terms where products of ϕ_1 and ϕ_2 appear in higher order than two are neglected. With the definitions of $K, E_{1,2}$ and U_1 we then get the two coupled equations for $\psi_{1,2}$ as shown in Eq. (3.8).

We consider the symmetric double-well for which $E_1 = E_2$ and $U_1 = U_2$. By separating imaginary and real part in the equations for $\psi_{1,2}$ we find with the help of the following relations

$$N_1 = \frac{N}{2} + n \quad ; \quad N_2 = \frac{N}{2} - n \tag{A.3}$$

the dynamical eqautions for n and ϕ (Eq. (3.10)).

Improved Two-Mode Model

Doing the same steps as in the Standard Two-Mode Model but factorizing with respect to the $\varphi_\pm$ we find (for simplicity $\hbar = m = 1$)

$$\begin{aligned} &\imath\frac{\partial\psi_1(t)}{\partial t}\left(\varphi_+ + \varphi_-\right) + \imath\frac{\partial\psi_2(t)}{\partial t}\left(\varphi_+ - \varphi_-\right) \\ &= \sum_\pm \left(\psi_1(t) \pm \psi_2(t)\right)\left(\beta_\pm - g|\varphi_\pm|^2\right)\varphi_\pm + \frac{g}{2}\sum_\pm \left(\varphi_\pm^3 P_\pm + \varphi_\pm^2\varphi_\mp Q_\pm\right) \end{aligned} \tag{A.4}$$

The $P\pm$ and the $Q\pm$ are defined as follows

$$\begin{aligned} P_\pm &= 2(\psi_1 \pm \psi_2) - |\psi_1|^2\psi_1 \mp |\psi_2|^2\psi_2 \pm \psi_1^2\psi_2^* + \psi_2^2\psi_1^* \\ Q_\pm &= \pm 2(\psi_2 - \psi_1) + 5\psi_1|\psi_1|^2 \mp 5\psi_2|\psi_2|^2 \pm \psi_1^2\psi_2^* - \psi_2^2\psi_1^* \end{aligned}$$

We introduce new quantities to simplify this equation

$$\begin{aligned} \gamma_{ij} &= g\int dx\varphi_i^2(x)\varphi_j^2(x) \quad \text{for } i,j \in \{+,-\} \\ \Delta\gamma &= \gamma_{--} - \gamma_{++} \\ \Delta\beta &= \beta_- - \beta_+ \\ A &= \left(10\gamma_{+-} - \gamma_{++} - \gamma_{--}\right)/4 \\ B &= \Delta\beta - \frac{\Delta\gamma}{2} \\ C &= \left(\gamma_{++} + \gamma_{--} - 2\gamma_{+-}\right)/4 \\ F &= \left(\beta_+ + \beta_-\right)/2 - \gamma_{+-} \end{aligned} \tag{A.5}$$

$$\begin{aligned} M_{1,2} &= F + A|\psi_{1,2}|^2 - \frac{\Delta\gamma}{4}\psi_{1,2}\psi_{2,1}^* \\ K_{1,2} &= \frac{\Delta\beta}{2} - \frac{\Delta\gamma}{4}|\psi_{2,1}|^2 - C\psi_{1,2}^*\psi_{2,1} \end{aligned}$$

If we multiply Eq. (A.4) separately with $\varphi_\pm$ and integrate over space we find two coupled differential equations for $\psi_{1,2}$ (see [25])

$$\begin{aligned} \imath\frac{\partial\psi_1}{\partial t} &= M_1\psi_1 - K_1\psi_2 \\ \imath\frac{\partial\psi_2}{\partial t} &= M_2\psi_2 - K_2\psi_1 \end{aligned} \tag{A.6}$$

In contrast to the Standard Two-Mode Model the coupling term $K_{1,2}$ depends on time and the interaction. Again using Eq. (A.3) we find the dynamical equations for n and ϕ.

Relation of the defined quantities

The introduced quantities of the Improved Two-Mode Model are related to the corresponding quantities of the Standard Two-Mode Model by (see [25] for a detailed deriva-

tion)

$$\begin{aligned} E_{1,2} &= \frac{1}{2}\left[(\beta_+ - \gamma_{++}) + (\beta_- - \gamma_{--})\right] \\ U_{1,2} &= A + 2C \\ K &= \frac{B}{2} - \frac{\Delta\gamma}{4} \end{aligned} \tag{A.7}$$

Parameters of the Improved Two Mode Model

The relevant parameters A, B and C depend only on the trap geometry and the atom numbers. They have been calculated by T. Bergeman (see also [25]) for our double-well potential of the form

$$V_{\text{ext}}(x) = \frac{1}{2}m(w_x^2x^2 + w_y^2y^2 + w_z^2z^2) + \frac{V_0}{2}\left(\cos\left(\frac{2\pi}{q_0}x\right) + 1\right) \tag{A.8}$$

with $q_0 = 4.78\mu$m, $(\omega_x|\omega_y|\omega_z) = 2\pi \times (87|98|98)$Hz. The results are shown in Fig. A.1. These parameters are connected to the tunnelling energy and the charging energy (see section 3.1.2) as

$$E_J = \frac{N}{2}B \quad ; \quad E_c = \frac{2}{N}A \tag{A.9}$$

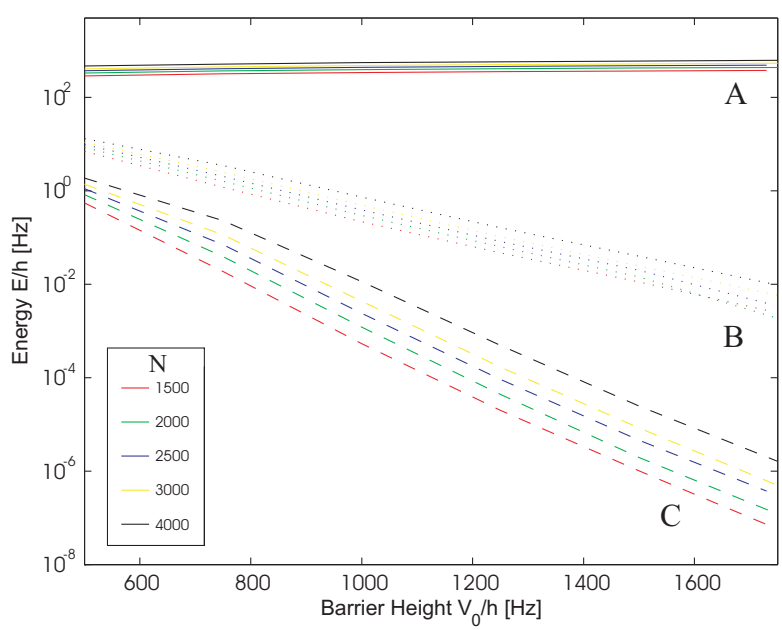

Figure A.1: The relevant parameters A, B and C of the Improved Two-Mode model for the double-well (Eq. (A.8)) are plotted as a function of the barrier height V_0 for different number of atoms.

Appendix B

On the Josephson Hamiltonian and Analytical Results on the Coherence Factor

We consider the Hamiltonian

$$H(n,\phi) = \frac{1}{2}E_c n^2 - E_J\sqrt{1-\frac{4n^2}{N^2}}\cos\phi \tag{B.1}$$

In order to get an idea about the functional behaviour the Hamiltonian is plotted Fig. B.1(a) for $E_J = 100$nK, $E_c = 20$pK and 2500 atoms as a function of the relative phase ϕ and the population imbalance n. Fig. B.1(b) depicts the logarithmic plot of the Boltzman factor $\exp(-H(n,\phi)/k_BT)$ which is needed to calculate the thermal fluctuations and the coherence factor. The temperature is chosen to be 20nK.

We estimate the error that is done when calculating the coherence factor when the square root term in the Hamiltonian is neglected

$$\tilde{H}(n,\phi) = \frac{1}{2}E_c n^2 - E_J\cos\phi \tag{B.2}$$

In the upper graph of Fig. B.2 a numerical comparison of the coherence factor for the full Hamiltonian (solid line) and the one calculated with the Hamiltonian in Eq. (B.2) (blue points) is plotted for $E_c = 20$pK and 2500 atoms. The lower graph shows the deviation of the two coherence factors

$$f_{\text{err}} = 1 - \frac{\tilde{\alpha}}{\alpha} \tag{B.3}$$

We see that for the error made when neglecting the square root term in the Hamiltonian is for our parameters negligible.

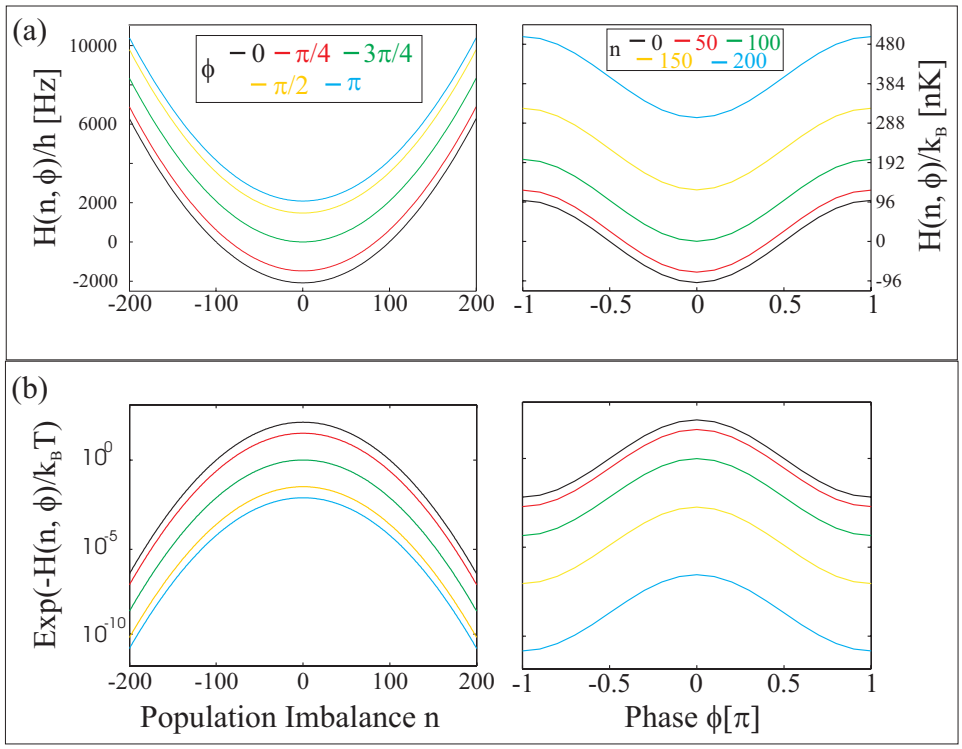

Figure B.1: (a) The Hamiltonian B.1 for different values of ϕ and n (see inset) is plotted. (b) The Boltzmann factor of the Hamiltonian is plotted for the same values as in (a). Here, $E_J = 100$nK, $E_c = 20$pK, the number of atoms is 2500 and the temperature for plot (b) is 20nK.

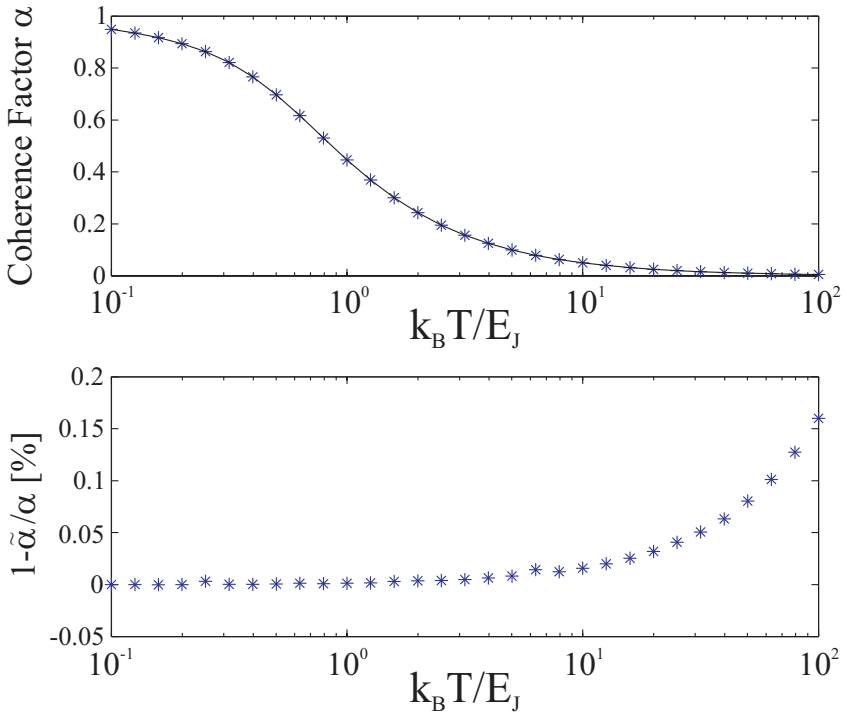

Figure B.2: The solid line in the upper graph shows the coherence factor calculated with the full Hamiltonian Eq. (B.1) as a function of k_BT/E_J for $E_c = 20$pK and 2500 atoms. The points correspond to calculation of the coherence factor with the approximated Hamiltonian Eq. (B.2). The lower graph shows the deviation of the two Eq. (B.3). We see that the error is negligible for our parameter regime.

Evaluation of the Thermal Average Integral

We give an analytic expression for the coherence factor. In the limit of $n \ll N$ it is given by

$$\alpha = \langle \cos\phi \rangle = \frac{\int_{-\pi}^{\pi} d\phi \cos\phi \exp(E_J \cos\phi / k_B T)}{\int_{-\pi}^{\pi} d\phi \exp(E_J \cos\phi / k_B T)} \tag{B.4}$$

The integral is given in terms of the well-known modified Bessel functions of the first kind

$$\alpha = \frac{I_1(x)}{I_0(x)} \qquad \text{with } x = \frac{E_J}{k_B T} \tag{B.5}$$

The modified pth order Bessel functions of the first kind read [59]

$$I_p(x) = \frac{1}{\pi} \int_0^{\pi} d\phi \exp(x \cos\phi) \cos(p\phi) = \frac{2}{\pi} \int_{-\pi}^{\pi} d\phi \exp(x \cos\phi) \cos(p\phi) \tag{B.6}$$

They can be expanded in a series

$$I_p(x) = \sum_{k=0}^{\infty} \frac{\left(\frac{x}{2}\right)^{p+2k}}{k!\Gamma(p+k+1)} \tag{B.7}$$

$$= \frac{1}{\Gamma(p+1)} \left(\frac{x}{2}\right)^p + \frac{1}{1!\Gamma(p+2)} \left(\frac{x}{2}\right)^{p+2} + \frac{1}{2!\Gamma(p+3)} \left(\frac{x}{2}\right)^{p+4} + \cdots \tag{B.8}$$

With this we can give an analytic expression for the coherence factor

$$\alpha = \frac{\sum_{k=0}^{\infty} \frac{1}{(k+1)\cdot(k!)^2} \left(\frac{x}{2}\right)^{2k+1}}{\sum_{k=0}^{\infty} \frac{1}{(k!)^2} \left(\frac{x}{2}\right)^{2k}} \tag{B.9}$$

Appendix C

Numerical Method for Solving the Non-Linear Schrödinger Equation

The Fourier Split-Step Algorithm

The non-linear Schrödinger equation can be solved numerically using a split-step fourier method [60]. This method is suitable for the GPE as for the NPSE. The algorithm is explained in the following.

The time evolution of the wave function obeying the corresponding wave equation can be written with the time evolution operator as

$$\psi(x,t+dt) = \exp\left(-\frac{\imath}{\hbar}\hat{H}dt\right)\psi(x,t) = \exp\left(-\frac{\imath}{\hbar}\left(\hat{p}^2/2m + D(x)\right)dt\right)\psi(x,t) \tag{C.1}$$

where the $\hat{p}$ represents for the momentum operator and $D(x)$ accounts for all terms depending on x. In the Gross-Pitaesvkii equation this term reads $D_{\mathrm{GPE}}(x) = V_{\mathrm{ext}}(x) + g|\psi(x)|^2$, whereas for the NPSE this term

$$\begin{aligned} D_{\mathrm{NPSE}}(x) &= V_{\mathrm{ext}}(x) + g_{1d}\frac{|\Psi(x,t)|^2}{\sqrt{1+2a|\Psi(x,t)|^2}} \\ &\quad + \frac{\hbar\omega_\perp}{2}\left(\frac{1}{\sqrt{1+2a|\Psi(x,t)|^2}} + \sqrt{1+2a|\Psi(x,t)|^2}\right) \end{aligned} \tag{C.2}$$

We expand the time evolution operator in three terms

$$\exp\left(-\frac{\imath}{\hbar}\hat{H}dt\right) \approx \exp\left(-\frac{\imath}{\hbar}\frac{\hat{p}^2}{2m}dt/2\right)\exp\left(-\frac{\imath}{\hbar}D(x)dt\right)\exp\left(-\frac{\imath}{\hbar}\frac{\hat{p}^2}{2m}dt/2\right) \tag{C.3}$$

Since $\hat{p}$ and $D(x)$ do no commute in general we make an error[1] which is on the order of $O(dt^3)$ according to [60]. With this expansion we can propagate the wave function in a very easy way. Since the momentum operator is diagonal in Fourier space ($\hat{p} = p$) we do the time propagation by doing a half time step in Fourier space, then one full step in

[1] This expansion only equals the initial expression when the two operators commute. This comes from the fact the $\exp(A)\exp(B) = \exp(A + B + [A,B] + \cdots)$. See Baker-Cambell-Hausdorf theorem in standard text books [61].

real space and the last half time step in Fourier space again. The corresponding steps read

$$\hat{\psi}(k, t+dt) = \exp\left(-\frac{\imath}{\hbar}\left(p^2/2m\right) dt/2\right) \hat{\psi}(k, t+dt) \tag{C.4}$$

$$\psi(x, t+dt) = \exp\left(-\frac{\imath}{\hbar} D(x)\right) \psi(x, t+dt) \tag{C.5}$$

where $\hat{\psi}(k,t) = \mathrm{FT}[\psi(x,t)]$.

Ground State and Excited State Calculation

The above mentioned algorithm propagates a given initial state in time. If we want to take the ground state of the system as initial state, it has to be calculated in advance. This is done changing the Fourier-Split step algorithm by introducing a Wick rotation, i.e. $\tau = -\imath t$. It means that we can use the same algorithm, but do the propagation in imaginary time. Since this leads to a loss of particles in each step, we have to normalize the wave function in every time step again. Taking an initially good guess on the wave function this progagation will then converge to the ground state wave function of the system [62].

In order to calculate the excited states, we subtract the corresponding part of the (already calculated) lower states in the wave function in each time step. This is done by projecting each lower state upon the wave function and subtracting it. For calculating the Mth excited state this step reads

$$\psi^M(x) = \psi^M(x) - \sum_{i=0}^{M-1} \langle \psi^M | \psi^i \rangle \psi^M(x) \tag{C.6}$$

where $\psi^0(x)$ is the ground state wave function. An example on this method is described in the following section.

The Ground and Excited States in The Double-Well Potential

We applied the above algorithm for solving the NPSE (see section 2.3.2) for a double-well potential. The resulting ground state depending on the barrier height V_0 is shown in Fig. C.1. The calculation has been done with 2500 atoms and a harmonic confinement of $(\omega_x|\omega_y|\omega_z) = 2\pi \times (90|100|100)$Hz.

With the above mentioned method we calculate the eigenstates and thus the eigenenergies of this system. Fig. C.2(a) shows the resulting eigenenergies for the collective excitation of the condensate as a function of the barrier height[2]. With no barrier we have equidistant energies as expected for a harmonic trap. Ramping the barrier up the energies are shifted and move closer together. We note that the ground and the excited state are nearly degenerate. Furthermore, the gap to the second excited state is large compared to the energy difference of the ground and the excited state. This is why the two-mode model only takes the first two states for describing the condensate dynamics into account.

[2]The complete energy here is composed of the energy in the double-well and the energy of the transversal ground state (see section 2.3.2)

Fig. C.2(b) depicts the energy spectrum with the condensate in the ground state and a single particle excited in a higher state as a function of the barrier height. In order to calculate this the interaction energy has been replaced by a term only taking the ground state wave function as interaction potential

$$\psi(x) = \frac{p^2}{2m} + V(x) + g|\psi^0(x)|^2 \tag{C.7}$$

For both graph we see that as soon as the energy is comparable with the barrier height, the corresponding states degenerate.

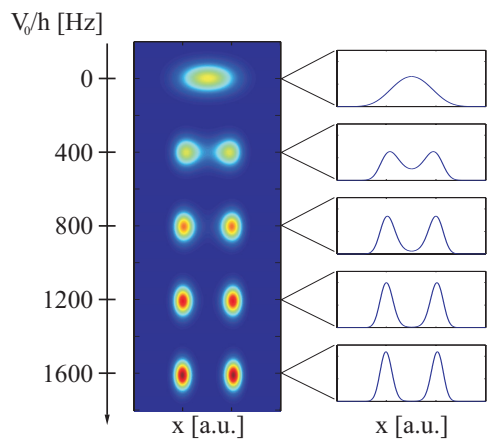

Figure C.1: Shown is the ground state density distribution in a double-well for different barrier heights calculated with the NPSE. The left part shows a two-dimensional plot of the ground state density distribution $|\psi^0(x)|^2$, whereas the right part shows a cut through the center axis. The numerical parameters are $N = 2500$ atoms and the harmonic trapping frequencies of $(\omega_x|\omega_y|\omega_z) = 2\pi \times (90|100|100)$Hz.

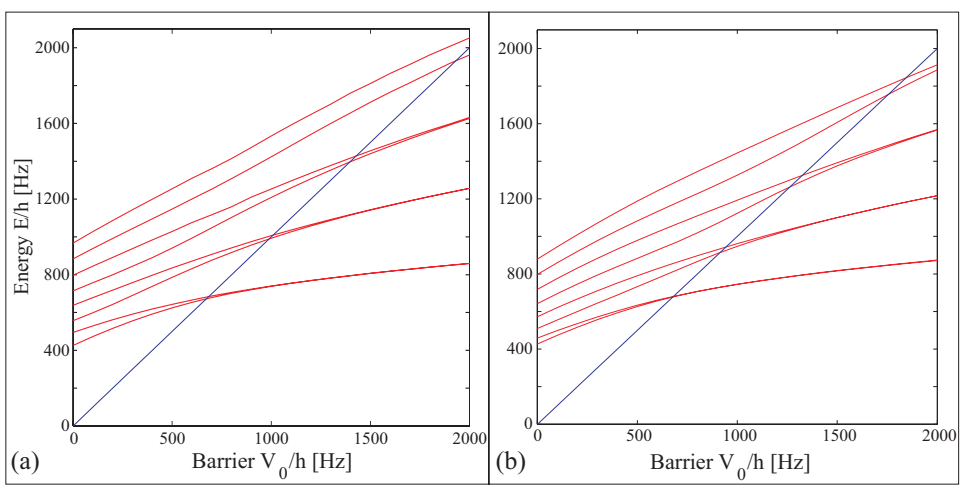

Figure C.2: (a) The collective excitation spectrum for a condensate in a the double-well potential as a function of the barrier height is shown. The calculation have been done using a Fourier split-step algorithm for solving the one-dimensional NPSE. (b) shows the excitation spectrum with a single particle in the higher states while the condensate remains in the groundstate. The numerical parameters for this graph are the same as in Fig. C.1. The dashed line shows the bisecting line for comparing the barrier height with the energy.

Appendix D

Comparison between the Exact Hamiltonian and its Classical Approximation

We consider N atoms in the double-well potential. Let the operator $a^{(\dagger)}$ annihilate (create) a particle in the left well. The operator $b^{(\dagger)}$ applies for the right well. We define the state where N_L particles are in the left well and N_R in the right one as $|N_L, N_R\rangle$. Introducing the population imbalance $n = (N_L - N_R)/2$ we can rewrite the state as

$$|n\rangle := \left|\frac{N}{2} + n, \frac{N}{2} - n\right\rangle \tag{D.1}$$

The creation/annihilation operators of the corresponding symmetric and antisymmetric state in this model are written as

$$c_{s,a}^{(\dagger)} = \frac{1}{\sqrt{2}}(a^{(\dagger)} \pm b^{(\dagger)}) \tag{D.2}$$

The Hamiltonian in this case reads [30]

$$H = \frac{E_c}{4}\left(\left(a^\dagger a\right)^2 + \left(b^\dagger b\right)^2\right) - \frac{E_J}{N}\left(a^\dagger b + b^\dagger a\right) \tag{D.3}$$

Let $N_{s,a} := \langle c_{s,a}^\dagger c_{s,a}\rangle$ be the number of particles in the symmetric and antisymmetric state, respectively. Doing interference experiments the symmetric state corresponds to a relative phase of 0 and the antisymmetric to a phase of π. The averaged momentum distribution for this case reads

$$\langle I(p)\rangle \propto \langle N_a\left(1 + \cos\left(\pi - d\cdot\frac{p}{\hbar}\right)\right) + N_s\left(1 + \cos\left(0 - d\cdot\frac{p}{\hbar}\right)\right)\rangle \tag{D.4}$$

$$\propto \left(1 + \left(1 - \frac{2\langle N_a\rangle}{N}\right)\cos\left(d\cdot\frac{p}{\hbar}\right)\right) \tag{D.5}$$

Thus, the coherence factor is obtained by considering

$$\alpha = 1 - \frac{2\langle\hat{V}\rangle}{N} \quad \text{with} \quad \hat{V} := N_a = \frac{1}{2}(a^\dagger - b^\dagger)(a - b) \tag{D.6}$$

In order to calculate the corresponding average we consider the density matrix ϱ of the canonical ensemble which can be found in standard text books [61]

$$\rho = e^{-H/k_B T} \tag{D.7}$$

The expectation value of the operator $\hat{V}$ follows then as

$$\langle \hat{V} \rangle = \frac{\mathrm{Tr}(\hat{V} \cdot \varrho)}{\mathrm{Tr}\varrho} = \frac{\mathrm{Tr}\left(\hat{V} \cdot e^{-H/k_B T}\right)}{\mathrm{Tr}\left(e^{-H/k_B T}\right)} \tag{D.8}$$

where Tr $M = \sum_k M_{kk}$ is the trace of a matrix M.

With this prelimenary definitions we calculate the matrix elements of the Hamiltonian and the operator $\hat{V}$

$$\begin{aligned}
\langle k|H|n\rangle &= \delta_{k,n} \cdot \frac{E_c}{4}\left(\frac{N}{2}^2 + 2n^2\right) \\
&\quad -\delta_{k,n+1} \cdot \frac{E_J}{N}\sqrt{\left(\frac{N}{2}+k\right)\left(\frac{N}{2}-n\right)} \\
&\quad -\delta_{k,n-1} \cdot \frac{E_J}{N}\sqrt{\left(\frac{N}{2}-k\right)\left(\frac{N}{2}+n\right)}
\end{aligned} \tag{D.9}$$

$$\begin{aligned}
\langle k|\hat{V}|n\rangle &= \delta_{k,n} \cdot \left(\frac{N}{2}\right) \\
&\quad -\delta_{k,n+1} \cdot \frac{1}{2}\sqrt{\left(\frac{N}{2}+k\right)\left(\frac{N}{2}-n\right)} \\
&\quad -\delta_{k,n-1} \cdot \frac{1}{2}\sqrt{\left(\frac{N}{2}-k\right)\left(\frac{N}{2}+n\right)}
\end{aligned} \tag{D.10}$$

In order to simplify equation D.8 we diagonalize the Hamiltonian as

$$H^D = T^t \cdot H \cdot T \tag{D.11}$$

and the expectation value of $\hat{V}$ reads

$$\langle \hat{V} \rangle = \frac{\mathrm{Tr}\left(T^t \hat{V} T \cdot e^{-H^D/k_B T}\right)}{\mathrm{Tr}\left(e^{-H^D/k_B T}\right)} \tag{D.12}$$

These can be easily implemented in a computer algebra program and numerically calculated. Fig. D.1 shows the numerical comparison between the coherence factor resulting from these step and the one resulting from the classical approximation

$$\alpha = \langle \cos\phi \rangle_{\mathrm{th}} = \frac{I_1(E_J/k_B T)}{I_0(E_J/k_B T)} \tag{D.13}$$

with the modified Bessel function $I_{0,1}$. We see that both approaches are in excellent agreement.

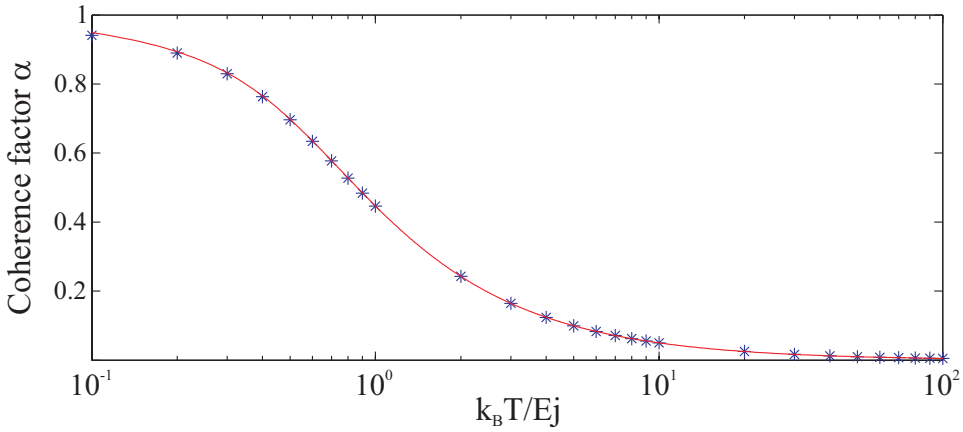

Figure D.1: The comparison between the exact Hamiltonian (Eq. (D.3)) and the classical approximation with respect to the coherence factor α is shown. The red line corresponds to the theoretical prediction for α according to the classical approximation (Eq. (D.13)) as a function of $k_B T/E_J$. The points show the result of a numerical calculation for Eq. (D.6).

Bibliography

[1] L. de Broglie. A Tentative Theory of Light Quanta. *Phil. Mag.*, **47**:446, 1924.

[2] C. Davisson and L.H. Germer. Diffraction of Electrons by a Crystal of Nickel. *Physical Review*, **30**:705, 1927.

[3] N. S. Bose. Plancks Gesetz und Lichtquantenhypothese. *Z. Phys.*, **26**:178, 1924.

[4] Albert Einstein. Quantentheorie des einatomigen idealen Gases. Zweite Abhandlung. *Sitzungsberichte der Preussischen Akademie der Wissenschaften*, **1**:3, 1925.

[5] K. Davis, M.-O. Mewes, M. Andrews, N. van Druten, D. Drufee, D. Kurn, and W. Ketterle. Bose-Einstein Condensation in a Gas of Sodium Atoms. *Physical Review Letters*, **75**:3969, 1995.

[6] M. Anderson, J. Ensher, M. Matthews, C. Wiemann, and E. Cornell. Observation of Bose-Einstein Condensation in a Dilute Atomic Vapor. *Science*, **269**:198, 1995.

[7] C.C. Bradley, C.A. Sackett, J.J. Tollet, and R.G. Hulet. Evidence of Bose-Einstein Condensation in an Atomic Gas with Attractive Interactions. *Physical Review Letters*, **75**:1687, 1995.

[8] M.R. Andrews, C.G. Townsend, H.-J. Miesner, D.S. Durfee, D.M. Kurn, and W. Ketterle. Observation of Interference Between Two Bose-Einstein Condensates. *Science*, **275**:637, 1997.

[9] J. C. Davis and R. E. Packard. Superfluid ^{3}He Josephson Weak Links. *Reviews of Modern Physics*, **74**:741, 2002.

[10] B.D. Josephson. Possible New Effects in Superconductive Tunneling. *Physics Letters*, **1**:251–253, 1962.

[11] P.L. Anderson and J.W. Rowell. Probable Observation of the Josephson Superconducting Tunnel Effect. *Physical Review Letters*, **10**:230, 1963.

[12] A. Barone and P.Paterno. Physics and Applications of the Josephson Effect. Whiley and Sons, New York, 1982.

[13] M. Albiez, R. Gati, J. Fölling, S. Hunsmann, M. Cristiani, and M. K. Oberthaler. Direct Observation of Tunneling and Nonlinear Self-Trapping in a Single Bosonic Josephson Junction. *Physical Review Letters*, **95**:010402, 2005.

[14] I. Zapata, F. Sols, and A.J. Leggett. Josephson Effect Between Trapped Bose-Einstein Condensates. *Physical Review A*, **57**:R28, 1997.

[15] A. Smerzi, S. Fantoni, S. Giovanazzi, and S.R. Shenoy. Quantum Coherent Atomic Tunnelling Between Two Trapped Bose-Einstein Condensates. *Physical Review Letters*, **79**:25, 1997.

[16] S. Raghavan, A. Smerzi, S. Fantoni, and S.R. Shenoy. Coherent Oscillations Between Two Weakly Coupled Bose-Einstein Condensates: Josephson Effects, π Oscillations and Macroscopic Quantum Self-Trapping. *Physical Review A*, **59**:620–633, 1999.

[17] L. D. Landau and E. M. Lifschitz. Statistische Physik. Akademie Verlag, Berlin, 1975.

[18] C.J. Pethick and H. Smith. Bose-Einstein Condensation in Dilute Gases. Cambridge, University Press, 2002.

[19] S.R. de Groot, G.J. Hooyman, and C.A. ten Seldam. On the Bose-Einstein Condensation. *Proc. R. Soc. London A*, **203**:266, 1950.

[20] E.P. Gross. Structure of a Quantized Vortex in Boson Systems. *Nuovo Cimento*, **20**:454, 1961.

[21] E.P. Gross. Hydrodynamics of a Superfluid Condensate. *Jounal of Mathematical Physics*, **4**:195, 1963.

[22] L.P. Pitaevskii. Vortex Lines in an Imperfect Bose Gas. *Sov. Phys. JETP*, **13**:451, 1961.

[23] F. Dalfovo, S. Giorgini, L. P. Pitaevskii, and S. Stringari. Theory of Bose-Einstein condensations in trapped gases. *Rev. Mod. Phys.*, **71**:463, April 1999.

[24] L. Salasnich, A. Parola, and L. Reatto. Effective Wave-Equations for the Dynamics of Cigar-Shaped and Disc-Shaped Bose Condensates. *Physical Review A*, **65**:043614, 2002.

[25] D. Ananikian and T. Bergeman. The Gross-Pitaevskii Equation for Bose Particles in a Double Well Potential: Two Mode Models and Beyond. *Phys. Rev. A*, 73:013604, January 2006.

[26] S. Giovanazzi, A. Smerzi, and S. Fantoni. Josephson Effects in Dilute Bose-Einstein Condensates. *Physical Review Letters*, **84**:4521, 2000.

[27] L. D. Landau and E. M. Lifschitz. Mechanik. Akademie Verlag, Berlin, 1964.

[28] M. Albiez. Observation of Nonlinear Tunneling of a Bose-Einstein Condensate in a Single Josephson Junction. PHD thesis, University of Heidelberg, 2005.

[29] Jonas Fölling. Bose-Einstein Josephson Tunnelling and Generation of Arbitrary Optical Potentials. Diploma thesis, University of Heidelberg, 2005.

[30] G-S Paraoanu, S. Kohler, F. Sols, and A. J. Leggett. The Josephson Plasmon as a Bogoliubov Quasiparticle. *Journal of Physics B*, **34**:4689–4696, 2001.

[31] L. Pitaevskii and S. Stringari. Thermal vs Quantum Decoherence in Double Well Trapped Bose-Einstein Condensates. *Phys. Rev. Letters*, **87**:18, October 2001.

[32] Y. Castin and J. Dalibard. Relative Phase of Two Bose-Einstein Condensates. *Physical Review A*, **55**:4330, 1997.

[33] M. Naraschewski, H. Wallis, A. Schenzle J. I. Cirac, and P. Zoller. Interference of Bose Condensates. *Physical Review A*, **54**:2185, 1996.

[34] B. Eiermann. Kohärente nichtlineare Materienwellendynamik - Helle atomare Solitonen. PHD thesis, Universität Konstanz, 2004.

[35] S. Hunsmann. Josephson-Effekte in Bose-Einstein Kondensaten. Diploma thesis, Universität Heidelberg, October 2004.

[36] M. Taglieber. Helle atomare Gap-Solitonen. Diploma thesis, Universität Konstanz, Oktober 2003.

[37] P. Treutlein. Dispersionsmanagement für Materiewellen. Diploma thesis, Universität Konstanz, Oktober 2002.

[38] K. Dieckmann, R.J.C. Spreeuw, M. Weidemüller, and J.T.M Walraven. Two-Dimensional Magneto-Optical Trap as a Source of Slow Atoms. *Physical Review A*, **58**(5):3891–95, 1998.

[39] E.L. Raab, M. Prentiss, A. Cable, S. Chu, and D.E. Pritchard. Trapping of Neutral Sodium Atoms with Radiation Pressure. *Physical Review Letters*, **59**:2631, 1987.

[40] W.R. Klein and B.D. Cook. Unifed approach to ultrasonic light diffraction. *IEEE Transactions on sonics and ultrasonics*, **SU-14**:123, 1967.

[41] W. Ketterle, D.S. Durfee, and D.M. Stamper-Kurn. Making, Probing and Understanding Bose-Einstein Condensates. In M. Inguscio, S. Stringari, and C. Wieman, editors, *Bose-Einstein Condensation in Atomic Gases*, Amsterdam: IOS Press, 1999. Società Italiana di Fisica.

[42] E. Majorana. Atomi Orientati in Campo Magnetico Variabile. *Nuovo Cimento*, **9**:43–50, 1932.

[43] W. Petrich, M. Anderson, J. Ensher, and E. Cornell. Stable, Tightly Confining Magnetic Trap for Evaporative Cooling of Neutral Atoms. *Physical Review Letters*, **74**:3352, 1995.

[44] William H. Wing. On Neutral Particle Trapping in Quasistatic Electromagnetic Fields. *Prog. Quant. Electr.*, **8**:181, 1984.

[45] H.J. Metcalf and P. van der Straten. Laser Cooling and Trapping. Springer Verlag, 1999.

[46] C. Cohen-Tannoudji, J. Dupont-Roc, and G. Grynberg. Atom-Photon Interactions. Wiley-Interscience, New York, 1992.

[47] P. Horowitz and W. Hill. The Art of Electronics. Cambridge University Press, Cambridge, second edition, 1989.

[48] R. Gati, B. Hemmerling, J. Fölling, M. Albiez, and M. K. Oberthaler. Noise Thermometry with Two Weakly Coupled Bose-Einstein Condensates. *Physical Review Letters (preprint at cond-mat/0601392 v1)*, 2006.

[49] R. Gati, M. Albiez, J. Fölling, B. Hemmerling, and M.K. Oberthaler. Realization of a Single Josephson Junction for BoseEinstein Condensates. *Applied Physics B*, **82**:207, 2006.

[50] I. Marino, S. Raghavan, S. Fantoni, S.R. Shenoy, and A. Smerzi. Bose-Condensate Tunneling Dynamics: Momentum-Shortened Pendulum With Damping. *Physical Review A*, **60**:487, 1999.

[51] J. Ruostekoski and D.F. Walls. Bose-Einstein Condensate in a Double-Well Potential as an Open Quantum System. *Physical Review A*, **58**:R50, 1998.

[52] M. Lewenstein and L. You. Quantum Phase Diffusion of a Bose-Einstein Condensate. *Physical Review Letters*, **77**:3489, 1996.

[53] A. Imamoglu, M. Lewenstein, and L. You. Inhibition of Coherence in Trapped Bose-Einstein Condensates. *Physical Review Letters*, **78**:2511, 1997.

[54] A. Smerzi and S. Raghavan. Macroscopic Quantum Fluctuations in The Josephson Dynamics of Two Weakly Linked Bose-Einstein Condensates. *Physical Review A*, **61**:063601, 2000.

[55] M. Greiner, O. Mandel, T. Esslinger, T. W. Hänsch, and I. Bloch. Quantum Phase Transition from a Superfluid to a Mott Insulator in a Gas of Ultracold Atoms. *Nature*, **415**:39, January 2002.

[56] G. Theocharis, P. Schmelcher, M.K. Oberthaler, P.G. Kevrekidis, and D.J. Frantzeskakis. Lagrangian Approach to the Dynamics of Dark Matter-Wave Solitons. *Physical Review A*, **72**:023609, 2005.

[57] W.P. Reinhardt and C.W. Clark. Soliton Dynamics in the Collisions of Bose-Einstein Condensates. *J. Phys. B. At. Mol. Opt. Phys.*, **30**:L785, 1997.

[58] T.F. Scott, R.J. Ballagh, and K. Burnett. Formation of Fundamental Structures in Bose-Einstein Condensates. *J. Phys. B. At. Mol. Opt. Phys.*, **31**:L329, 1998.

[59] I.N. Bronstein, K.A. Semendjajew, G. Musiol, and H. Mühlig. Taschenbuch der Mathematik. Verlag Harri Deutsch, Thun und Frankfurt am Main, 2000.

[60] Paul L. DeVries. Application of the Split Operator Fourier Transform Method to the Solution of the Nonlinear Schrödinger Equation. *AIP Conference Proceedings*, **160**:269, 1986.

[61] L. D. Landau and E. M. Lifschitz. Quantenmechanik. Akademie Verlag, Berlin, 1984.

[62] M.L. Chiofalo, S. Succi, and M.P. Tosi. Ground State of Trapped Interacting Bose-Einstein Condensate by an Explicit Imaginary Time-Algorithm. *Physical Review E*, **62**:7438, 2000.

Danksagung

Ich möchte mich an dieser Stelle bei allen bedanken, die mich während meines Studiums und meiner Diplomarbeit unterstützt haben:

- Ich danke Prof. Markus K. Oberthaler für die Aufnahme in seine Arbeitsgruppe und die Möglichkeit, in diesem faszinierenden Gebiet der Physik zu arbeiten. Nicht nur sein Enthusiasmus für Physik, auch die Events außerhalb des Labors trugen zu einem schönen und lehrreichen Jahr bei.
- Prof. Jörg Schmiedmayer danke ich für die Begutachtung meiner Arbeit.
- Ich danke 'meinem' Doktoranden Rudolf Gati, von dem ich eine Menge in den vielen Diskussionen während meiner Diplomarbeit gelernt habe und für die angenehme Zeit, die wir gemeinsam im Labor verbrachten. Besonders erwähnt seien hier die vielen 'Sushi-' und 'Chinesisch-Abende' während der Messungen.
- Des weiteren möchte ich mich bei Jérôme Estève, Timo Ottenstein und meinem Vorgänger Jonas Fölling bedanken, die - jeder auf seine eigene Art und Weise - für eine nette Zeit inner- und außerhalb des Labors gesorgt haben.
- Ralf Stützle, Lisa Kierig, Ute Schnorrberger und Ramona Ettig, die am Argon-Experiment in unserer Gruppe arbeiten, möchte ich ebenfalls für die nette Gruppenatmosphäre danken. Ein besonderer Dank geht hier natürlich an das ewig verschnupfte Ramona Schaf!
- Ich möchte mich bei meiner besten Freundin Sabine für die tolle Zeit, die wir in den letzten Jahren gemeinsam verbrachten, bedanken. Aber: ,,Hüte Dich vor dem Groooove, Sabine!"
- Schließlich danke ich meiner Familie für ihre Unterstützung während meines Studiums.

Erklärung:

Ich versichere, dass ich diese Arbeit selbstständig verfasst und keine anderen als die angegebenen Quellen und Hilfsmittel benutzt habe.

Heidelberg, den _____ _____

Unterschrift